INFORMATION TO USERS

This manuscript has been reproduced from the microfilm master. UMI films the text directly from the original or copy submitted. Thus, some thesis and dissertation copies are in typewriter face, while others may be from any type of computer printer.

The quality of this reproduction is dependent upon the quality of the copy submitted. Broken or indistinct print, colored or poor quality illustrations and photographs, print bleedthrough, substandard margins, and improper alignment can adversely affect reproduction.

In the unlikely event that the author did not send UMI a complete manuscript and there are missing pages, these will be noted. Also, if unauthorized copyright material had to be removed, a note will indicate the deletion.

Oversize materials (e.g., maps, drawings, charts) are reproduced by sectioning the original, beginning at the upper left-hand corner and continuing from left to right in equal sections with small overlaps. Each original is also photographed in one exposure and is included in reduced form at the back of the book.

Photographs included in the original manuscript have been reproduced xerographically in this copy. Higher quality 6" x 9" black and white photographic prints are available for any photographs or illustrations appearing in this copy for an additional charge. Contact UMI directly to order.

UMI

A Bell & Howell Information Company
300 North Zeeb Road, Ann Arbor MI 48106-1346 USA
313/761-4700 800/521-0600

Experimental Investigations of Shear-Induced Particle Migrations in Concentrated Suspensions Undergoing Shear

by

Anubhav Tripathi

A Dissertation Submitted to the Graduate Faculty in Engineering in Partial Fulfillment of the Requirements for the Degree of Doctor of Philosophy

The City University of New York

1998

This manuscript has been read and accepted for the Graduate Faculty in Engineering in satisfaction of the dissertation requirement for the degree of Doctor of Philosophy.

8/17/98
Date

Chairman of Examining Committee

8/17/98
Date

Executive Officer

Prof. Andreas Acrivos(Mentor)

Prof. Sheldon Weinbaum

Dr. Eric Herbolzheimer

Prof. David Rumschitzki

Prof. Charles Maldarelli

Prof. Yiannis Andreopoulos

Supervisory Committee

THE CITY UNIVERSITY OF NEW YORK

ABSTRACT

Experimental Investigations of Shear-Induced Particle Migrations in Concentrated Suspensions Undergoing Shear

by

Anubhav Tripathi

Advisor: Professor Andreas Acrivos

This thesis describes the results of four sets of experiments which were performed to investigate shear-induced particle migrations in concentrated suspensions undergoing shear. The first part deals with the measurement of the shear-induced particle and fluid-tracer diffusivities in concentrated suspensions by a new correlation technique. These self-diffusivities were measured in the velocity gradient and vorticity directions in a narrow gap Couette device for values of the strain $\gamma\Delta t$ ranging from 0.05 to 0.5, where γ is the applied shear rate and Δt is the correlation time. The particle diffusivities were found to be in good agreement with the experimental results of Leighton

& Acrivos (1987a) and of Phan & Leighton (1993), even though these earlier studies were performed at much larger values of $\gamma\Delta t$. It was shown, for the first time, that, in concentrated suspensions, the transverse motion of a particle becomes chaotic at very low values of the strain. This is a remarkable result, because it was generally believed thus far that a diffusive behavior could only be attained for experimental time-scales $\gamma\Delta t > 1$, i.e. when the time-scales are larger than the collision time in a simple shear flow and a particle has experienced several interactions. In addition, the fluid diffusivities were found to be 0.7 times the corresponding particle diffusivities for values of the particle concentration ranging from 0.3 to 0.5. This is the first time that fluid diffusivities have been measured in concentrated suspensions. The second part of the thesis deals with the phenomenon of viscous resuspension in bidensity suspensions. Experiments were performed in a narrow gap Couette device using a bidensity suspension consisting of two type of particles, both having same size, one of which was heavy while the other had the same density as that of the suspending fluid. The resuspension height of an initially settled bed of heavy particles was measured over a ten-fold range of the applied shear rate using an imaging technique which was developed to study the particle migration process in concentrated bidisperse suspensions. It was found that, at a given shear rate, the resuspension height of the heavy particles increased with an increase in the concentration of the neutrally buoyant spheres. A bidensity model based on the Leighton & Acrivos

migration theory was then developed and was found to be in good agreement with the experimental results. The success of the bidensity model has provided strong evidence that the observed enhancement of the resuspended height is due to the existence of a shear-induced particle diffusivity and the decrease in the settling velocity of the heavy particles due to presence of the neutrally buoyant particles in the region above the initially settled bed of heavy particles. The third part of the thesis concerns a theoretical and experimental study for examining the maximum value of the volumetric feed rate possible in an inclined settler operated continuously in the bottom feeding mode. A new upper bound for the maximum value of the volumetric feed rate which can be tolerated under a given set of conditions was found theoretically as well as experimentally. Finally, in the last chapter, particle velocity and velocity fluctuations were measured in a concentrated suspension being sheared in a Couette device using laser Doppler anemometry. The purpose of these measurements was to provide information about values of the so-called *suspension temperature* T which equals the sum of the translational velocity fluctuations for a particle relative to its mean translational velocity. All the measurements were corrected for the influence of the LDA noise. Unfortunately, the order of magnitude of the LDA noise and of the particle velocity fluctuations was found to be the same and, in addition, the latter included a contribution of the particle rotation which does not enter into the expression of T and which could not be removed from the measured

data. Hence, any quantitative conclusions regarding T could not be made even though the measured experimental results were comparable to those obtained by Shapley *et al.* (1997). Finally, a suggestion is made on how the problems of the particle rotation and the LDA noise could be overcome.

Acknowledgments

It is a great pleasure to thank my supervisor, Professor Andreas Acrivos. I am much indebted to him for his patient guidance and continual encouragement throughout the course of this research; it is impossible to assess the great influence which he has had upon this work and myself.

I would like to thank Drs. Boris Khusid, Bir Kapoor, Avi Nir, Roberto Mauri, Elizabeth Guazzelli and Ms. Nina Shapley for their valuable suggestions. I would also like to thank our collaborator Mr. Victor Breedveld in the first part of this research.

Many thanks to Akhilesh, Apeksha, Vishwanath, Mahesh, Larry, Sudhir, Mayank, Andy and Mary.

My thanks are due to the US Department of Energy for the grant DE-FG02-90ER14139A008.

List of Tables

List of Figures

Contents

Chapter 1

Measurements of the Shear-Induced Particle and Fluid Tracer-Diffusivities in Concentrated Suspensions by a Novel Method

abstract

The shear-induced particle self-diffusivity in a concentrated suspension (20% - 50% solids volume fraction) of non-colloidal spheres (90 μm average diameter) was measured using a new correlation technique. This method is based on the correlation between the positions of tracer particles in successive images and can be used to determine the self-diffusivity in non-colloidal suspensions for different time-scales. These self-diffusivities were measured in the velocity gradient and vorticity directions in a narrow gap Couette de-

vice for values of the strain $\gamma \Delta t$ ranging from 0.05 to 0.5, where γ is the applied shear rate and Δt is the correlation time. In both directions, the diffusive displacements scaled linearly with $\gamma \Delta t$ over the range 0.05–0.5 and the corresponding diffusivities were found to be in good agreement with the experimental results of Leighton & Acrivos (1987a) and of Phan & Leighton (1993), even though these earlier studies were performed at much larger values of $\gamma \Delta t$. The self-diffusivity in the velocity gradient direction was found to be about 1.7 times larger than in the vorticity direction. The technique was also used to measure the shear-induced fluid tracer-diffusivity in concentrated suspensions (30%-50% solids volume fraction) of non-colloidal spheres(325 μm average diameter) containing a small fraction of 35 μm diameter tracer particles. The fluid diffusivities were found to be 0.7 times the corresponding particle diffusivities when both diffusivities were scaled with γa^2 ($2a = 325$ μm).

1. Introduction

The self-diffusion of tracer particles in non-colloidal, as well as non-Brownian, suspensions has attracted a great deal of attention in recent years. Even at low Reynolds numbers, where inertial effects play a negligible role, particles in such suspensions exhibit diffusion-like motions due to hydrodynamic interactions with their neighbors whose positions have a random component. These interparticle interactions induce a net particle migration in the presence of inhomogeneities in the bulk shear rate or in the particle concentration.

In order to understand this self-diffusivity, consider a neutrally buoyant test sphere present in a viscous suspension of otherwise identical spheres. When the suspension is subjected to an external shear flow, the test particle interacts with the other surrounding particles and, consequently, experiences a series of displacements away from its original streamline. Such displacements, when taken together, will have zero mean but a finite mean square displacement which can be characterized by a shear-induced coefficient of self-diffusion. Since the rate of such interactions is proportional to the shear rate γ, and the length scale of each displacement is comparable to the particle radius a, the diffusion coefficient has a dimensional scaling $\gamma\, a^2$(Eckstein *et al.* 1977). It is important to note that the coefficient of self-diffusion associated with this mechanism is quite different from the shear-induced gradient diffusivity (Leighton & Acrivos 1987b), the latter being the coefficient in the linear relation between the particle flux resulting a non-uniformity in the

particle concentration and the concentration gradient. According to the arguments by Leighton & Acrivos (1987b), such a flux down a concentration gradient arises because a given particle in a sheared suspension experiences a greater number of interactions from the high concentration side than from the other. On the other hand, the mixing of marked spheres in a suspension of uniform concentration is entirely a self-diffusion process. Although the latter is one of the most basic transport processes occurring in sheared suspensions, only a few theoretical and experimental studies of the self-diffusivity have been reported to-date. These include the experimental measurements of the shear-induced self-diffusivity of non-Brownian particles by Eckstein, Bailey & Shapiro (1977), Leighton & Acrivos (1987a) and Phan & Leighton (1993), the computations via Stokesian Dynamics simulations by Bossis & Brady (1987), Phung, Brady & Bossis (1996), Phung (1993) and the theoretical work by Brady & Morris (1997). The results of all these studies are summarized in figures 1.1 & 1.2 (Brady 1997) where the dimensionless self-diffusivities along the velocity gradient and vorticity directions are plotted as a function of the particle concentration ϕ. Clearly, owing to the large scatter in the experimental observations it is difficult to compare directly the experimental and computational results. In addition, in order to understand the nature of the microscopic interactions between the particles, measurements of the self-diffusivity over a wide range of values of the strain $\gamma \Delta t$, where Δt is the time step over which the particle displacement is observed, would

be highly desirable. To our knowledge such measurements have not been attempted thus far.

Similarly, the self-diffusivity of a fluid tracer in non-colloidal concentrated suspensions has not been measured so far inspite of its importance in many industrial and clinical processes. For example, a great deal of literature is available concerning liquid phase mass transport in red blood cell suspensions and on gas and heat transport in suspensions of particles. Zydney and Colton(1988) list about 50 publications on this topic. Although considerable evidence exists that both heat and mass transport in concentrated suspensions can be substantially augmented in shear flow, existing models are not completely adequate for predicting the experimental observations. We believe that the results of this study can be used to estimate the importance of augmented solute transport in the flow of concentrated suspensions, and also that they can provide a basis for a more detailed experimental and theoretical study of this phenomenon.

In this paper we shall present a new method for measuring the self-diffusion coefficient in concentrated suspensions of non-colloidal and non-Brownian particles. This technique is based on the application of spatial correlation procedures to consecutive images of tracer particles in a fixed imaging volume. In the next section, the general idea of the method will be explained, followed by the development of a theoretical framework for analyzing the data. Then, in subsection 2.3 the theory will be applied to the

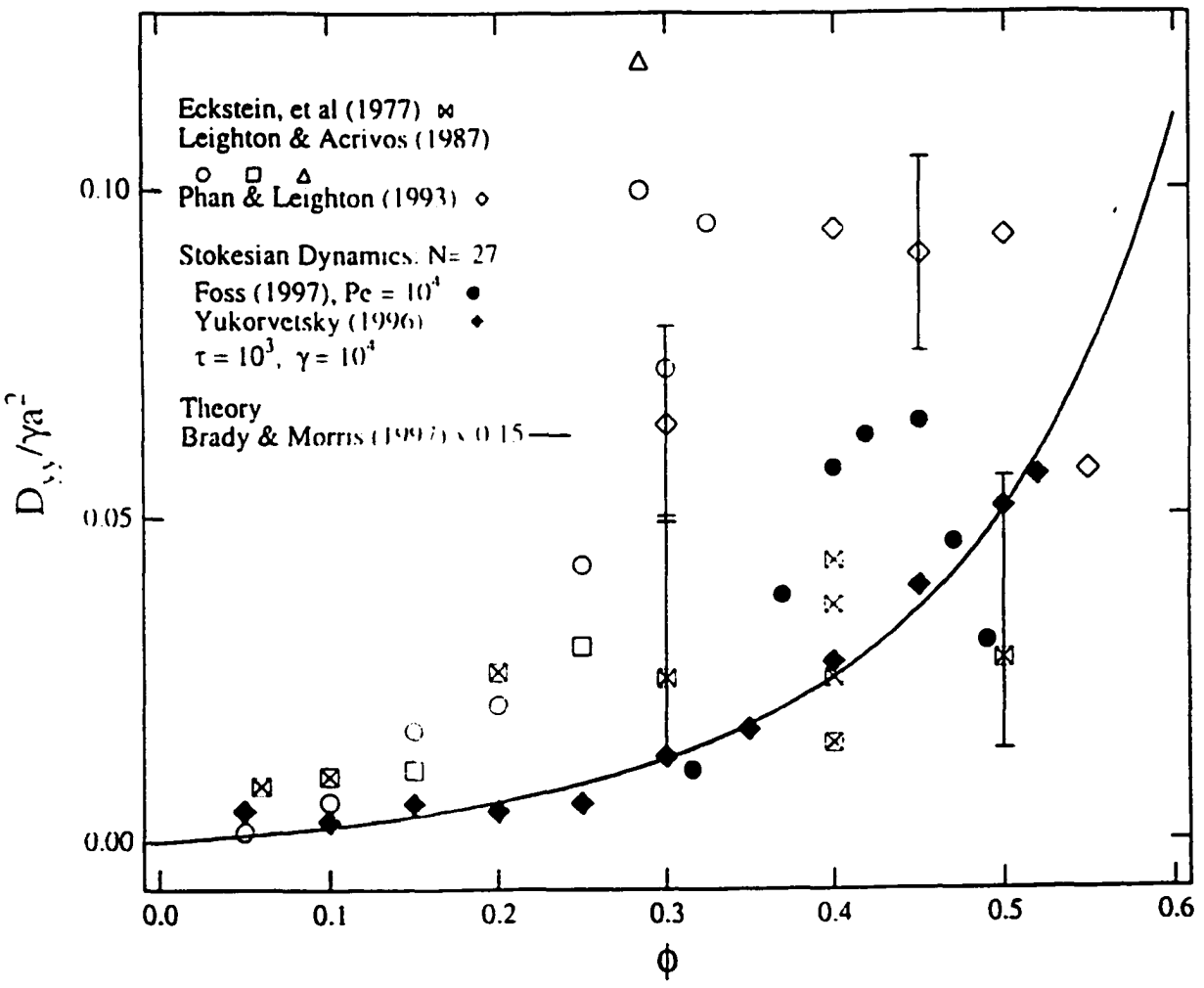

Figure 1.1: Data for the shear-induced particle self-diffusivity along the direction of shear in a simple shear flow collected by Brady(1997) and plotted against the particle volume fraction in the suspension. (Adapted with the permission of Professor J. F. Brady)

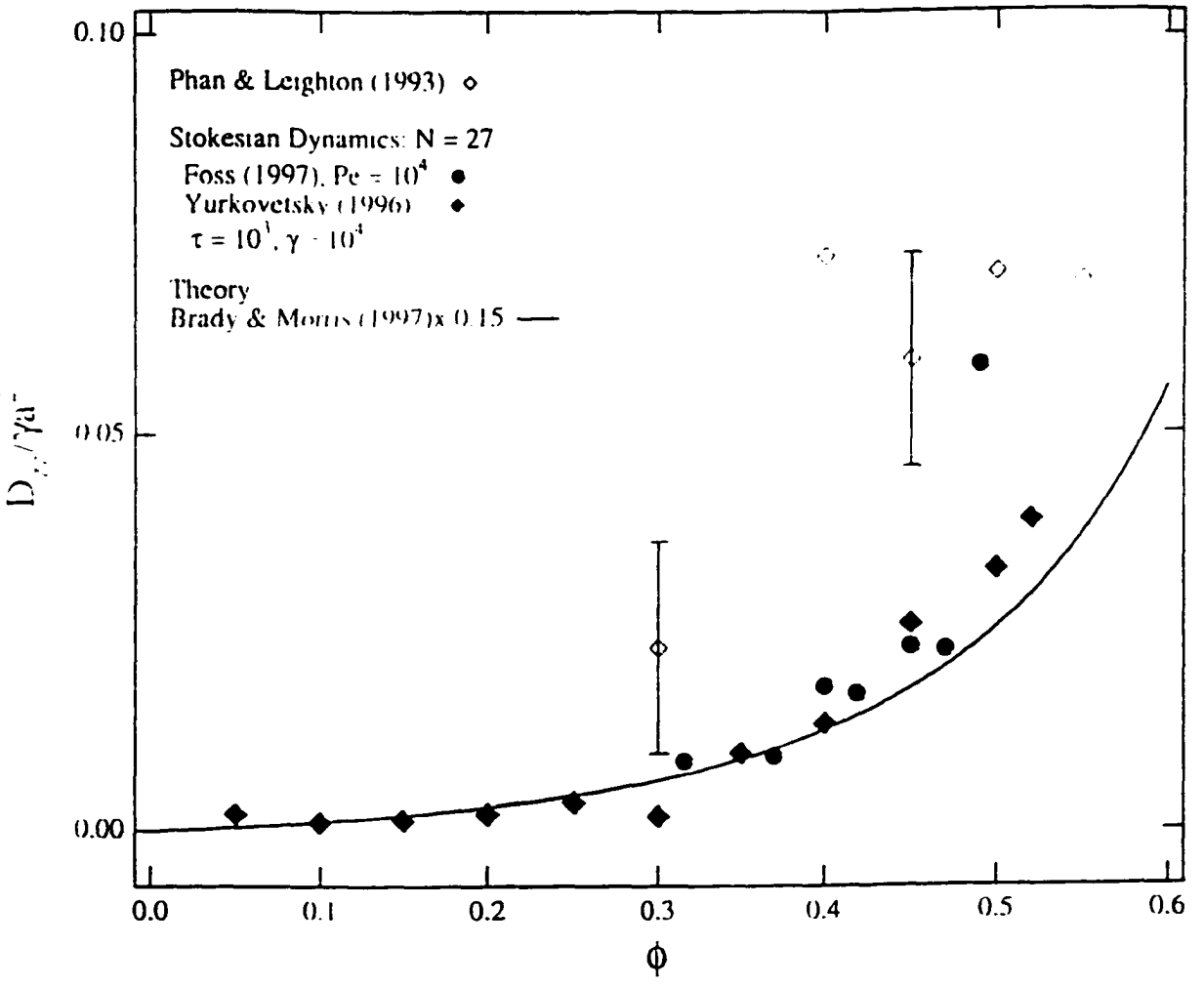

Figure 1.2: Data for the shear-induced particle self-diffusivity along the vorticity axis in a simple shear flow collected by Brady (1997) and plotted against the particle volume fraction in the suspension. (Adapted with the permission of Professor J. F. Brady)

case of a simple shear flow, applicable to the Couette geometry in which we performed our experiments. The third section contains a description of our experimental procedure and the final section is devoted to the results and discussion.

2. The new approach

In this section we shall present the salient features of a simple and accurate experimental technique for measuring the self-diffusion coefficient in concentrated sheared suspensions.

2.1. Basic concepts

We examine the phenomenon of diffusion by investigating the positions of tracer neutrally buoyant spherical particles immersed in a suspension of otherwise identical spheres undergoing shear. The tracers are colored black in order to distinguish them from the surrounding particles, which are refractive index matched with the suspending fluid. The images are taken at a fixed position in the geometry, but, because the suspension is being sheared, the tracers move with the general flow and will stay in the image window only for a limited time. Figure 1.3 shows an example of two successive images taken at a time interval Δt with the bulk flow as indicated so that all the particles move from left to right. The imaging window occupies a two-dimensional

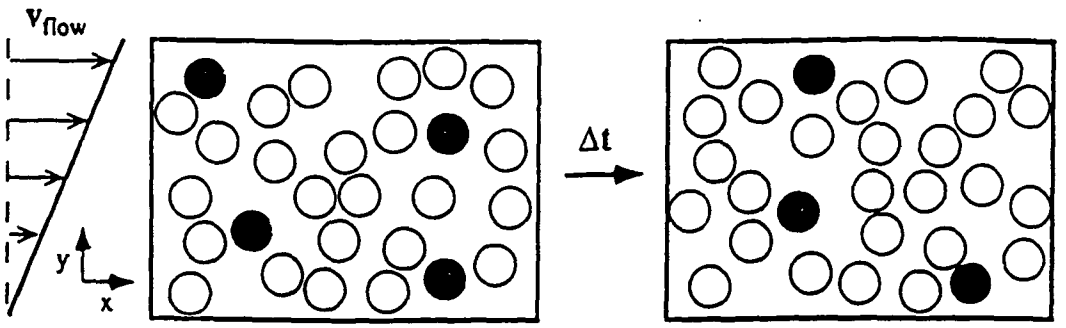

Figure 1.3: Schematic diagrams of two successive images of a fluid element in a sheared suspension.

rectangular area. In an experimental set-up, the window will always be the two-dimensional projection of a three-dimensional fluid volume, because of the finite depth of focus of the optics (This effect will be dealt with in the next subsection and does not change the general considerations to be described below). The black particles in figure 1.3 represent the tracers, while the white ones refer to the refractive index matched particles, which are invisible if the matching is perfect. Particles intersecting the border of the image window are not drawn.

The motion of the non-colloidal particles consists of two parts: a convective motion along the streamlines of the bulk fluid flow and fluctuations due to their hydrodynamic interactions with other particles. The latter give

rise to the shear-induced diffusion, both the self-diffusion and, if present, the gradient diffusion. An essential step in the technique consists of locating all the M tracers in the second image as well as all the N tracers in the first image and then calculating the two-dimensional vectors:

$$\Delta\tilde{\mathbf{x}}_{nm} = (x_m - x_n, y_m - y_n) \qquad n = 1, 2, .., N; m = 1, 2, .., M$$

where $(x_n y_n)$ and (x_m, y_m) refer to the positions of the particle centers in the first and second image, respectively. This results into $N \cdot M$ different two-dimensional displacement vectors $\Delta\tilde{\mathbf{x}}_{nm}$, generally a number too small for performing a meaningful statistical analysis. Figure 1.3, for example, yields 12 vectors. But if the procedure is repeated for a large number of image combinations with the same time-interval, the number of vectors increases rapidly. These data can be used to define the function $C_{2D}(\Delta\tilde{\mathbf{x}}; \Delta t)$, which denotes the number of times a two-dimensional displacement vector $\Delta\tilde{\mathbf{x}}$ appears in the ensemble of images. The function $C_{2D}(\Delta\tilde{\mathbf{x}}; \Delta t)$ thus represents the experimental probability density of finding a vector $\Delta\tilde{\mathbf{x}}$ in the ensemble of images.

The vectors $\Delta\tilde{\mathbf{x}}_{nm}$ can be divided into two different categories. The first contains all the vectors $\Delta\tilde{\mathbf{x}}_{nm}^{auto}$ for which tracer m is the same as n. On these occasions, the particle has not left the image window during the time interval. The second category contains all the cross-correlation vectors $\Delta\tilde{\mathbf{x}}_{nm}^{cross}$, between different tracer particles in consecutive images. For example, assume that N' ($N' \leq N$) particles in the first image of figure 1.3 are present

in the second image as well. Then, the total number of $N \cdot M$ correlation vectors $\Delta\tilde{\mathbf{x}}_{nm}$ consists of N' auto-correlation vectors $\Delta\tilde{\mathbf{x}}_{nm}^{auto}$ and $N \cdot M - N'$ cross-correlation vectors $\Delta\tilde{\mathbf{x}}_{nm}^{cross}$. For the analysis of the particle motion, the auto-correlation vectors $\Delta\tilde{\mathbf{x}}_{nm}^{auto}$ are of interest because they contain information about the displacements of individual particles during the time interval Δt. The cross-correlation vectors are of less interest, although they contain information on the spatial distribution of the tracer particles in the fluid.

Unfortunately, it is impossible to tell a priori whether a vector $\Delta\tilde{\mathbf{x}}_{nm}$ belongs to the first or to the second category. This would only be possible if the time interval was very small, so that one could easily detect where the individual particles have gone. In the general case of larger time intervals, however, this would be very difficult and thus complicate the interpretation of the images. Fortunately, our technique does not need this information in evaluating the self-diffusivity. Specifically, we shall show in the next section that the auto-correlation and cross-correlation contributions to $C_{2D}(\Delta\tilde{\mathbf{x}}; \Delta t)$ are of a different nature, and therefore can be separated statistically. Then, once the auto-correlation part has been extracted from the correlation vectors, the diffusive motion of individual particles can be analyzed. Before proceeding though, let us first generalize the concept to the full three-dimensional formulation.

2.2. Theoretical formulation in three-dimensions

In the experimental system, the two-dimensional images are the projection of a three-dimensional fluid volume. The effects of this projection onto a finite-sized two-dimensional image window have not been taken into account so far and will be analyzed in this section. As will be shown, this slightly complicates the interpretation of the experimentally determined function $C_{2D}(\Delta\tilde{\mathbf{x}};\Delta t)$ mentioned in the previous section, but, after carefully considering these effects, $C_{2D}(\Delta\tilde{\mathbf{x}};\Delta t)$ can be directly related to the actual three-dimensional probability density of the particles which is the quantity of primary interest. No a priori assumptions on the nature of the particle motion have to be made.

The effect of the projection is that the three-dimensional vectors $\Delta\mathbf{x} \equiv (\Delta x, \Delta y, \Delta z)$ in the fluid volume become two-dimensional vectors $\Delta\tilde{\mathbf{x}} \equiv (\Delta x, \Delta y)$ on the image. Thus, in determining the function $C_{2D}(\Delta x, \Delta y; \Delta t)$ we are, in essence, counting the number of two-dimensional vectors $(\Delta x, \Delta y)$ appearing in the images by adding all the three-dimensional vectors $(\Delta x, \Delta y, \Delta z)$, regardless of the value of the out of plane distance Δz. This can be formulated mathematically as

$$C_{2D}(\Delta x, \Delta y; \Delta t) = \int C_{3D}(\Delta x, \Delta y, \Delta z; \Delta t) d\Delta z \qquad (1.1)$$

where $C_{3D}(\Delta x, \Delta y, \Delta z; \Delta t)$ is the full three-dimensional spatial correlation probability of the ensemble of images, representing the chance of finding a displacement $(\Delta x, \Delta y, \Delta z)$. Off hand, it might appear that $C_{3D}(\Delta x, \Delta y, \Delta z; \Delta t)$

should equal $P(\Delta\mathbf{x};\Delta t,\mathbf{x})$, where $P(\Delta\mathbf{x};\Delta t,\mathbf{x})$ is defined as the theoretical probability density of finding two particles with center to center vector $\Delta\mathbf{x}$ after a given time interval Δt. However, owing to experimental limitations, the two functions are related by

$$C_{3D}(\Delta\mathbf{x};\Delta t)=\int\int\int_V S(\mathbf{x},\mathbf{x}+\Delta\mathbf{x})P(\Delta\mathbf{x};\Delta t,\mathbf{x})d\mathbf{x} \qquad (1.2)$$

where $S(\mathbf{x},\mathbf{x}+\Delta\mathbf{x})$ to be discussed further on in this section, is the experimental probability of detecting the particles referred to above.

The function $C_{3D}(\Delta x,\Delta y,\Delta z;\Delta t)$ thus represents the ensemble averaged experimental sampling of the probability density $P(\Delta\mathbf{x};\Delta t,\mathbf{x})$ and will be analyzed in terms of $P(\Delta\mathbf{x};\Delta t,\mathbf{x})$. Next, following the same arguments as in section 2.1, we split the probability density function $P(\Delta\mathbf{x};\Delta t,\mathbf{x})$ into two parts. The first, termed the spatial auto-correlation in section 2.1, refers to the probability that the same particle has been displaced by $\Delta\mathbf{x}$. In terms of the probability distribution, it is equivalent to the transition probability density $P^{trans}(\Delta\mathbf{x};\Delta t,\mathbf{x})$ of a particle being displaced by $\Delta\mathbf{x}$ during the time Δt, starting from position $\mathbf{x}$. The function $P^{trans}(\Delta\mathbf{x};\Delta t,\mathbf{x})$ contains fundamental information on the particle motions.

The second contribution to the total probability density $P(\Delta\mathbf{x};\Delta t,\mathbf{x})$ refers to the probability density of finding two different tracer particles at relative positions $\Delta\mathbf{x}$ after the time-interval Δt. This part of the distribution probability density will be denoted by $P^{distr}(\Delta\mathbf{x};\Delta t)$, since it is linked to the distribution of different tracer particles over the image window. At steady

state, $P^{distr}(\Delta\mathbf{x};\Delta t)$ can then be expressed as:

$$P^{distr}(\Delta\mathbf{x};\Delta t) = \int\int\int P_1(\mathbf{x})P_2(\mathbf{x}+\Delta\mathbf{x};\Delta t:\mathbf{x})d\mathbf{x} \qquad (1.3)$$

where $P_1(\mathbf{x};t)$ is the probability density of finding a tracer at $\mathbf{x}$ and $P_2(\mathbf{x}+\Delta\mathbf{x};\Delta t:\mathbf{x})$ is the conditional probability density of another tracer being on the position $\mathbf{x}+\Delta\mathbf{x}$ after a time-interval Δt given that the first tracer was at $\mathbf{x}$. Also, the domain of integration is the whole image volume. Of course, if the tracers are distributed homogeneously over the window, P_1 is constant and can be taken out of the integration. Having thus defined the probability density functions $P^{trans}(\Delta\mathbf{x};\Delta t,\mathbf{x})$ and $P^{distr}(\Delta\mathbf{x};\Delta t)$, we proceed with the derivation of their relations with the spatial correlation function $C_{3D}(\Delta\mathbf{x};\Delta t)$ (equation (1.2)), which in turn can be used to determine $C_{2D}(\Delta\tilde{\mathbf{x}};\Delta t)$ via equation (1.1). The main effect to consider is the fact that the observed fluid volume is of limited size in all three directions and that the image analysis introduces some errors in detecting the particles in the images. Both factors influence the sampling function $C_{3D}(\Delta\mathbf{x};\Delta t)$.

First, let us investigate the effect of the window boundaries in the x- and y-direction. Note that if the image window has width W and height H, the two-dimensional displacement vector $\Delta\tilde{\mathbf{x}}$ can never exceed the limits $-W < \Delta x < W$ and $-H < \Delta y < H$. As an extra complication, due to the limited size of the window, the chances of finding a large vector $(\Delta x, \Delta y)$ are lower than finding small ones. When both Δx and Δy are positive, this windowing effect is illustrated in figure 1.4 which shows that, within the fixed

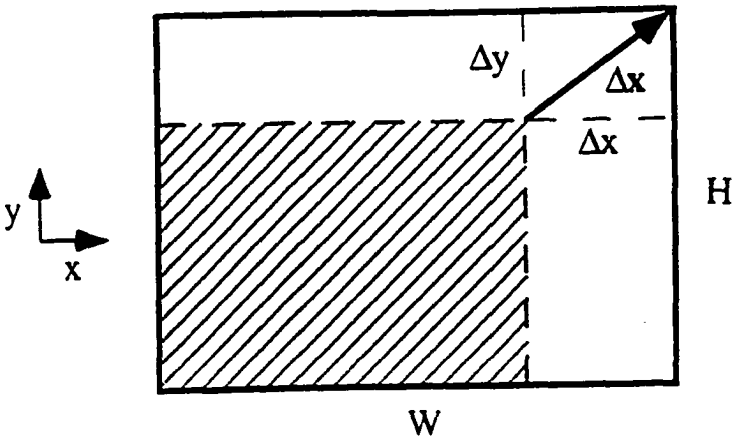

Figure 1.4: Schematic of the windowing effect on the correlation function for positive Δx and Δy.

image window, the vector $(\Delta x, \Delta y)$ can only be realized starting from the shaded fraction of the window area, otherwise the end of the vector would point out of the window. Thus, the starting two-dimensional vector $\tilde{\mathbf{x}}$ must lie inside the region bounded by

$$\begin{aligned} \frac{1}{2}(|\Delta x| - \Delta x) < \quad & x \quad < W - \frac{1}{2}(|\Delta x| + \Delta x) \\ \frac{1}{2}(|\Delta y| - \Delta y) < \quad & y \quad < H - \frac{1}{2}(|\Delta y| + \Delta y) \end{aligned}$$

for the two-dimensional vector $\tilde{\mathbf{x}} + \Delta\tilde{\mathbf{x}}$ to be observed. The absolute values have to be used, because the windowing effect limits the effective size of the image window also for two-dimensional displacement vectors $\Delta\tilde{\mathbf{x}}$ with negative components.

In addition, it is not obvious that all the tracers within the fluid volume will be detected under all circumstances, as occurs, for example, when the lighting is inhomogeneous or when the tracers are too closely together to be separated by both the human eye and sophisticated image analysis software. Therefore, it is reasonable to introduce the detection probability $S_{xy}(x, y)$ which varies over the image window. Ideally, when all the tracers can be detected, S_{xy} equals unity at all positions within the image window. Although this can not be realized in practice, it is still possible to make S_{xy} almost a constant by carefully manipulating the lighting arrangement. But even so, its value will generally be slightly smaller than unity because, in any large collection of acquired images some of them will contain tracers that appear to be overlapping and cannot be located accurately.

The third dimension of the fluid volume is the z-direction, perpendicular to the object plane. Here, a finite volume around the focal plane of the optics will be observed due to the finite depth of focus ($d.o.f.$). Specifically, if $z = 0$ denotes the location of the focal plane, the depth of focus is usually defined so that the z-values at which tracer particles can be distinguished range from $-\frac{1}{2}d.o.f.$ to $+\frac{1}{2}d.o.f.$. As a result, the detection probability S_z will always be a very strong function of z. Even if we assume that S_z does not depend on the x- and y- positions (which is reasonable if the $d.o.f.$ is small compared to the window size), it will, by definition, have its maximum in the focal plane and vanish at $z = \pm d.o.f.$ where the tracers can no longer be distinguished

from their surroundings.

Using the arguments presented in the preceding paragraphs, equation (1.2) can be written in the following way:

$$
\begin{aligned}
C_{3D}(\Delta x, \Delta y, \Delta z; \Delta t) = & \\
& \int_{z_{min}}^{z_{max}} \int_{y_{min}}^{y_{max}} \int_{x_{min}}^{x_{max}} [\hat{n} S_{xy}(x,y) S_z(z) P_1(\mathbf{x})] \cdot \qquad (1.4) \\
& \qquad \left[\hat{n} S_{xy}(x+\Delta x, y+\Delta y) S_z(z+\Delta z) P^{trans}(\Delta \mathbf{x}; \Delta t, \mathbf{x})\right] \, dx \, dy \, dz \\
+ & \int_{z_{min}}^{z_{max}} \int_{y_{min}}^{y_{max}} \int_{x_{min}}^{x_{max}} [\hat{n} S_{xy}(x,y) S_z(z) P_1(\mathbf{x})] \cdot \\
& \qquad [\hat{n} S_{xy}(x+\Delta x, y+\Delta y) S_z(z+\Delta z) P_2(\mathbf{x}+\Delta \mathbf{x}; \Delta t : \mathbf{x})] \, dx \, dy \, dz
\end{aligned}
$$

where

$$
\begin{aligned}
x_{\min} &= x_0 - \frac{1}{2}W + \frac{1}{2}(|\Delta x| - \Delta x), \; x_{\max} = x_0 + \frac{1}{2}W - \frac{1}{2}(|\Delta x| + \Delta x), \\
y_{\min} &= y_0 - \frac{1}{2}H + \frac{1}{2}(|\Delta y| - \Delta y), \; y_{\max} = y_0 + \frac{1}{2}H - \frac{1}{2}(|\Delta y| + \Delta y), \\
z_{\min} &= z_0 - \frac{1}{2}dof + \frac{1}{2}(|\Delta z| - \Delta z), \; z_{\max} = z_0 + \frac{1}{2}dof - \frac{1}{2}(|\Delta z| + \Delta z)
\end{aligned}
$$

and $\hat{n}$ is the average number of tracers in the fluid volume which is introduced in order to normalize the probability density functions. In addition, (x_0, y_0, z_0) denotes the center of the object volume within which the measurements are being made. Both integrands in equation (1.4) involve a product of two terms: the first contains the probability that a tracer is observed at position $\mathbf{x}$ and the second the probability that a tracer –either the same (P^{trans}) or another (P_2)– is observed at position $\mathbf{x} + \Delta\mathbf{x}$ after the time-interval Δt. The integration over x, y and z originates from the finite size of the object volume, discussed earlier.

The general equation (1.4) can be simplified by letting $P_1(\mathbf{x})$ be constant, which is permissible if the gradients in the concentration of the tracer particles are negligible on the scale of the window size. In addition, as was stated earlier, $S_{xy}(x, y)$ will be constant under appropriate experimental conditions. Consequently, equation (1.4) becomes

$$C_{3D}(\Delta\mathbf{x}; \Delta t) =$$
$$K_1\, \hat{n}^2 \int_{z_{min}}^{z_{max}} \int_{y_{min}}^{y_{max}} \int_{x_{min}}^{x_{max}} S_z(z) S_z(z + \Delta z) P^{trans}(\Delta\mathbf{x}; \Delta t, \mathbf{x})\, dx\, dy\, dz$$
$$+ K_1\, \hat{n}^2 \int_{z_{min}}^{z_{max}} \int_{y_{min}}^{y_{max}} \int_{x_{min}}^{x_{max}} S_z(z) S_z(z + \Delta z) P_2(\mathbf{x} + \Delta\mathbf{x}; \Delta t : \mathbf{x})\, dx\, dy\, dz \quad (1.5)$$

where $K_1 = P_1 \cdot S_{xy}^2$ is an $O(1)$ constant. Therefore, on substituting equation (1.5) into equation (1.1) we obtain that

$$C_{2D}(\Delta\tilde{\mathbf{x}}; \Delta t) = \quad (1.6)$$
$$K_1\, \hat{n}^2 \int_{-dof}^{+dof} \int_{z_{min}}^{z_{max}} \int_{y_{min}}^{y_{max}} \int_{x_{min}}^{x_{max}} S_z(z) S_z(z + \Delta z) P^{trans}(\Delta\mathbf{x}; \Delta t, \mathbf{x})\, dx\, dy\, dz\, d\Delta z$$
$$+ K_1\, \hat{n}^2 \int_{-dof}^{+dof} \int_{z_{min}}^{z_{max}} \int_{y_{min}}^{y_{max}} \int_{x_{min}}^{x_{max}} S_z(z) S_z(z + \Delta z) P_2(\mathbf{x} + \Delta\mathbf{x}; \Delta t : \mathbf{x})\, dx\, dy\, dz\, d\Delta z$$

where the integration over Δz is performed from the minimum ($-d.o.f.$) to the maximum ($+d.o.f.$) possible distance between tracers in the Δz-direction. The second term on the right hand side of equation (1.6) can be simplified further by considering special forms for $P_2(\mathbf{x} + \Delta\mathbf{x}; \Delta t)$. Although some comments on this subject will be made at the end of the next subsection, a thorough analysis is left for the future work, which concerns exclusively the first term. Note that, in arriving at equation (1.6), no a priori assumptions on

the transition probability density $P^{trans}(\Delta\mathbf{x};\Delta t,\mathbf{x})$ have been made. In the next section, equation (1.6) will be evaluated when the transition probability is that for the diffusive motion of tracers in a simple shear flow, on which our experimental work is focused.

2.3. The evaluation of self-diffusion coefficients in a simple shear flow

The analysis discussed in the previous section directly links the experimental results to the transition probability density function of the tracers. Different theoretical hypotheses for $P^{trans}(\Delta\mathbf{x};\Delta t,\mathbf{x})$ can be introduced into equation (1.4) to check their validity. In this paper we concentrate on the topic of self-diffusion in a concentrated suspension undergoing simple shear flow. Previous experiments (Leighton & Acrivos(1987a), Eckstein *et al.* (1977)) have shown that, for sufficiently long time-steps Δt, the motion of the particles can be viewed as a diffusion process with different diffusion coefficients along the characteristic flow axes (flow, velocity gradient and vorticity direction). In such a case, the transition probability density $P^{trans}(\Delta\mathbf{x};\Delta t,\mathbf{x})$ satisfies the general convective diffusion equation:

$$\frac{\partial P^{trans}}{\partial t} = -\nabla\cdot(\mathbf{v}\,P^{trans}) + \nabla\cdot\mathbf{D}\cdot\nabla P^{trans} \qquad (1.7)$$

with initial condition $P^{trans}(\Delta\mathbf{x};0,\mathbf{x}) = \delta(\Delta\mathbf{x})$, where $\mathbf{v}$ is the convective bulk particle velocity. For a stationary simple shear flow $\mathbf{v} = (\gamma y, 0, 0)$, with the x-axis in the flow direction and the y-axis in the velocity gradient

direction. The diffusion tensor **D** is defined by

$$\langle \Delta \mathbf{x}\, \Delta \mathbf{x} \rangle \sim 2\, \mathbf{D}\, \Delta t = 2 \begin{bmatrix} D_{xx} & D_{xy} & 0 \\ D_{yx} & D_{yy} & 0 \\ 0 & 0 & D_{zz} \end{bmatrix} \Delta t \tag{1.8}$$

D_{xx}, D_{yy} and D_{zz} being the diffusion coefficients in the different directions. Due to symmetry, all the off-diagonal elements of **D** are zero except for D_{xy} and D_{yx} which are equal(c.f. Morris & Brady (1996)). The solution of equations (1.7) and (1.8) can be written in the form (c.f. van Kampen (1992)):

$$P^{trans}(\Delta \mathbf{x}; \Delta t, \mathbf{x}) = \frac{1}{(2\pi)^{\frac{3}{2}} \sigma_x \sigma_y \sigma_z} \tag{1.9}$$
$$\exp\left(- \frac{(\Delta x - \frac{1}{2}\gamma \Delta t (\Delta y + 2y) - \Delta y \frac{D_{xy}}{D_{yy}})^2}{2\sigma_x^2} - \frac{(\Delta y)^2}{2\sigma_y^2} - \frac{(\Delta z)^2}{2\sigma_z^2} \right)$$

where

$$\sigma_x^2 = 2D_{xx}\Delta t \left(1 + \frac{1}{12}\gamma^2 \Delta t^2 \frac{D_{yy}}{D_{xx}} - \frac{D_{xy}^2}{D_{xx} D_{yy}} \right), \ \sigma_y^2 = 2D_{yy}\Delta t \text{ and } \sigma_z^2 = 2D_{zz}\Delta t$$

On inserting equation (1.9) into equation (1.6) and integrating with respect to x and y, we obtain

$$C_{2D}(\Delta x, \Delta y; \Delta t) =$$
$$K_1\, \hat{n}^2\, \psi(\Delta t)\, \chi(\Delta t; dof)\, (W - |\Delta x|) \cdot \exp\left(-\frac{(\Delta y)^2}{2\sigma_y^2} \right) \cdot \frac{\sqrt{\pi}\,\sigma_x}{\sqrt{2}\,\gamma \Delta t} \cdot \tag{1.10}$$
$$\left(\operatorname{erf}\left[\frac{\Xi_1(\Delta x, \Delta y; \Delta t)}{\sqrt{2}\,\sigma_x} \right] - \operatorname{erf}\left[\frac{\Xi_2(\Delta x, \Delta y; \Delta t)}{\sqrt{2}\,\sigma_x} \right] \right)$$
$$+ K_1\, \hat{n}^2\, (W - |\Delta x|)\, (H - |\Delta y|) \int_{-dof}^{dof} \int_{z_{min}}^{z_{max}} S_z(z) S_z(z + \Delta z) P_2(\Delta \mathbf{x}; \Delta t)\, dz\, d\Delta z$$

where

$$\chi(\Delta t; dof) = \int_{-dof}^{dof} \int_{z_{min}}^{z_{max}} S_z(z) S_z(z + \Delta z) \exp\left(-\frac{(\Delta z)^2}{2\sigma_z^2}\right) dz\, d\Delta z, \quad (1.11)$$

$$\psi(\Delta t) = \frac{1}{(2\pi)^{\frac{3}{2}} \sigma_x \sigma_y \sigma_z} \quad (1.12)$$

while $\Xi_1(\Delta x, \Delta y; \Delta t) = \Delta x - \frac{1}{2}\gamma \Delta t(2y_0 - H + |\Delta y|) - \Delta y \frac{D_{xy}}{D_{yy}}$ *and*
$\Xi_2(\Delta x, \Delta y; \Delta t) = \Delta x - \frac{1}{2}\gamma \Delta t(2y_0 + H - |\Delta y|) - \Delta y \frac{D_{xy}}{D_{yy}}$.

Equation (1.10) describes the shape of the experimentally determined function $C_{2D}(\Delta x, \Delta y; \Delta t)$ for the case of a diffusive tracer motion in a simple shear flow. As will be shown in the more detailed description of the data analysis in section 3.3, this expression can be simplified further and then used to calculate the diffusion coefficient D_{yy} by analyzing only the width of the auto-correlation peak of $C_{2D}(\Delta x, \Delta y; \Delta t)$ in the Δy-direction. Note that the amplitude of the auto-correlation part (first term) depends on the window size, the time step (through χ and ψ) and on the depth of focus of the optical system (through χ).

The preceding analysis can also be performed when the image plane is in the Δx-Δz-plane, which is the case when the suspension is viewed from the velocity gradient direction. Here, however, the counterpart of equation (1.10) is simply:

$$C_{2D}(\Delta x, \Delta z; \Delta t) =$$
$$K_2\, \hat{n}^2\, \psi(\Delta t)\, \xi(\Delta x, \Delta t; dof)\, (W - |\Delta x|)\, (|H - \Delta z|) \exp\left(-\frac{(\Delta z)^2}{2\sigma_z^2}\right) \quad (1.13)$$

$$+ K_2 \hat{n}^2 (W - |\Delta x|)(H - |\Delta z|) \int_{-dof}^{dof} \int_{y_{min}}^{y_{max}} S_y(y) S_y(y + \Delta y) P_2(\Delta \mathbf{x}; \Delta t)\, dy\, d\Delta y$$

where

$$\xi(\Delta x, \Delta t; dof) = \int_{-dof}^{dof} \int_{y_{min}}^{y_{max}} S_y(y) S_y(y + \Delta y) \cdot \exp\left(- \frac{(\Delta x - \frac{1}{2}\gamma \Delta t(\Delta y + 2y) - \Delta y \frac{D_{xy}}{D_{yy}})^2}{2\sigma_x^2} - \frac{(\Delta y)^2}{2\sigma_y^2} \right) dy\, d\Delta y \tag{1.14}$$

and $K_2 = P_1 \cdot S_{xz}^2$ is a constant which is slightly different from K_1. The above differs from equation (1.10) in the sense, that the shape of the auto-correlation peak in the Δz-direction is simply that of a Gaussian peak, with a width that only depends on the diffusion coefficient D_{zz}. Consequently, equation (1.13) enables one to calculate the diffusion coefficient D_{zz} by analyzing the width of the auto-correlation peak of $C_{2D}(\Delta x, \Delta y; \Delta t)$ in the Δz-direction. Equation (1.14) is somewhat more complicated than equation (1.11) because, now ξ depends on both Δx and Δt.

Of course, the cross-correlation parts of equations (1.10) and (1.13) cannot be neglected in calculating the diffusion coefficients from the experimentally obtained functions C_{2D} because this part influences the shape of the correlation function in the region of the auto- correlation peak and must be subtracted out during the fitting procedures. To achieve this we recall that, as was mentioned in section 2.2, $P_2(\Delta \mathbf{x}; \Delta t)$ contains information about the distribution of different particles in consecutive images and is therefore closely related to the pair-distribution function. Symmetry arguments, therefore, are sufficient to eliminate the cross-correlation term in a simple shear flow.

Specifically, as shown in figure 1.5, the Δx-Δy-plane on which our function is measured can be divided into four quadrants with the original position of the tracer being at the origin so that, in simple shear, the flow in quadrants II and IV is compressive and in quadrants I and III extensional. But, since the flow in quadrants I and III is equivalent and similarly in quadrants II and IV, the pair-distribution function has an obvious symmetry in that each point $A(\Delta x, \Delta y)$ has a counterpart $A'(-\Delta x, -\Delta y)$ where the pair-distribution function is the same. This symmetry should also apply to the function $P_2(\Delta \mathbf{x}; \Delta t)$ and, as will be shown in section 3.3, this argument enables one to eliminate the cross-correlation contribution from the measured experimental data in an elegant way.

2.4. Previous experimental work

The general idea of the technique described above is in some respects similar to other well-known experimental methods, for example Particle Image Velocimetry (PIV), where in order to measure the velocity field in complex flow geometries, the fluid is seeded with small tracers which accurately follow the flow because of their small size. One difference, however, is that, whereas PIV uses very small time intervals Δt between the images to calculate velocity vectors, the time-intervals are considerably larger in the present application so as to maximize the displacements of the tracers.

On the other hand, Eckstein *et al.* (1977) and Leighton & Acrivos (1987a) examined the phenomenon of self-diffusion by investigating the motion of a

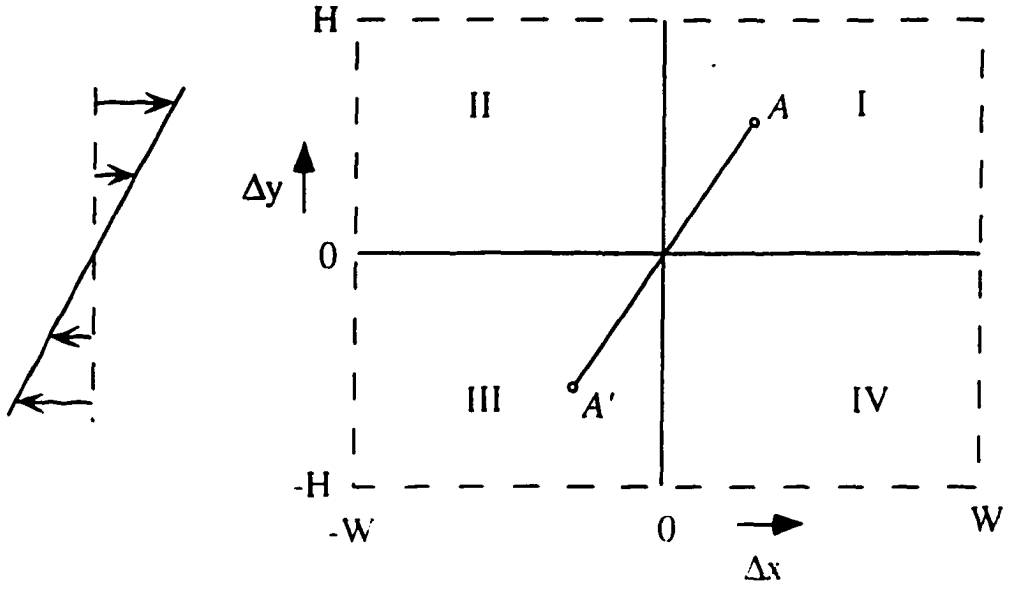

Figure 1.5: Schematic of four quadrants in the Δx-Δy-plane on which the function C_{2D} is measured. The origin refers to the original position of the tracer.

single labeled sphere immersed in a suspension of otherwise identical spheres being sheared in a Couette device. In their technique, the radial position (the velocity gradient direction) of the labeled sphere was measured after each rotation (Eckstein *et al.*) or inferred from the time taken for the particle to complete a transit of the device (Leighton & Acrivos). These data were then related to the random walk in the radial direction. Recently, Phan & Leighton (1993) also measured the self-diffusivity in the vorticity direction by observing the vertical position of a marked sphere each time it passed an observation window. It is worth remarking at this point that in the experiments of both Leighton & Acrivos (1987a) and Phan & Leighton (1993), the

strain $\gamma\Delta t$ was at least of $O(1)$, which, as will be shown presently, is more than an order of magnitude larger than in our experiments.

3. Experimental work

In this section we present the experimental details of our measurements of the shear-induced coefficient of particle self-diffusion. The basic approach consisted of evaluating the positions of tracer particles, immersed in a suspension of otherwise identical spheres, being sheared in a narrow gap Couette device.

3.1. Apparatus and Materials

The experiments were performed in a narrow gap cylindrical Couette device, shown in figure 1.6, which consisted of two cylinders made of high quality plexiglass. The inner radius of the outer stationary cylinder (R_O) was 8.224 cm and the outer radius of the inner rotating cylinder (R_I) was 7.542 cm, giving a gap size equal to 0.682 cm. The inner cylinder was mounted on a shaft, which in turn was mounted on a computer controlled feedback motor (ID Corp., California). Also, the shaft was aligned accurately with two bearings separated by O-rings. A great advantage of this design is that its transparency enabled us to provide uniform lighting to the imaging volume.

The particles used in the experiments were class 4F acrylic spheres obtained from ICI. Their density was measured to be 1.172 g/ml and the

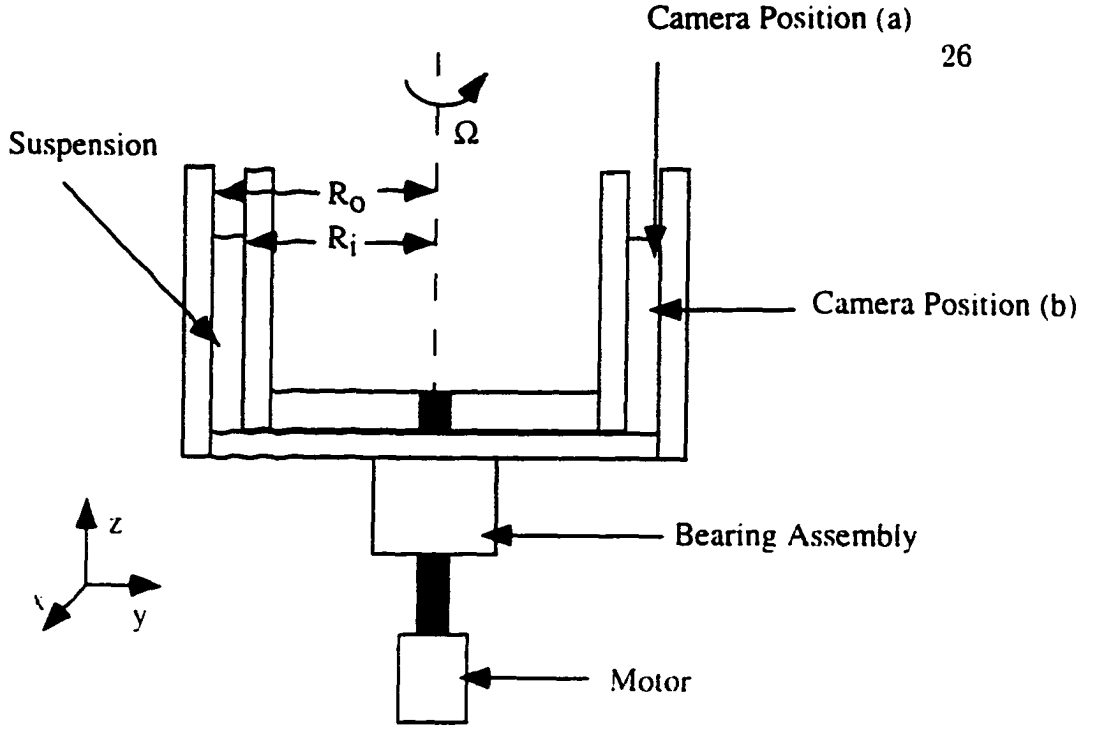

Figure 1.6: Schematic of the Couette device and the camera positions (a) and (b) for observations in, respectively, the velocity gradient and vorticity directions.

spheres containing air bubbles were removed by density segregation. The polydisperse material was sieved many times to obtain the diameter range 90 ± 15 μm. Following the recipe of Krishnan *et al.* (1996), a suspension of these particles was made using a mixture of 77.38% Triton X-100, 9.23% water and 13.39% anhydrous zinc chloride (weight percentages) which matched the refractive index and density of the acrylic spheres. The pure suspending fluid had a viscosity of 3.4 Pa·s at the operating temperature of 23°C. Tracer particles were prepared by dyeing part of the acrylic spheres with RIT liquid fabric dye and their density was also found to be close to 1.172 g/ml. A small amount of the tracer particles (typically 0.4 vol.% in our experiments)

were then added to the suspension. The suspension was sheared for several hours to achieve a uniform concentration and to drive out any air bubbles. The experiments were carried out at two shear rates (0.78 s^{-1} and 1.8 s^{-1}) for particle volume fractions of 20%, 30%, 40% and 50%.

The particles used in the fluid diffusivity experiments were class B728 acrylic spheres obtained from Zenica Resins. These were sieved to obtain a uniform fraction in the size range 300 - 350 μm. Tracer particles were of the same class in the size range 25 - 38 μm. Here, the experiments were carried out at two shear rates (0.78 s^{-1} and 1.8 s^{-1}) for the particle volume fraction 30%, 40% and 50%.

3.2. The Image Analysis

The motion of the tracer particles was observed by viewing two small volumes of the suspension from positions (a) and (b), shown in figure 1.6, using a high resolution (1008 × 1018 pixels) CCD camera (Kodak MegaPlus ES1.0) with Infinity Optics (8× magnification). For lighting we used a Fiber Optic Illuminator (Cole Parmer Instrument Company) that provided an excellent contrast in the image. The camera was mounted on a three-dimensional traversing system, which allowed us to focus the camera precisely at the desired locations. Images from the CCD camera were passed via an 8-bit digital video signal to a dedicated image acquisition and processing board (Oculus F64 by Coreco Inc.) which operated on a personal computer equipped with a 200MHz Intel Pentium Processor. We programmed the frame buffer arrays

of the F64 board to enable the acquisition of 5 consecutive images at equal time intervals Δt (with $\Delta t_{\min} = 55$ msec) before storing the images into the hard disk of the computer. This program was typically run with 100 loops to acquire and store 500 images automatically. The grabbing times of all the images were stored for further analysis.

We used the positions (a) and (b), shown in figure 1.6, to measure the self-diffusion coefficients in the velocity gradient and in the vorticity directions respectively. When viewing from position (a), the center of the imaging volume was kept at 1 mm below the top interface and at 1.5 mm inside the outer wall of the Couette gap. When viewing from position (b) the center of the fluid element $W \times H \times d.o.f.$ of the suspension was chosen 1.7 cm above the bottom and 1 mm inside the outer wall of the Couette gap. These positions were chosen to reduce the wall effects as far as possible. The cross-sectional area, $W \times H$, was calculated using the known magnification of the camera optics and in our experiments was found to be 1.17 mm$\times$1.18 mm. The depth of focus, $d.o.f.$, was determined by viewing a 45° inclined plane through the camera with the preset optics. The inclined plane had four sets of target columns containing different numbers of line pairs per millimeter. The resolution appropriate for the given magnification was then chosen and the distance up to which the line pairs were distinctly visible was measured. This distance was read from either the computer monitor or the scale on the inclined plane. Using this technique, the depth of focus was found to be

425 ± 25 μm.

The positions of the tracer particles in each digitized image were accurately determined using the imaging software (Visilog 5.1 by Noesis Vision Inc.). This software stretched the pixel-grey value dynamic range (process called equalization) to make the details more visible and then removed the unwanted small scale noise. After running a binarization operation, border particles were eliminated and analysis procedures were performed on the dark objects in the image. These procedures involved the calculation of the areas, sphericities, blackness and positions of the dark objects. If the properties met our pre-set criteria, an object was counted as being a tracer and the position of its center was stored in a file. In this way, all the images were scanned and all the tracers and their locations were identified.

For our self-diffusion measurements, a large number of images were taken for each run in order to ensure good ensemble averaging. Typically, we acquired 500 images. The positions of the tracers, as obtained from the measurements described above, were then used to generate the correlation functions C_{2D} for each set. The method for generating these functions and evaluating the self-diffusion coefficients will now be described.

3.3. The data analysis

The data on the positions of all the tracer particles in the images were used to calculate the correlation function $C_{2D}(\Delta x, \Delta y; \Delta t)$ in the following way. For the total ensemble, the two-dimensional displacement vectors $(\Delta x_{nm}, \Delta y_{nm})$

were calculated for all combinations of the tracers in consecutive images, as described in section 2.1. The Δx-Δy-domain ($-W \leq \Delta x \leq W$ and $-H \leq \Delta y \leq H$) was discretized in $N_{\Delta x} \times N_{\Delta y}$ small area elements, usually called numerical bins. All the vectors $(\Delta x_{nm}, \Delta y_{nm})$ were put into the corresponding numerical bin. The number of vectors in each bin was then divided by the number of images, N_{ima}, and by the area covered by each numerical bin, $2\,W/N_{\Delta x} \cdot 2\,H/N_{\Delta y}$, to arrive at the normalized value of the correlation function $C_{2D}(\Delta x, \Delta y; \Delta t)$ at the position of the center of the bin. The normalization procedure is necessary to obtain the correct value if numerical integration is performed and to allow comparison with the theoretical predictions of equations (1.10) and (1.13). The number of bins $N_{\Delta x} \times N_{\Delta y}$ must be small enough in order for each bin to contain a sufficient number of vectors for further analysis, but large enough to provide information on the behaviour of the correlation function at small length scales.

From each ensemble of images, the correlation function could be obtained for different time-steps, by not only comparing consecutive images at a time interval Δt, but by also analyzing image combinations at other intervals $(2 \cdot \Delta t, 3 \cdot \Delta t)$ within one grabbing sequence of 5 images.

Using the data analysis procedures described above, three-dimensional plots could be generated of the function $C_{2D}(\Delta x, \Delta y; \Delta t)$ on the Δx-Δy-plane. Because in our experimental set-up the particles moved from left to right due to convection, the auto-correlation peak in equations (1.10) and

(1.13) was always located at positive values of Δx. As a result, the values of the correlation function $C_{2D}(\Delta x, \Delta y; \Delta t)$ for $\Delta x > 0$ involve a combination of an auto- and a cross-correlation, whereas the values of $C_{2D}(\Delta x, \Delta y; \Delta t)$ for $\Delta x < 0$ consist only of cross-correlation contributions. Using the symmetry argument presented in section 2.3, the auto-correlation part of $C_{2D}(\Delta x, \Delta y; \Delta t)$ can then be obtained by calculating:

$$C_{2D}^{auto}(\Delta x, \Delta y; \Delta t) = C_{2D}(\Delta x, \Delta y; \Delta t) - C_{2D}(-\Delta x, -\Delta y; \Delta t) \quad \text{for } \Delta x \geq 0 \tag{1.15}$$

In order to evaluate the diffusion coefficients we focused our quantitative analysis on the displacements Δy in the velocity gradient (and Δz in the vorticity direction). Since we are not interested in the Δx-displacements, we used a very small number of bins in Δx, $N_{\Delta x} = 2$, i.e. one for negative and one for positive Δx-values. Then, after performing the subtraction of equation (1.15), we integrated $C_{2D}^{auto}(\Delta x, \Delta y; \Delta t)$ over Δx to obtain (see equation (1.10)):

$$C_{1D}^{auto}(\Delta y; \Delta t) = A \cdot \exp\left(-\frac{(\Delta y)^2}{2\sigma_y^2}\right) \tag{1.16}$$

with

$$A = K_1\, \hat{n}^2\, w(\Delta t)\, \chi(\Delta t; dof)\, \frac{\sqrt{\pi}\,\sigma_x}{\sqrt{2}\,\gamma \Delta t} \cdot \int_{-W}^{W} (W - |\Delta x|) \cdot \left(\operatorname{erf}\left[\frac{\Xi_1(\Delta x, \Delta y; \Delta t)}{\sqrt{2}\,\sigma_x}\right] - \operatorname{erf}\left[\frac{\Xi_2(\Delta x, \Delta y; \Delta t)}{\sqrt{2}\,\sigma_x}\right]\right) d\Delta x$$

But, since $|\Delta y|$, being of order of the particle radius a, is at least an order of magnitude smaller that H, y_0 and W, all of which are $O(1$ mm), the

amplitude A becomes independent of $|\Delta y|$ with an error of $O(a/H)$. Consequently, the width of the peak of C_{1D}^{auto} determines σ_y^2 which, in view of equation (1.9), equals twice the product of D_{yy} with the time-interval Δt, so that the diffusion coefficient can be determined by fitting the experimental data with equation (1.16).

We followed a similar procedures for analyzing the function $C_{2D}(\Delta x, \Delta z; \Delta t)$ and calculating the diffusivity D_{zz} in the vorticity direction. Again, after subtracting the cross-correlation part, we integrated $C_{2D}^{auto}(\Delta x, \Delta z; \Delta t)$ over Δx to obtain (see equation (1.13)):

$$C_{1D}^{auto}(\Delta z; \Delta t) = B \cdot (H - |\Delta z|) \cdot \exp\left(-\frac{(\Delta z)^2}{2\sigma_z^2}\right) \qquad (1.17)$$

with

$$B = K_2\, \hat{n}^2\, \psi(\Delta t) \int_{-W}^{W} \xi(\Delta x, \Delta t; dof)\, (W - |\Delta x|)\, d\Delta x$$

As $H \gg |\Delta z|$, the square of the width σ_z of this peak equals twice the product of the diffusion coefficient D_{zz} and the time interval Δt (see also equation (1.9)). Hence the diffusion coefficient D_{zz} can be determined by fitting the experimental data with equation (1.17).

In summary then, the diffusion coefficients D_{yy} and D_{zz} can be calculated by reducing the two-dimensional correlation functions $C_{2D}(\Delta x, \Delta y; \Delta t)$ and $C_{2D}(\Delta x, \Delta z; \Delta t)$ to the functions $C_{1D}(\Delta y; \Delta t)$ and $C_{1D}(\Delta z; \Delta t)$, respectively, and by subsequently fitting the resulting curves with the Gaussian peaks of equation (1.16) and (1.17). The amplitudes A and B of the respec-

tive equations (1.16) and (1.17) peaks were not analyzed thoroughly, because they contain a number of unknown functions.

4. Results and discussion

4.1. Validation of the technique

Using the experimental set-up, images were obtained of sufficiently high quality to carry out the required accurate image analysis procedures. A typical example of our image quality is shown in figure 1.7, which depicts a sample of two consecutive images (Δt = 220 msec) in a suspension with particle concentration $\phi = 0.30$ being sheared at the rate $\gamma = 1.79\ s^{-1}$.

In order to ensure that any observed self-diffusivity in a concentrated suspension was due only to the diffusive motion of the tracers, it was necessary to rule out the existence of any significant errors in our experimental set-up or in the image analysis procedure. The possible errors in the former included mechanical vibrations, rotation irregularities of the motor, non-uniformities in the Couette gap and misalignment of camera-optics. In addition, we expected some error in the calculation of the particle locations by the image analysis procedure. Although the importance of the image analysis error could not be estimated a priori, the errors originating from this source were minimized by applying homogeneous lighting and optimizing the contrast.

In order to quantify these errors, we performed measurements in a dilute suspension ($\phi = 0.4\%$) of only tracer particles, where the self-diffusivity was

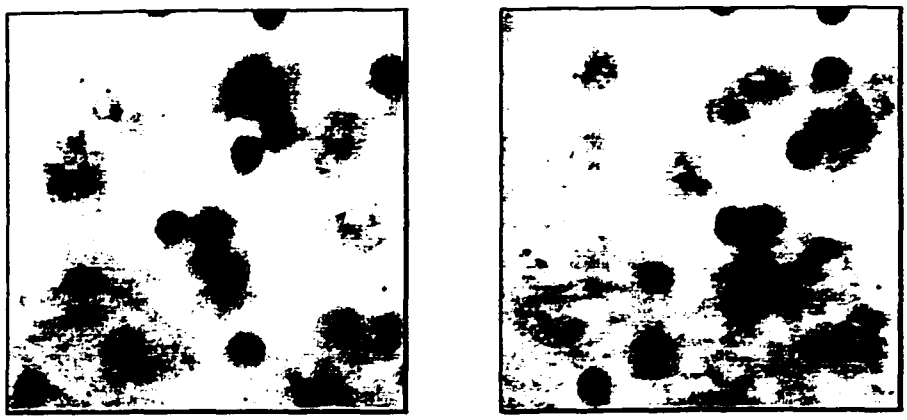

Figure 1.7: Photographs of two successive images taken 220 msec apart in a 30% concentrated suspension sheared at 1.79 s^{-1}. Here, the flow is from left to right.

expected to be negligible compared to the self-diffusivities reported in the literature for concentrated suspensions. Following the procedures described in section 3, the broadening of the correlation peaks in both the velocity gradient and vorticity direction was measured. This broadening is believed to be the result of the systematic errors mentioned above. If it was interpreted as self-diffusion, we found that the value of the associated diffusion coefficient was at most 10% of the values we observed for the concentrated suspensions at 30% volume fraction. The influence of the image analysis procedures on the diffusivity results was also checked and the results were found to be insensitive to changes in the criteria which we used for the detection of tracer particles in the images. These measurements in the dilute suspension showed that the contributions of the experimental errors were small. Hence, we applied the technique to determine the self- diffusivity in concentrated suspensions.

4.2. Particle self-diffusion in concentrated suspensions

The diffusion-coefficient experiments were conducted at solids concentrations ranging from 20 to 50% for values of $\gamma\Delta t$ ranging from 0.05 to 0.5. In figures 1.8 & 1.9 we present three-dimensional correlation plots for the case of $\phi = 0.30$ at $\gamma\Delta t = 0.085$ and 0.34, where $C_{2D}(\Delta x, \Delta z; \Delta t)$ is shown as a function on the Δx-Δz-plane according to the analysis procedures described in section 3.2. The Δx- and Δz-axis respectively represent the correlation distances in the velocity and vorticity gradient direction. The units of the

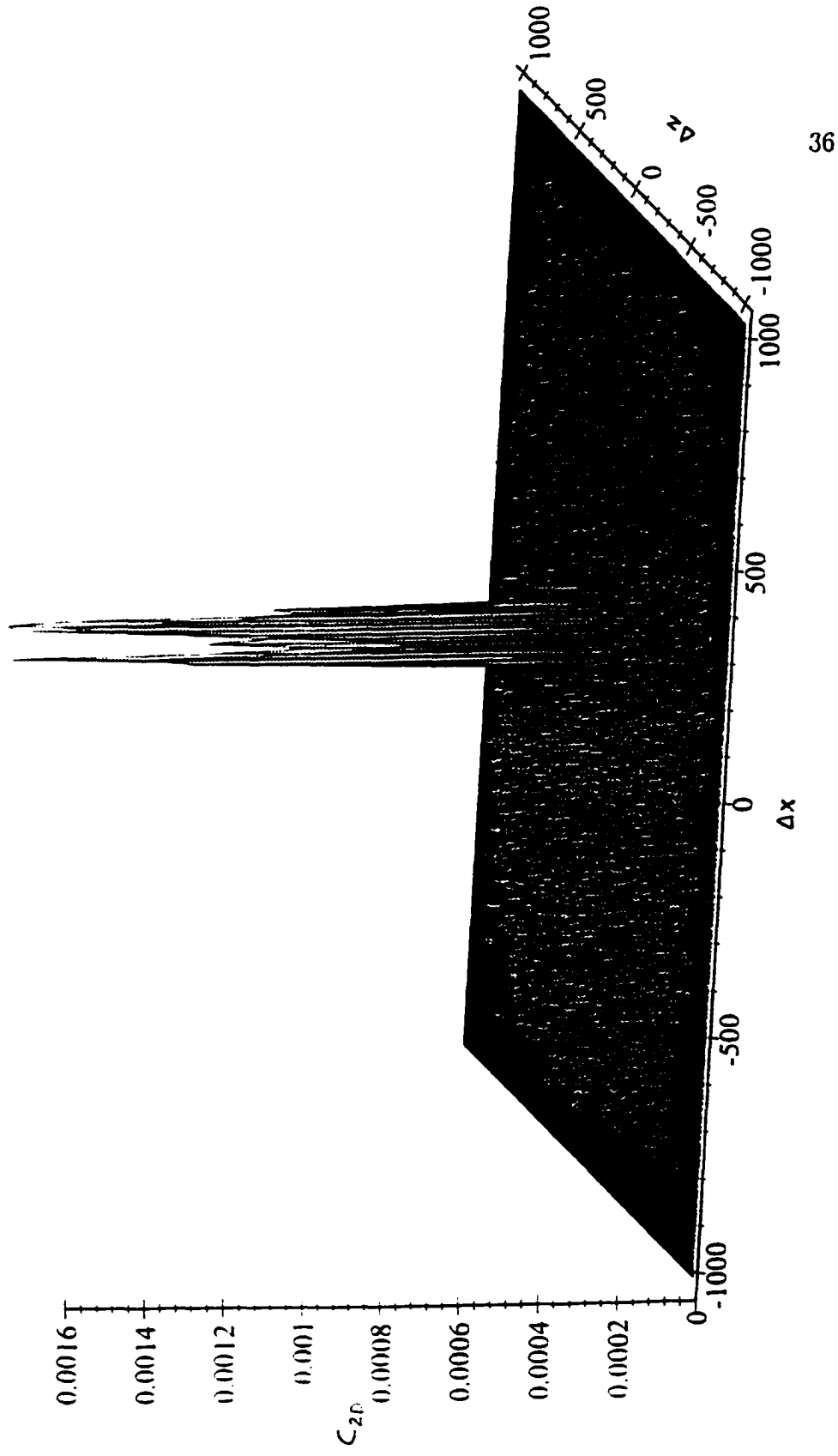

Figure 1.8: Plots of the experimentally determined correlation function C_{2D} in the Δx-Δz-plane for $\phi = 0.30$ and $\gamma\dot{}\Delta t = 0.085$.

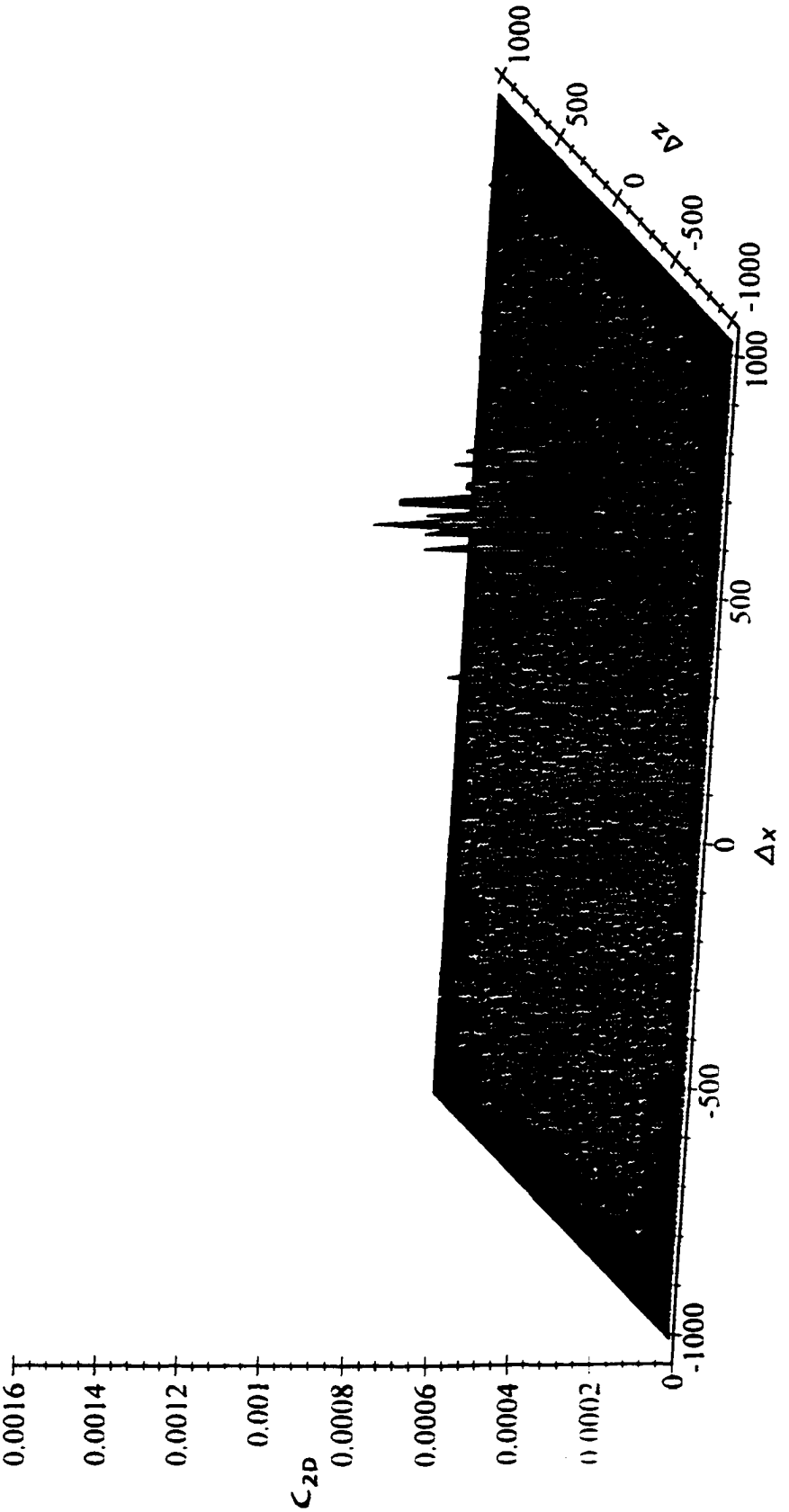

Figure 1.9: Plots of the experimentally determined correlation function C_{2D} in the Δx-Δz-plane for $o = 0.30$ and $\sim \Delta t = 0.34$.

displacements in the figures are pixels, for direct reference to the images. The auto-correlation peak is clearly distinguishable and is dominant over the cross-correlation contribution, which appears as the scatter in the rest of the plane. The width in the Δx-direction is the result of variations in the convective velocity over the window (see figure 1.3); in the Δz-direction the width is governed by the diffusive process and is much smaller. As the time-step Δt increases –from fig. 1.8 to 1.9–, the convective displacements increase and the peak shifts to the right. Also, the amplitude of the peak decreases, as fewer particles are detected in two consecutive images. These observations are in qualitative agreement with our expectations and figures 1.8 & 1.9 further validated our choice of the number of images acquired per run and the time interval Δt between consecutive images.

For a quantitative analysis, the three-dimensional plots were reduced to plots of $C_{1D}(\Delta z; \Delta t)$ as discussed in section 3.3. Figure 1.10 shows the graphs of $C_{1D}(\Delta z; \Delta t)$ versus Δz for the same experimental data as presented in figures 1.8 & 1.9, after subtraction of the cross- correlation part. Again, the displacements are expressed in pixels, but this could easily be transformed into SI-units by using the known camera magnification (1 pixel = 1.16 μm). The graphs also show the best possible fit with a Gaussian peak. It must be noted, that although the width of the peak is small compared to the particle size, a clear broadening can be observed in going from figure 1.10a to 1.10b, where Δt is increased.

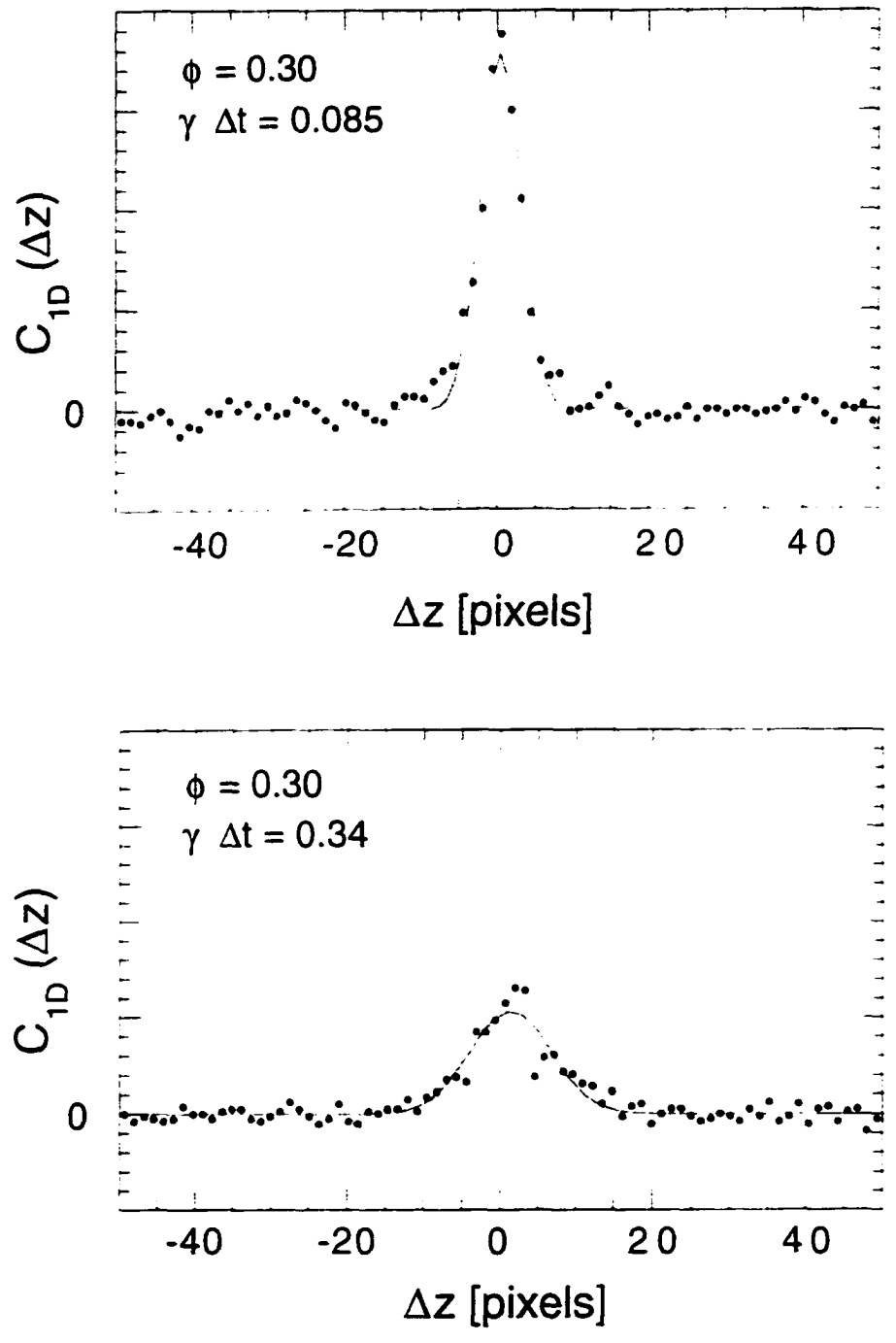

Figure 1.10: Plots of the experimentally determined correlation function C_{1D} vs. the displacement Δz for $\phi = 0.30$ and $\gamma\,\Delta t = 0.085$ (a) & 0.34 (b).

The decrease in the peak height with increasing values of $\gamma \Delta t$ also limits the range over which experiments could be performed, because the auto-correlation peak has to be distinguishable from the cross-correlation contribution. In our experimental set-up, measurements could be carried out for $\gamma \Delta t$ ranging from 0.05 to 0.5. For larger $\gamma \Delta t$ the particles did not remain within the window long enough to be detected in two consecutive images and thus contribute to the peak. This limitation was mainly caused by the fact that the experiments had to be performed in a region far enough from the wall of the outer cylinder to reduce wall effects as far as possible. The result is of a trade-off between the need of staying away from the wall and maximizing the range of $\gamma \Delta t$.

The width of the peaks in figure 1.10 is equal to the parameter σ_z defined in equation (1.9): $\sigma_z^2 = 2\, D_{zz}\, \Delta t$. For further analysis of the diffusion coefficient D_{zz} (and D_{yy}) and comparison with the results of other studies, the dimensionless scaling $\hat{D} = D/\gamma a^2$ must be introduced, where a is the particle radius. Using this formulation we therefore introduce the following two dimensionless diffusion coefficients:

$$\frac{\sigma_i^2}{a^2} = 2\, D_{ii}\, \gamma \Delta t \qquad i = y, z \tag{1.18}$$

For all experiments, the width of the peak has been determined and the results are presented in figures 1.11 to 1.13 where the dimensionless values σ_y^2/a^2 and σ_z^2/a^2 are plotted versus $\gamma \Delta t$ for the different volume fractions. These figures show that the linear scaling of equation (1.18) applies over

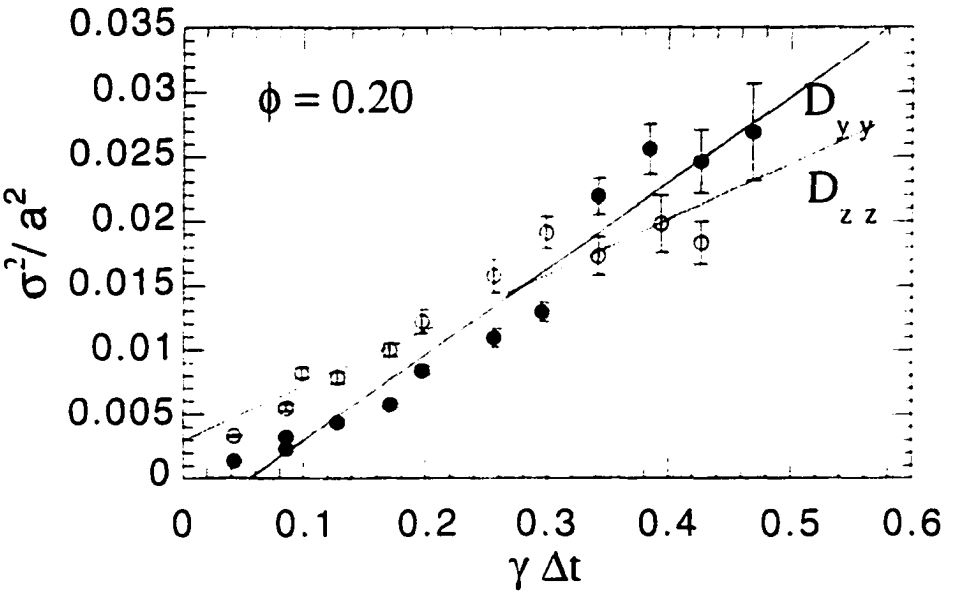

Figure 1.11: Plots of σ^2/a^2, the dimensionless variance of the correlation peak vs. $\gamma \Delta t$ for ϕ=0.20; the figure shows the results for both the velocity gradient (•- closed circles) and vorticity directions (o- open circles).

almost the entire range of $\gamma \Delta t$, i.e. from $\gamma \Delta t = 0.05$ to 0.5, although for $\phi = 0.20$ the linearity is not as clear as for the other experiments because the width of the auto-correlation peak is small and hence cannot be determined with much accuracy. The particle motion can, therefore, be described as a diffusive process on this time-scale and the diffusive character seems to exist over the entire range. This is rather surprising, because it was generally believed thus far that diffusive behaviour could only be attained for experimental time-scales $\gamma \Delta t > 1$, i.e. when the time-scales are larger than the assumed collision time in a simple shear flow and a particle has experienced several interactions.

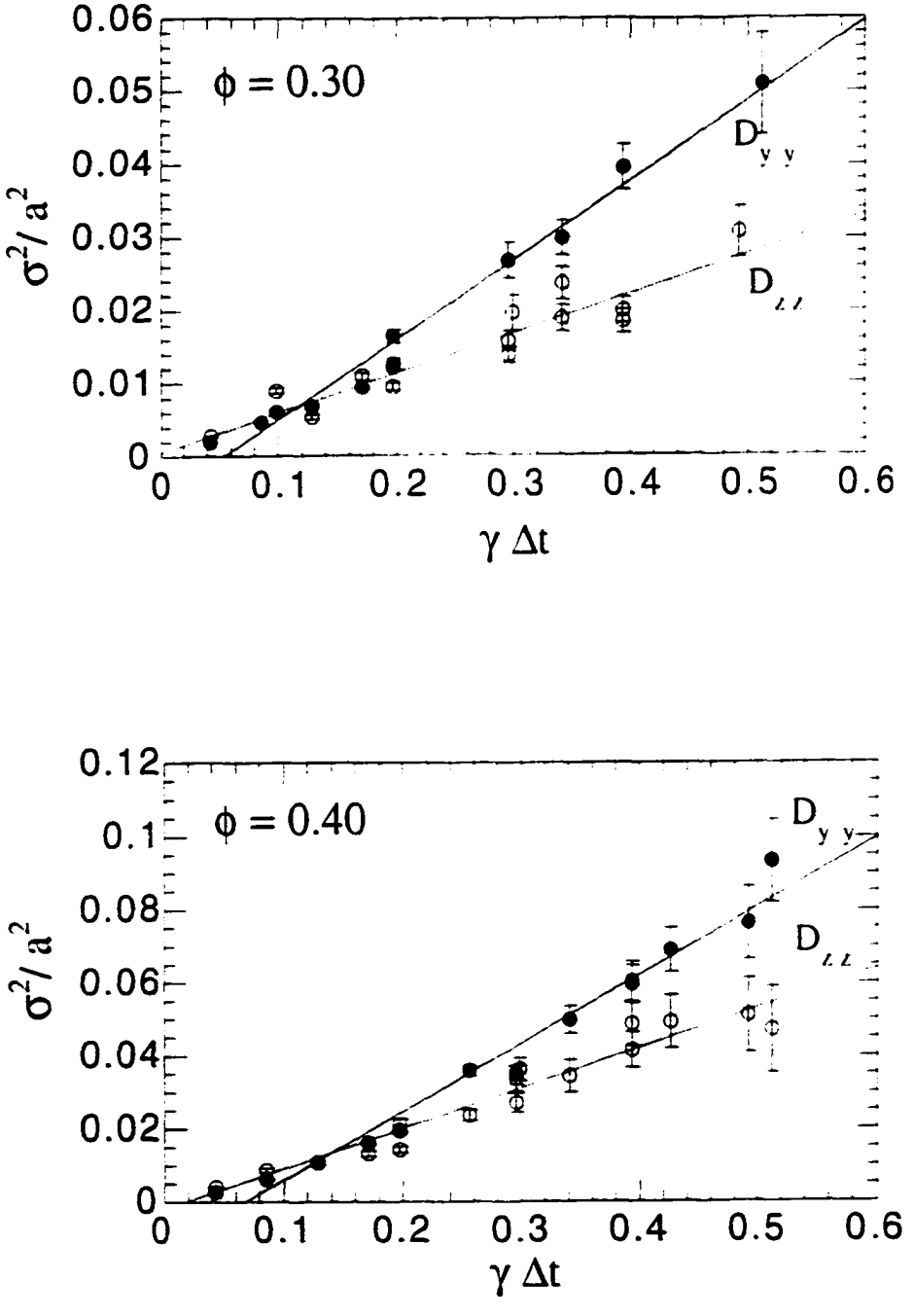

Figure 1.12: Plots of σ^2/a^2, the dimensionless variance of the correlation peak vs. $\gamma \Delta t$ for ϕ=0.30(a) and 0.40(b): the figures show the results for both the velocity gradient (•– closed circles) and vorticity directions (o open circles).

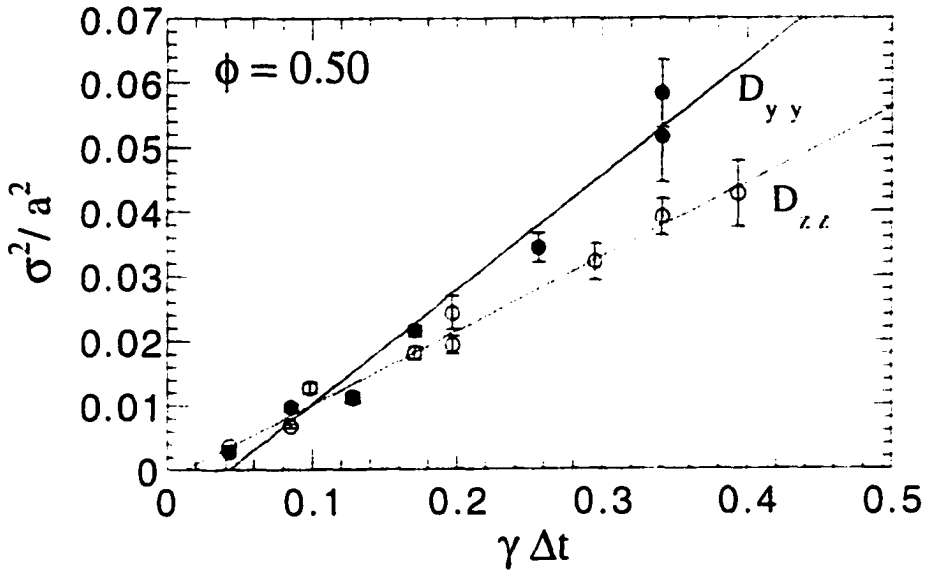

Figure 1.13: Plots of σ^2/a^2, the dimensionless variance of the correlation peak vs. $\gamma \Delta t$ for ϕ=0.50; the figure shows the results for both the velocity gradient (• closed circles) and vorticity directions (o- open circles).

Following equation (1.18), the dimensionless diffusion coefficients $\dot{D}_{yy}$ and $\dot{D}_{zz}$ can be calculated as one half the slope of the linear fits shown in figures 1.11 to 1.13. In all these figures, the diffusion coefficient in the velocity gradient direction ($\dot{D}_{yy}$) is considerably larger than in the vorticity direction ($\dot{D}_{yy}$) with the ratio being about 1.7 for all volume fractions.

Our results for the diffusion coefficients are plotted in figure 1.14 together with the results of the previous studies by Eckstein *et al.* (1977), Leighton & Acrivos (1987a) and Phan & Leighton (1993). Although these earlier experiments were performed for $\gamma \Delta t \gg 1$ by measuring the transit time and position of single tracer particles, they are in remarkable agreement with our

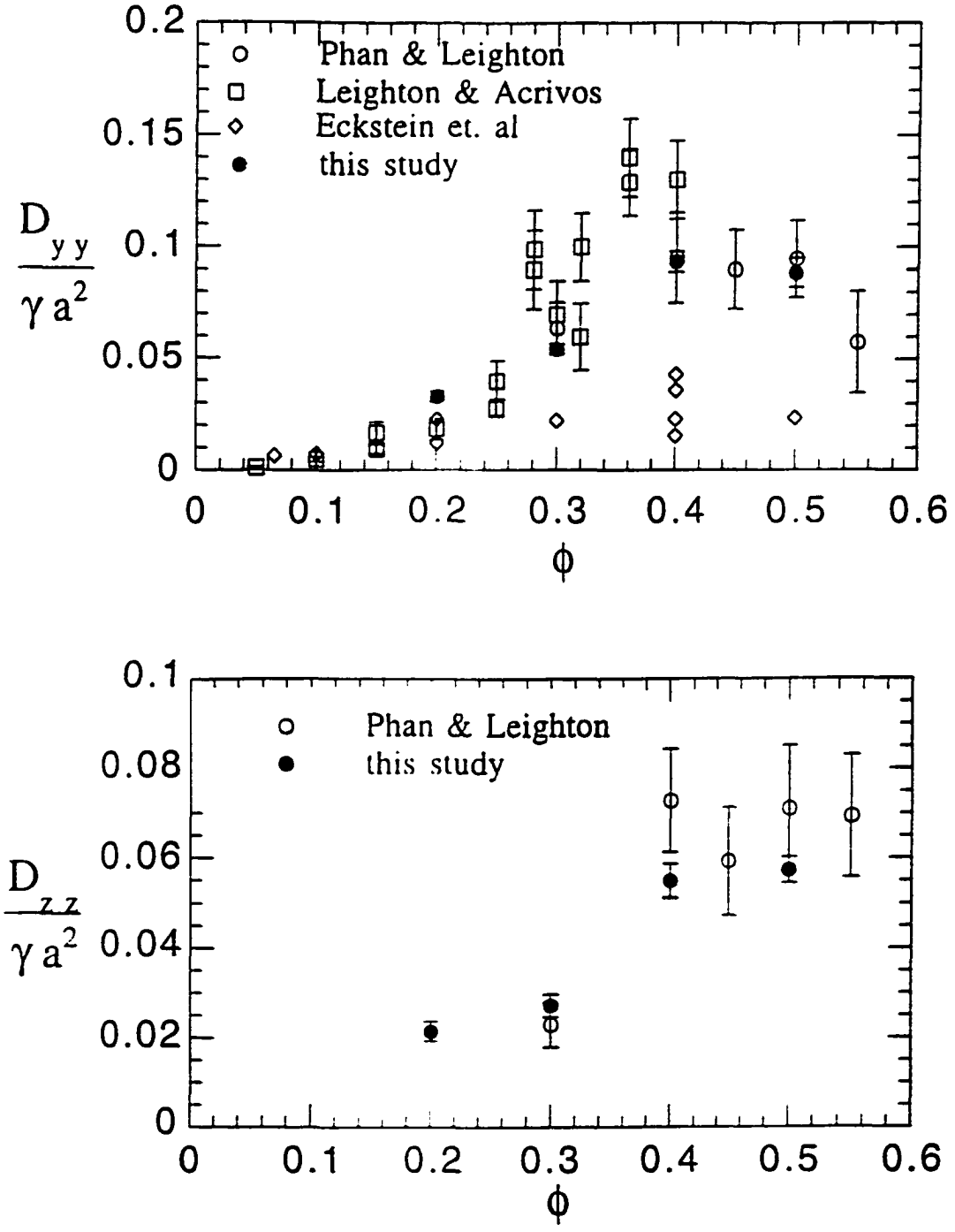

Figure 1.14: Comparison of the present results with previous experimental data for (a) the velocity gradient direction and (b) the vorticity direction. o–from Phan & Leighton (1993), □–from Leighton & Acrivos (1987), ◇–from Eckstein *et al.* (1977), •–from this study.

results for which $\gamma \Delta t < 1$. The error bars drawn for our data represent the uncertainty in the linear fits of figures 1.11 to 1.13; this error turned out to be dominant over the systematic errors, which were discussed in the previous section.

The self-diffusion coefficients $\hat{D}_{yy}$ and $\hat{D}_{zz}$ increase rapidly with increasing particle concentration, as was reported in all previous experimental studies, but their values appear to asymptote at $\phi = 50\%$. The same trend was also observed in the experiments by Phan & Leighton (1993).

4.3. Fluid tracer-diffusion in concentrated suspensions

The fluid-diffusion coefficients were estimated by examining the motion of tracers ($31.5\mu m$ in diameter) within a concentrated suspension of $325\mu m$ diameter particles having concentrations ranging from 30 to 50% and for values of $\gamma \Delta t$ ranging from 0.1-0.4. It is assumed that the motion of these tiny tracers represented the true fluid element motion in a suspension of large particles. In figures 1.15 & 1.16, we present the dimensionless variance of the correlation peak vs. $\gamma \Delta t$ for ϕ=0.30 and 0.40 in both the velocity gradient and vorticity directions and for ϕ=0.50 in the vorticity direction. Unfortunately, due to the presence of a curved interface in the case of ϕ = 0.5. measurements in the velocity gradient direction could not be performed. Following equation (1.18), the dimensionless fluid tracer diffusivities D^f_{yy} and D^f_{zz} are calculated as one half the slope of the linear fits shown in figures 1.15 to 1.16. Note that the diffusivities are scaled with γa^2. where a is the radius

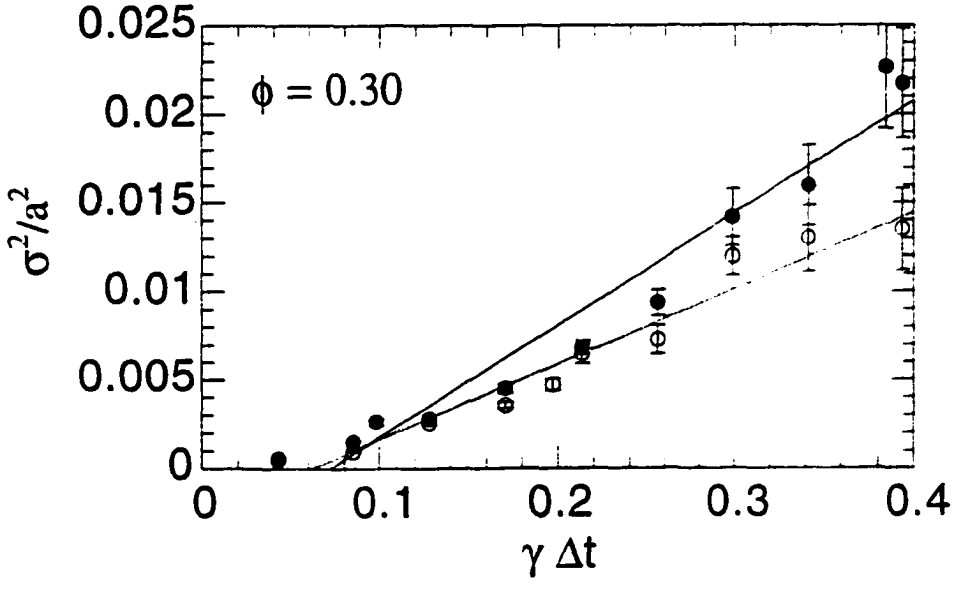

Figure 1.15: Plots of σ^2/a^2, the dimensionless variance of the correlation peak vs. $\gamma\,\Delta t$ for ϕ=0.30; the figure shows the results for both the velocity gradient (•– closed circles) and vorticity directions (o– open circles).

of particles making up the suspension. Our results for the fluid diffusion coefficients are plotted in figure 1.17a and 1.17b together with the results of the particle diffusivities reported earlier in figure 1.14. Clearly, the fluid tracer-diffusion coefficients are about 0.7 times the corresponding particle diffusion coefficients.

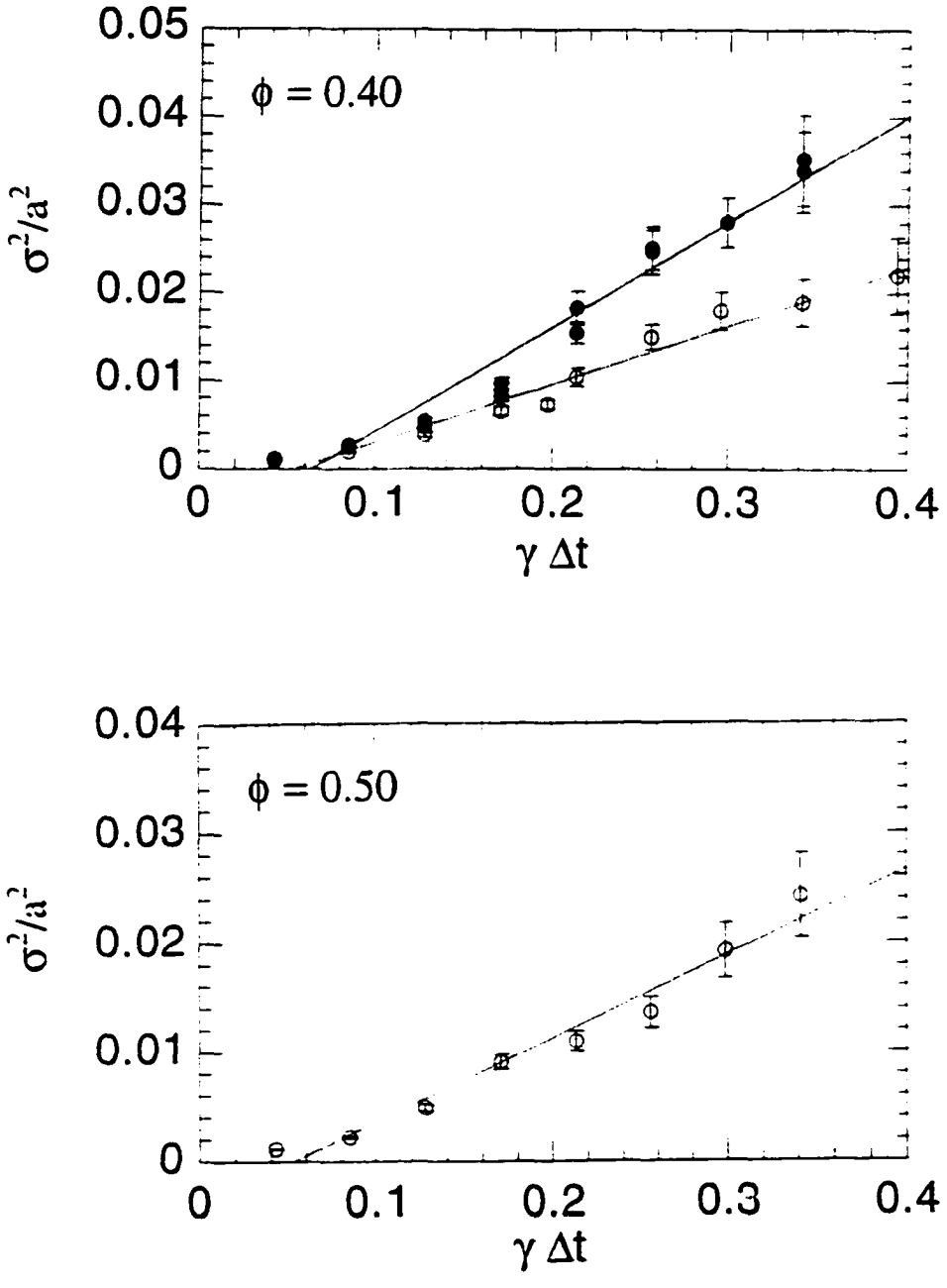

Figure 1.16: Plots of σ^2/a^2. the dimensionless variance of the correlation peak vs. $\gamma\,\Delta t$ for ϕ=0.40(a) and 0.50(b); the figures show the results for both the velocity gradient (•– closed circles) and vorticity directions (o– open circles).

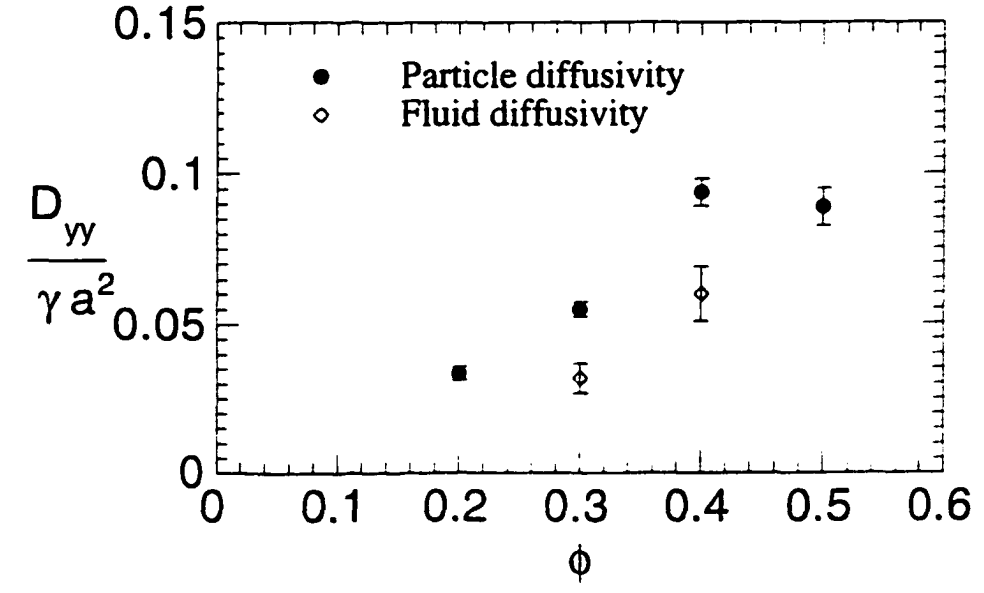

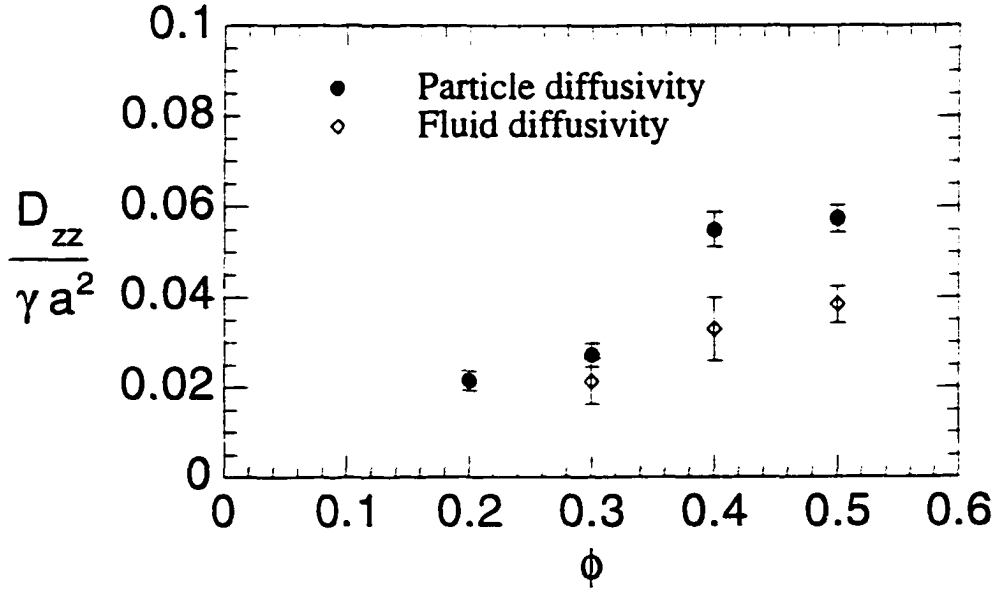

Figure 1.17: Comparison of the fluid and particle tracer-diffusivity experimental data for (a) the velocity gradient direction and (b) the vorticity direction. ◇–fluid tracer diffusivity, ●–particle self-diffusivity.

5. References

Bossis, G. & Brady, J. F. 1987 Self-diffusion of Brownian particles in concentrated suspensions under shear. *J. Chem. Phys.* **87**, 5437.

Brady, J. F. 1997 Shear-induced diffusion and particle migration. Presented at the AIChE Annual Meeting 1997, session 29D, Los Angeles.

Brady, J. F. & Morris, J. F. 1997 Microstructure of strongly sheared suspensions and its impact on rheology and diffusion. *J. Fluid Mech.* **348**, 103–139.

Eckstein, E. C., Bailey, D. G. & Shapiro, A. H. 1977 Self-diffusion of particles in shear flow of a suspension. *J. Fluid Mech.* **79**, 191.

Foss, D. 1997 *Private Communication* with Professor Brady.

Krishnan, G. P., Beimfohr. S. & Leighton, D. T. 1996 Shear-induced radial segregation in bidisperse suspensions. *J. Fluid Mech.* **321**, 371–393.

Leighton, D. T. & Acrivos, A. 1987 Measurement of shear-induced self-diffusion in concentrated suspensions of spheres. *J. Fluid Mech.* **177**, 109–131.

Leighton, D. T. & Acrivos, A. 1987 The shear-induced migration of particles in concentrated suspensions. *J. Fluid Mech.* **181**, 415–439.

Morris, J. F. & Brady, J. F. 1996 Self-diffusion in sheared suspensions. *J. Fluid Mech.* **312**, 223-252.

Phan, S. E. & Leighton, D. T. 1993 Measurement of the shear-induced tracer diffusivity in concentrated suspensions. *J. Fluid Mech.*, submitted.

Phung, T. 1993 Behavior of concentrated colloidal suspensions by Stokesian

Dynamics simulation. PhD thesis, Californian Institute of Technology.

Phung, T., Brady, J. F. & Bossis, G. 1996 Stokesian Dynamics simulation of Brownian suspensions. *J. Fluid Mech.* **313**, 181–207.

Van Kampen, N. G. 1992 Stochastic processes in physics and chemistry. Elsevier Science Publishers B.V., The Netherlands.

Yurkovetsky, Y. 1998 I. Statistical mechanics of bubbly liquids; II. Behavior of sheared suspensions of non-Brownian particles. PhD thesis, Californian Institute of Technology.

Zydney, A. L. & Colton, C. K. 1988 Augmented solute transport in the shear flow of a concentrated suspension. *PhysicoChemical Hydrodynamics* **10(1)**, 77-96.

Chapter 2

Viscous Resuspension in a Bidensity Suspension

abstract

Experiments were performed in a narrow gap Couette device to study the viscous resuspension process in a bidensity suspension consisting of two types of spherical particles, both having the same size, one of which was heavy while the other had the same density as that of the suspending fluid. The resuspension height of an initially settled bed of heavy particles was measured over a ten-fold range of applied shear rates, using an imaging technique which was developed to study the particle migration process in concentrated bidisperse suspensions. It was found that, at a given shear rate, the resuspension height of the heavy particles increased with an increase in the concentration of the neutrally buoyant spheres. The experimental results were then compared

with the predictions of a bidensity model based on the particle migration theory of previous work and good agreement was found between the two.

1. Introduction

Viscous resuspension is a process whereby, in the presence of shear, an initially settled layer of heavy particles becomes entrained in the bulk fluid even under conditions of vanishingly small Reynolds numbers. This phenomenon was studied both experimentally and theoretically by, among others, Gadala Maria(1979), Leighton & Acrivos(1986), Schaflinger et al.(1990), Chapman & Leighton (1991) and more recently by Acrivos et al.(1993). Acrivos et al.(1993) investigated this process in a narrow gap Couette device where the shear rate was (approximately) constant across the gap and, following Leighton and Acrivos (1986), modelled it by balancing the downward flux of particles due to gravity with an upward flux arising from shear-induced particle diffusion in a direction normal to the plane of shear from regions of high particle concentrations to low. According to this model, the change Δh in the height of the bed, relative to its (initial) settled value h_o, is a function of the single parameter $A = \frac{9}{2}\frac{\mu\gamma}{gh_o\Delta\rho}$, with γ being the shear rate and $g\Delta\rho$ the buoyancy force, which reflects the ratio of viscous to gravitational forces. Acrivos et al.(1993) found good agreement between the measured resuspension heights and those computed from the solution of their model equation.

In the present paper, we report the results of an experimental investigation of the resuspension process in a narrow gap Couette device where the suspension consisted of two types of spherical particles, both having same

size, one of which was heavy while the other had the same density as that of the fluid. Unlike the case treated in Acrivos et al.(1993), where a clear fluid layer existed above an initially settled bed, here that region was occupied initially by a suspension of neutrally buoyant particles of given volume fraction ϕ^*. The migration of particles and the resuspension height were observed using an imaging technique which was developed to study the shear-induced particle migration in concentrated bidisperse suspensions undergoing shear. It was found that, at the same shear rate, the resuspension height of the heavy particles was enhanced when ϕ^*, the initial concentration of the neutrally buoyant particles, was increased. This observed enhancement will be explained in terms of a bi-density model based on the particle migration theory of Leighton & Acrivos(1987). The experimentally determined resuspension heights were found to be in good agreement with those predicted theoretically.

In the next section we shall describe our experimental technique and results, and in section 3 we shall present a simple theoretical model for shear-induced migration in a bidensity suspension (particles having same size but of different density) to explain the enhanced resuspension phenomenon observed in our experiments. The final section is devoted to conclusions.

2. Experimental Technique and Results

2.1. Apparatus and materials

The experiments were performed in a narrow gap cylindrical Couette device, shown in figure 2.1, which consisted of two cylinders made of high quality plexiglass. The inner radius of the outer stationary cylinder(R_o) was 8.224cm and the outer radius of the inner rotating cylinder(R_i) was 7.542 cm, giving a gap size equal to 0.682cm. The inner cylinder was mounted on a shaft which in turn was mounted on a motor (ID Corp., California). The bottom of the apparatus was sealed with mercury. This prevented the particles from migrating out of the gap and also created a stress-free boundary. Since the gap-to-inner radius ratio was small, the shear was taken as being constant across the gap.

The particles used in the experiments consisted of acrylic and polystyrene spheres. The former were a lot of class B728 obtained from Zenica Resins, while the latter, obtained from Maxiblast Inc., were a lot of class PB-2.5. The density of the acrylic spheres was measured to be 1.165g/cc and those spheres containing air bubbles were segregated. Similarly, the polystyrene spheres of density 1.045gm/cc were segregated from those containing air bubbles. The polydisperse material was sieved to obtain a uniform fraction in the size range $300 - 350\mu m$, with a standard deviation of $25\mu m$. The acrylic spheres were dyed with black RIT liquid fabric dye and the color coating on the particles was found to be insoluble in the suspending fluid. The latter consisted of a

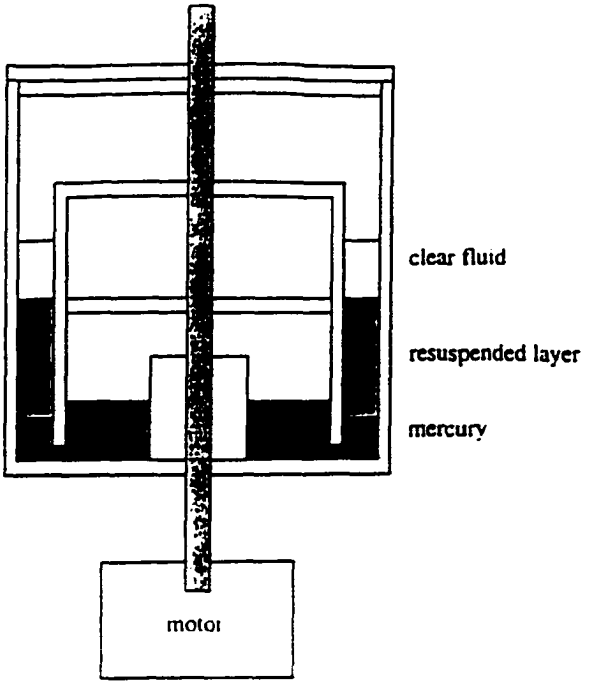

Figure 2.1: Schematic of the resuspension in a Couette gap and the experimental setup.

mixture of 40.9% (by volume) Dow Corning 556 and 59.1% Dow Corning 705 fluid which matched the density of the polystyrene particles. The refractive index of the suspending fluid was close to that of polystyrene particles though they were not matched exactly. The pure suspending fluid was Newtonian and had a viscosity of 57.2 cp at the operating temperature of 24°C.

2.2. Experimental Procedure

After sealing the gap with mercury, a sufficient amount(57ml) of suspending fluid was loaded to a height of 2 cm over the mercury in the Couette gap. The heavy (black) particles were subsequently introduced and the suspension was allowed to rest for three days. The settled height h_0 of the suspension was

then measured to be 0.43cm and 0.49cm for two different sets of experimental runs. Hence, the height of the suspending fluid occupying the region above the settled layer was sufficiently large for the purpose of maintaining the clear fluid layer above the resuspended region at all applied shear rates. Next, the suspension was sheared at shear rates varying from 1.48/s to 15/s which were lower by at least a factor of 20 than the critical shear rate for the onset of Taylor instability in a narrow gap Couette flow with the fluids used in this study. The change in the equilibrium height of the resuspended layer was measured using the technique described in the next section and consecutive runs were taken after a sufficient time had elapsed in order to ensure that steady state had been reached. This procedure was then repeated after adding density matched polystyrene particles(white) to the liquid above the settled bed and the resulting suspension was sheared for a day to drive out any air bubbles and eliminate any local concentration inhomogeneities present initially as a result of the loading procedure. The experiments were performed for values of the density matched particle concentration ϕ^* equal to 10%, 20%, 30%, 40% and 45%.

2.3. Measurement Technique

The migration of the particles, the resuspended height and the particle concentration were observed by viewing the suspension through a plexiglass window using a high resolution(1000K x 1000K) CCD camera (Kodak MegaPlus ES1.0) with Infinity Optics (98X total magnification on the monitor) plus a

Dantec light sheeting probe that provided an excellent contrast in the video. A three-dimensional traversing system was employed to mount the camera. This allowed us to measure the resuspended height and the concentration at various locations by traversing the magnified image on the video. Images from the CCD camera were passed via an 8-bit digital video signal to a dedicated image acquisition and processing board (Oculus F/64 by Coreco Inc.), which operated on a personal computer equipped with a 200MHz Intel Pentium processor.

The concentration of the heavy (black) particles was measured by counting of the number of particles in a known volume element Δx x Δy x Δz, of the flowing suspension. The cross-sectional area, Δx x Δy, was calculated using the known magnification of the camera optics and the pixel size of the CCD chip and, in our experiments, was found to be 0.5mm X 0.51mm. The depth of field, Δz, was determined by viewing a 45° inclined plane through the camera with the preset optics as shown in figure 2.2. The inclined plane had four sets of target columns containing different line pairs per millimeter(lp/mm). The resolution appropriate for the given magnification was then chosen and the distance corresponding to the point at which the resolution disappeared was measured. This distance was read from either the computer monitor or the scale on the inclined plane. Note that there was a factor of $\sqrt{2}$ on the appropriate inclined scale to account for the viewing angle. Using this technique, we measured the depth of view and the range of grey level

counts at the camera resolution. In our experiments, the depth of field was found to be $425 \pm 25\mu m$. Next, the number heavy (black) particles in this volume element was found by using a particle counting procedure in the imaging software(Visilog 5.0). This procedure involves morphology, binarization, threshold, holefill and edge-detection operations. Moreover, the grey level range estimated in the depth of field measurements successfully eliminated the "out of plane" blurred particles during these software manipulations.

The accuracy of the particle counting scheme depends on the quality of the image and the degree of particle overlap. In concentrated suspensions, the high degree of particle overlap makes it difficult to use the counting procedures for concentration estimations. To be sure, the concentration could be measured, in principle, by coloring a known fraction of refractive-index matched particles and assuming that the concentration of the suspension at any location is proportional to the fraction of the colored particles at that location. In our experimental system, however, it is not possible to match the refractive-indices for bidensity suspensions which have materials with different refractive-indices. Therefore, the concentration profiles of the neutrally buoyant and black particles were not measured throughout the suspension. Instead, in order to ascertain the height of the resuspension, we measured the concentration of the heavy (black) particles only in those regions where it fell below 5-6%. The center of the measurement volume was located at a distance of one particle diameter inside the outer wall of the Couette device using the

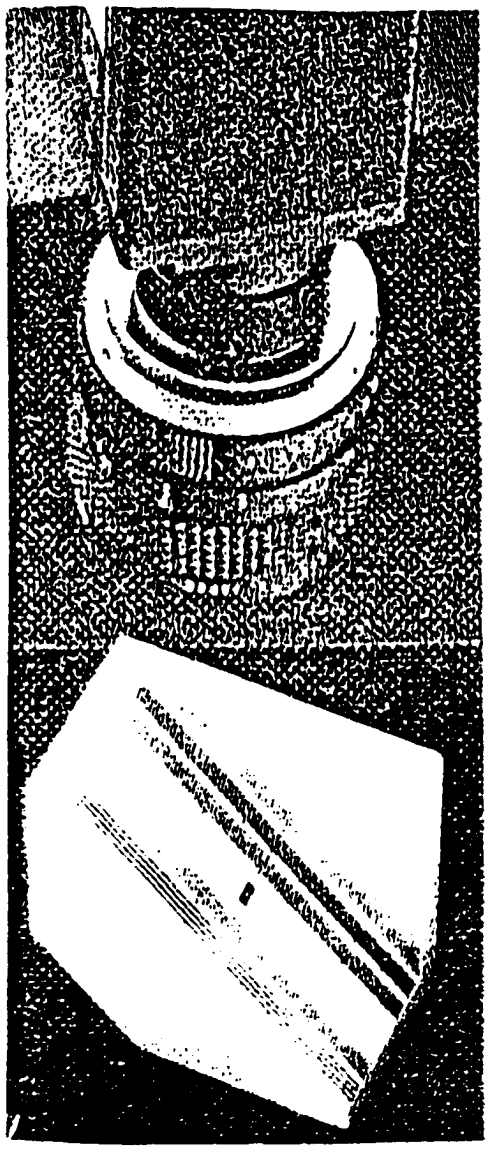

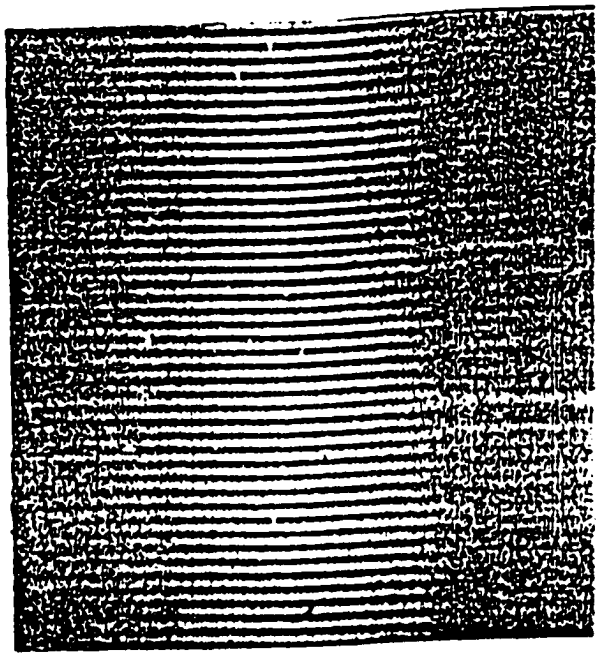

Depth of View

$$D.O.F\ (\Delta z) = \frac{\text{Depth of View}}{\text{Magnification}}$$

$$= 423 \text{ microns}$$

450 Inclined Plane
(with four resolutions)

Figure 2.2: Schematic diagram of the arrangement of the camera in depth of field measurement.

traversing system. At each location, around 200 images were digitized and processed for the concentration evolution. Subsequently, the concentration of the heavy (black) particles was obtained by ensemble averaging these images.

2.4. Experimental Observations and Results

Many interesting features were observed during our experiments investigating the shear-induced particle migration in a bidensity suspension. We first measured the resuspension height of the black particles in the absence of the neutrally buoyant particles (mono-density case) for shear rates varying from 1.4/s to 15/s. The results were then compared with the theoretical and experimental study of Acrivos et al.(1993) and were found to be in good agreement. The neutrally buoyant particles were then loaded at various concentrations following the procedure described in the previous section. We were then surprised to watch the heavy particles migrating (against gravity!) into the region occupied by the neutrally buoyant particles and also the neutrally buoyant particles migrating into the region of high concentration of the heavy particles. We observed that, as the initial concentration ϕ^* of the neutrally buoyant particles was increased, an increasing number of heavy(black) particles were entrained into the region containing the neutrally buoyant suspension. Shown in figures 2.3-2.5 are the photographs of different experimental runs. Further, unlike the case of the resuspension of heavy particles in clear fluid (the mono-density resuspension process) where a sharp interface was formed between the black particle resuspended layer

and the fluid above it, here the concentration of the black particles dropped to a negligible value over an extended region whose width increased with ϕ^*. Hence, it was impossible to locate the position where the concentration of the resuspended black particles was zero. We therefore chose to denote the resuspension height of the layer of black particles as that location where the measured concentration of the black particles was approximately 0.02.

This resuspension height was measured using the imaging technique described in the previous section. By making several measurements and then averaging, we found that, in general, this height could be located accurately with a standard deviation of 0.1mm whenever either the applied shear rate or the concentration of the neutrally buoyant particles was small. In these cases, the concentration of the black particles fell off rapidly to a negligibly small value. Thus, a clear contrast was created at the location where the black particle concentration became small. However, when the concentration of the neutrally buoyant particles was increased, we observed that the number density of the black particles decrease gradually, rather than abruptly, towards the top of the neutrally buoyant layer with the result that, owing to the small gradient in concentration, it was difficult to locate accurately the location at which the concentration of the black particles equalled 2%. We observed that, in these cases, the resuspended height(as defined above) could be located with an error bar shown in figure 2.6.

In the following section, we shall develop a simple theoretical model for

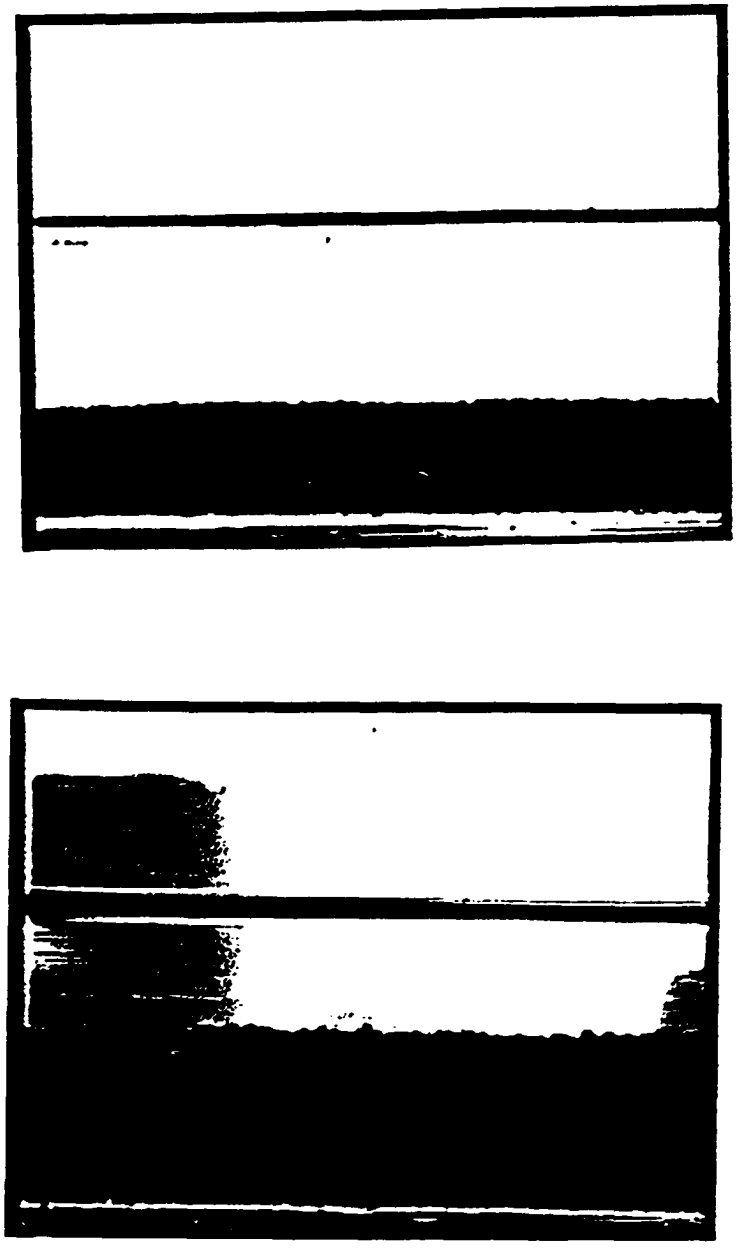

Figure 2.3: The photographs of experimental runs: A=0 & $\phi^* = 0$ (a) and A=0.5 & $\phi^* = 0$ (b).

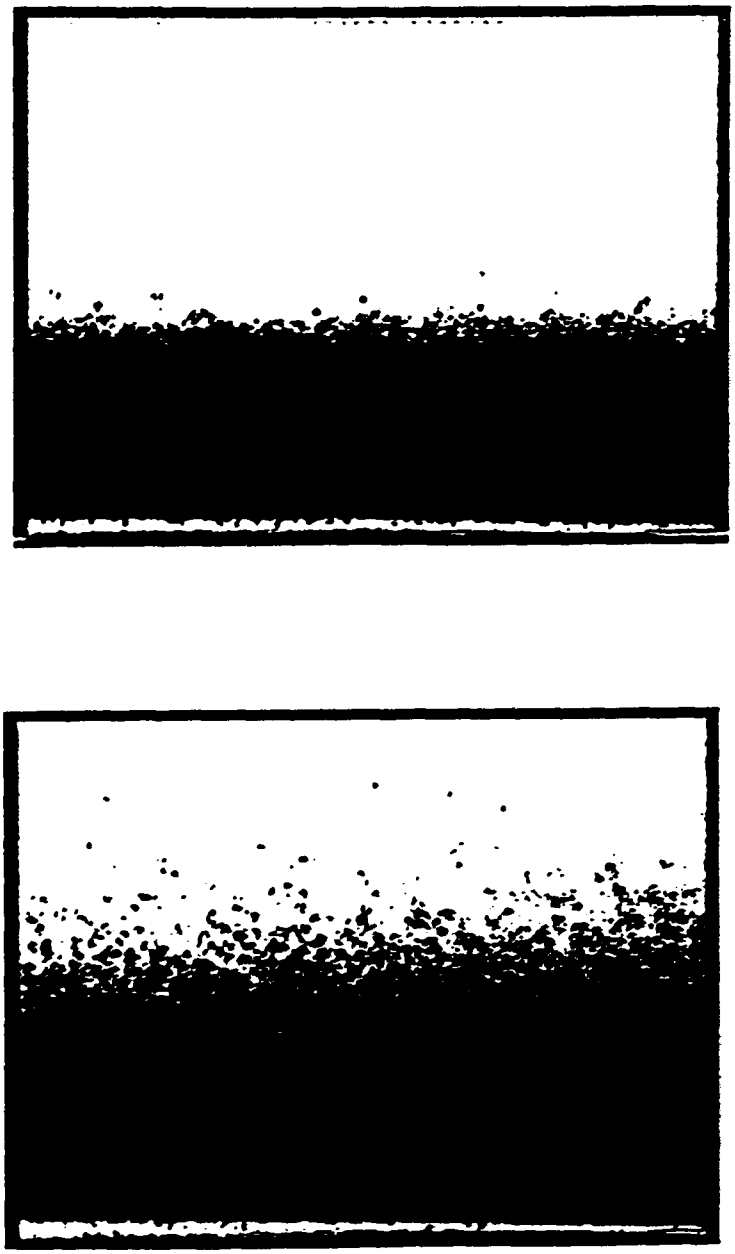

Figure 2.4: The photographs of experimental runs: A=0.5 & $\phi^* = 0.3$ (a) and A=0.5 & $\phi^* = 0.4$ (b).

Figure 2.5: A photograph of experimental run: A=0.5 & $\phi^* = 0.45$.

shear-induced migration in a bidensity suspension (particles having same size but different densities) to explain our experimental findings and to determine the concentration profile and resuspension height of the black particles.

3. Theory

3.1. Shear-induced resuspension in monodisperse suspensions

Consider an initially settled bed of heavy, non-Brownian monodisperse particles immersed in an infinite layer of a suspending fluid in a narrow gap Couette device. In the presence of an externally imposed shear flow, the settled layer is entrained into the bulk fluid and acquires a non-uniform particle concentration profile even under conditions of vanishingly small Reynolds

numbers. According to Leighton & Acrivos (1986), the particle concentration profile which is attained results from the combined effect of two particle fluxes (a) a gravitational flux given by,

$$\frac{2a^2 g\Delta\rho}{9\mu_f}\phi f(\phi), \tag{2.1}$$

where a is the particle radius, $f(\phi)$ is the hindrance function, μ_f is the viscosity of the pure suspending fluid and $g\Delta\rho$ is the buoyancy force, and (b) a shear-induced flux proportional to particle concentration gradient $\frac{d\phi}{dy}$. In turn, the latter consists of two terms: a convective flux ϕu, where u is the particle drift velocity in the absence of gravity due to the presence of a particle concentration gradient and ϕ is the particle concentration, and a diffusive flux equal to $-\gamma a^2 D_{tr}(\phi)\frac{d\phi}{dy}$, where $D_{tr}(\phi)$ is the particle *tracer* diffusivity. In addition, when the shear rate γ is constant across the gap, the drift velocity is given by

$$u = -\gamma a^2 \frac{D_g(\phi)}{\phi}\frac{d\phi}{dy}, \tag{2.2}$$

where $D_g(\phi)$, equal to the gradient diffusivity rendered dimensionless with γa^2, is a function of ϕ only. It should be noted that the shear-induced gradient diffusivity is quite different from the shear-induced coefficient of self- or tracer- diffusion. Shear-induced self diffusion, investigated experimentally by Leighton & Acrivos(1987) and Eckstein et al. (1977) and via numerical simulation by Bossis & Brady (1987), arises from the random motion of the

particles which occurs as they tumble over one another in a shear flow. Thus, self-diffusion governs the mixing of labeled particles in a sheared suspension at a uniform concentration. In contrast, the gradient diffusivity is defined as the ratio of the particle flux resulting from a concentration gradient to the magnitude of the gradient. Since the interaction of particles in a shear suspension may act to "push" particles from regions of high concentration to low, the gradient diffusivity is not necessarily the result of a random walk process.

We use the model proposed by Leighton & Acrivos(1986.1987) to obtain

$$D_g(\phi) = \frac{1}{3}\phi^2(1 + \frac{1}{2}e^{8.8\phi}) - D_{tr}(\phi) \tag{2.3}$$

$$D_{tr}(\phi) = \frac{1}{2}\phi^2(1 + 0.09e^{7\phi}). \tag{2.4}$$

We note parenthetically that alternate expressions for $D_g(\phi)$ and $D_{tr}(\phi)$ have been proposed by Phillips et al.(1992), but the results to be presented below are not significantly affected if one set is chosen over the other.

At steady state, the net particle flux in a sheared suspension vanishes, thus we obtain the flux balance equation:

$$A\{D_g(\phi) + D_{tr}(\phi)\}\frac{d\phi}{d\xi} = -\phi f(\phi) \tag{2.5}$$

where $\xi = y/h_o$ and A is defined as

$$A = \frac{9}{2}\frac{\mu_f \dot{\gamma}}{g\Delta\rho h_o}. \tag{2.6}$$

Here, h_o is the initial settled height of the heavy particles in the absence of shear. Therefore, the concentration distribution and the resuspended height of a sheared suspension is obtained by solving equation (2.5) subject to the conditions:

$$\begin{aligned} \int_0^h \phi d\xi &= \phi_{max} \\ \phi(\xi = h) &= 0 \end{aligned} \tag{2.7}$$

where h is the resuspension height divided by h_o and ϕ_{max} is the particle concentration in the settled suspension. Also, as in Leighton & Acrivos (1986), we approximate $f(\phi)$ by means of

$$f(\phi) = \frac{1-\phi}{\mu_r}. \tag{2.8}$$

where μ_r is the relative viscosity of the suspension given as

$$\mu_r = \frac{\mu(\phi)}{\mu_f} = [1 + \frac{1.5\phi}{1 - \frac{\phi}{\phi_{max}}}]^2. \tag{2.9}$$

with ϕ_{max} taken here as equal to 0.58. A plot of h-1 as function of A (as obtained from the numerical solution of the system given above) is shown in figure 2.6. Hence, provided that an infinite clear fluid layer exists above the settled layer, the resuspension height is predicted to increase monotonically with the strength of the applied shear rate. Previous studies (Leighton & Acrivos(1986) and Acrivos et al.(1993)) have shown a good agreement between the model predictions and the experiments.

In the following subsection, we shall develop a model for determining the concentration profile and resuspension height when an infinite clear fluid layer above an initially settled bed is replaced by a suspension of neutrally buoyant particles.

3.2. Shear-induced resuspension in a bidensity suspension

Consider an infinite layer of a suspension of neutrally buoyant spherical particles(white) of known concentration ϕ^* above an initially settled bed of heavy spherical particles(black colored) in a narrow gap Couette device. The black spheres (density ρ_1) and the white spheres(density $\rho_2 = \rho_f$) have the same size(radius a). In the presence of an applied shear, the black particles will again resuspend into the white suspension but the diffusion and sedimentation fluxes experienced by these particles will now differ from those given in the previous section. Recently, Revay & Higdon (1992) have described the results of numerical simulations for the polydisperse sedimentation of equal-sized spheres, e.g. particles of different density in the absence of an imposed shear flow. Using Stokesian dynamics, these authors have shown that the settling velocities of individual particles species can be expressed in terms of two scalar functions of the total volume fraction ϕ, the self-mobility M_o and the interaction mobility M_1. By rearranging equation (14) of Revoy and Higdon, we therefore obtain the sedimentation flux, N_{g_i} of the two species as

$$N_{g_i} = \frac{2}{9}\frac{a^2 g \Delta\rho}{\mu_f}\phi_i\{\tilde{M}_o(\phi)\delta_{i1} + \frac{\tilde{M}_1(\phi)}{\phi}\phi_1\} \tag{2.10}$$

where $\phi_i (i = 1, 2)$ is the concentration of species i and $6\pi\mu_f a M_o \equiv \tilde{M}_o(\phi)$ (similarly for $\tilde{M}_1(\phi)$, c.f. fig. 1 & 2, Revoy & Higdon). These two scalar functions can be represented as

$$\tilde{M}_o(\phi) \sim 1 - \frac{\phi}{\phi_{max}} \tag{2.11}$$

$$\tilde{M}_o(\phi) + \tilde{M}_1(\phi) \sim f(\phi), \tag{2.12}$$

where $f(\phi)$ is given by equation (2.8).

As mentioned in §3.1, two additional fluxes arise in a sheared suspension due to the particle drift velocity and the self or tracer diffusivity. According to the model of Leighton & Acrivos, the presence of gradients in concentration lead to gradients in viscosity which, in turn, cause particles undergoing measurable interactions to be displaced from regions of high viscosity to low, and hence from regions of high concentration to low. Therefore, in bidensity suspensions of two sets of particles having the same size, the particle drift velocity is proportional to the gradient of the total particle concentration, i.e. $\frac{d\phi}{d\xi}$. Consequently, the convective flux, of particles of species i, becomes

$$\frac{\gamma a^2}{h_o}\phi_i\frac{D_g(\phi)}{\phi}\frac{d\phi}{d\xi}, \tag{2.13}$$

where $D_g(\phi)$ is given by equation (2.3).

The second source of particle migration in a bidensity suspension arises from the random self-diffusion process. In order to explain this, let us consider a case where a suspension of neutrally buoyant spheres of the same size is loaded in a Couette gap. Let us further imagine that the particles in the bottom half of the suspension are colored black while the particles in the top half are white. When the suspension is subjected to shear, the black particles interact with the other(black & white) particles in the suspension and suffer random displacement normal to their undisturbed streamlines. As a result of this, some of the black particles will spend part of their time in the white layer and a part in the black layer. Note that here the drift mechanism is absent, owing to the absence of actual gradients in the total concentration of particles. In contrast, the random walk motion leading to the tracer diffusivity requires particles to exchange positions and the tracer diffusivity here is proportional to the total concentration of the black and white particles. The shear-induced diffusive flux, of particles of species i, is then given by

$$\frac{\gamma a^2}{h_o} D_{tr}(\phi) \frac{d\phi_i}{d\xi}, \tag{2.14}$$

where $D_{tr}(\phi)$ is given by equation (2.3) since the two sets of particles have the same size. Hence, the shear-induced flux, J_{D_i} of particles of species i is given by

$$J_{D_i} = -\frac{\gamma a^2}{h_o}\{\phi_i \frac{D_g(\phi)}{\phi}\frac{d\phi}{d\xi} + D_{tr}(\phi)\frac{d\phi_i}{d\xi}\}. \tag{2.15}$$

Equation (2.15) is similar in form to an expression for the flux of each species proposed by Shauly et al. (1997) who also proposed a set of model equations for the more general case of polydisperse suspensions containing particles of different sizes.

At steady state, the net flux of the particles of each species in a sheared suspension vanishes, thus the flux balance becomes

$$A\{\phi_i \frac{D_g(\phi)}{\phi}\frac{d\phi}{d\xi} + D_{tr}(\phi)\frac{d\phi_i}{d\xi}\} = -\phi_i\{\tilde{M}_o(\phi)\delta_{i1} + \frac{\tilde{M}_1(\phi)}{\phi}\phi_1\} \qquad (2.16a,b)$$

It is important to note that, within the infinite suspension layer of white particles the tracer diffusivity of the black particles is now finite rather than being zero as within the clear fluid layer in the monodisperse case. This makes it possible for the black particles to migrate into the infinite layer of neutrally buoyant particles. In addition, the settling velocity of the black particles is now decreased owing to the presence of the white particles, and, therefore the magnitude of the hindrance function f is reduced. Similarly, the white particles migrate inside the black resuspended layer. Hence, we need to solve equation (2.16) subject to the conditions

$$\int_0^\infty \phi_1 d\xi = \phi_{max} \qquad (2.17)$$

which expresses the conservation of the total volume of black particles, and

$$\phi_1 \to 0 \quad as \quad \xi \to \infty$$

$$\phi_2 \to \phi^* \quad as \quad \xi \to \infty. \qquad (2.18)$$

Next, we add the two differential equations given by equation (2.16) to obtain

$$\frac{d\phi}{d\xi} = -\frac{\{\tilde{M}_0(\phi) + \tilde{M}_1(\phi)\}\phi_1}{A\{D_g(\phi) + D_{tr}(\phi)\}} \tag{2.19}$$

which, when integrated using equations (2.17)-(2.18) yields:

$$\int_{\phi^*}^{\phi(0)} \frac{\{D_g(\phi) + D_{tr}(\phi)\}}{\{\tilde{M}_0(\phi) + \tilde{M}_1(\phi)\}} d\phi = \frac{\phi_{max}}{A}, \tag{2.20}$$

where $\phi(0)$, determined by the above expression, is the total concentration at $\xi = 0$. We then multiply equation (2.16a) by ϕ_2 and equation (2.16b) by ϕ_1 and subtract to obtain

$$\frac{dX}{d\xi} = -\frac{X(1-X)\tilde{M}_0(\phi)}{AD_{tr}(\phi)}, \tag{2.21}$$

where $X = \frac{\phi_1}{\phi}$. On making use of equations (2.17)-(2.19) and integrating equation (2.21), we then arrive at

$$X(0) = 1 - exp[-\int_{\phi^*}^{\phi(0)} \frac{\tilde{M}_o(\phi)\{D_g(\phi) + D_{tr}(\phi)\}}{\phi D_{tr}(\phi)\{\tilde{M}_0(\phi) + \tilde{M}_1(\phi)\}} d\phi], \tag{2.22}$$

where $X(0)$, determined by the above, is the fraction of the heavy particles at $\xi = 0$. We then solve equations (2.19) & (2.21) using the Runge-Kutta fourth order method by marching from $\xi = 0$.

Although, in principle, the concentration of the black particles in the bidensity suspension vanishes only at infinity, we chose, as remarked earlier, to estimate the resuspension height as that value of ξ where the concentration

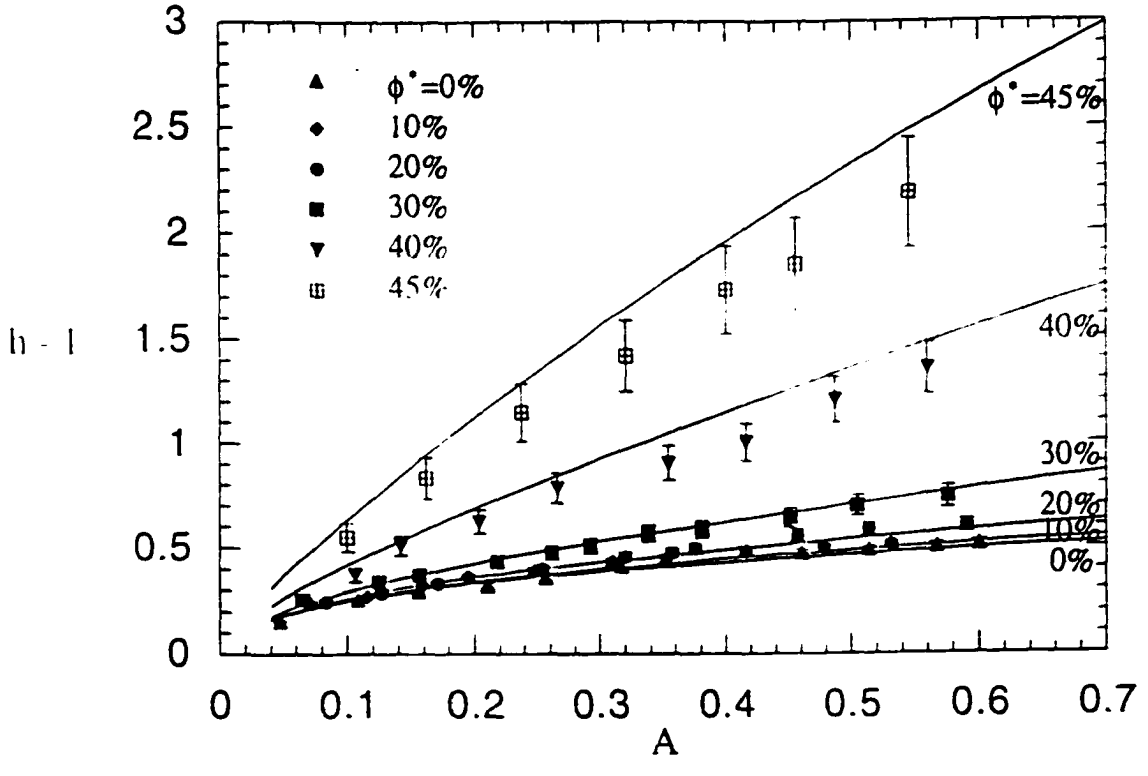

Figure 2.6: A comparison between the experimental data for h as a function of A and the theoretical model predictions.

of black particles ϕ_1 equals 2%. Note that this definition of the resuspension height is consistent with that of our experimental work. Shown in figure 2.6 is the comparison between the experimental data for h as a function of A and the results of the theoretical model as obtained from the numerical evaluation of equations (2.5)-(2.7) and equations (2.18)-(2.22). The two sets appear to be in good agreement. Figures 2.7-2.8 are the theoretical concentration profiles for different values of A and ϕ^*. It is interesting to note that the lighter white particles are also predicted to migrate, down to $\xi = 0$, for high values of A & ϕ^*. The concentration profiles, shown in figures 2.7-2.8, are in good agreement with those observed experimentally(shown in figures 2.3-2.5).

4. Conclusions

In this paper we have reported the results of a theoretical and experimental investigation of a viscous resuspension process in a bidensity suspension sheared in a narrow gap Couette device. This suspension consisted of two types of equi-sized spherical particles, of which one was heavy while the other had the same density as that of the suspending fluid. Over a ten-fold range of applied shear rates, the resuspension height of the initially settled bed of heavy particles was measured using an imaging technique. The resuspension height of the heavy particles was observed to increase with the concentration of the neutrally buoyant particles. The experimental results were found to

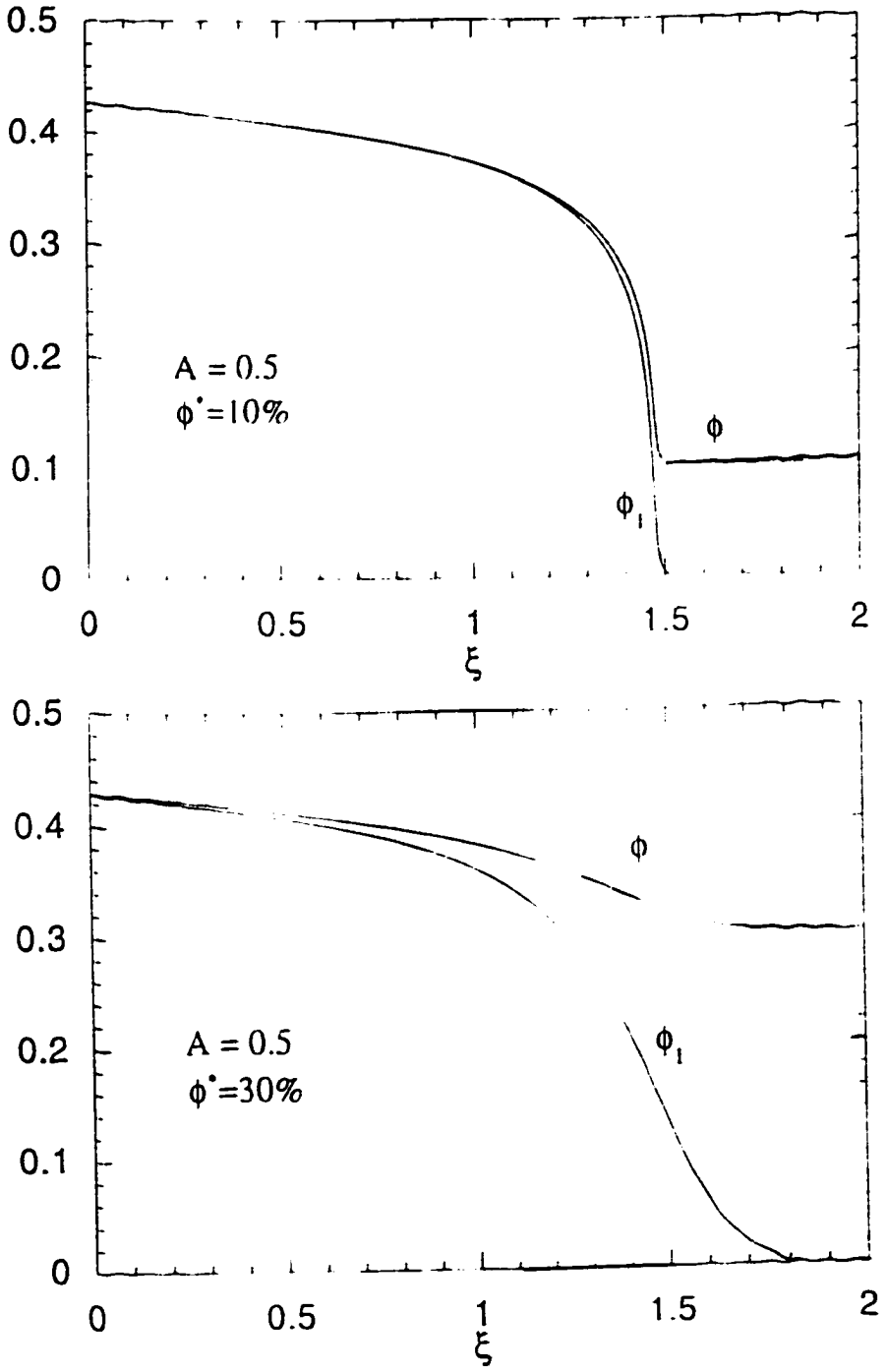

Figure 2.7: The theoretical concentration profiles for A=0.5 & $\phi^* = 0.1$ (a) and A=0.5 & $\phi^* = 0.3$ (b).

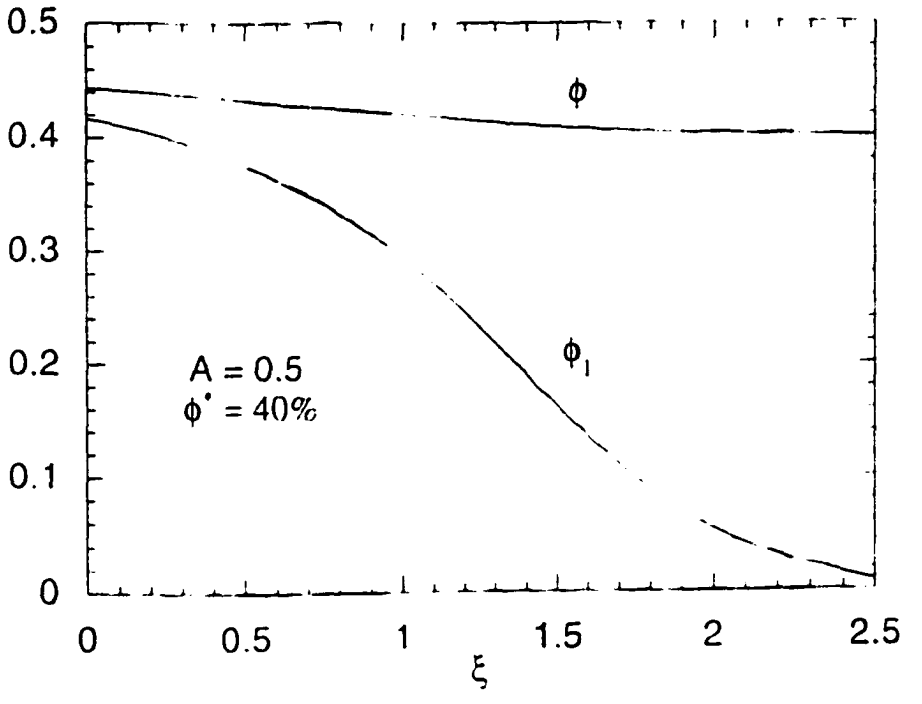

Figure 2.8: The theoretical concentration profile for A=0.5 & $\phi^* = 0.4$.

be in good agreement with the predictions of a bidensity model based on the Leighton & Acrivos migration theory. The success of the bidensity model has provided strong evidence to the effect that the observed enhancement of the resuspended height is due to the existence of a shear-induced particle tracer diffusivity and the decrease in the settling velocity of the heavy particles due to the presence of the neutrally buoyant particles in the region above the initially settled bed of heavy particles.

5. References

Acrivos, A., Mauri, R. & Fan, X. 1993 Shear-Induced resuspension in a Couette device. *Int. J. Multiphase Flow* **19**, 797-802.

Bossis, G. & Brady, J. F. 1987 Self-diffusion of Brownian particles in concentrated suspensions under shear. *J. Chem. Phys.* **87**, 5437-5448.

Chapman, B. K. & Leighton, D. T. 1991 Dynamic viscous resuspension. *Int. J. Multiphase Flow* **17(4)**, 469-483.

Eckstein, E. C., Bailey, D. G. & Shapiro, A. H. 1977 Self-diffusion of particles in shear flow of a suspension. *J. Fluid Mech.* **79**, 191-208.

Gadala-Maria, F. A. 1979 The rheology of concentrated suspensions. Ph.D. Thesis, Stanford University.

Leighton, D. T. & Acrivos, A. 1986 Viscous resuspension. *Chem. Eng. Sci.* **41**, 1377-1384.

Leighton, D. T. & Acrivos, A. 1987 Measurement of shear-induced self-diffusion in concentrated suspensions of spheres. *J. Fluid Mech.* **177**, 109-131.

Leighton, D. T. & Acrivos, A. 1987 The shear-induced migration of particles in concentrated suspensions. *J. Fluid Mech.* **181**, 415-439.

Phillips, R. J., Armstrong, R. C., Brown, R. A., Graham, A. L. & Abbot, J. R. 1992 A constitutive equation for concentrated suspensions that accounts for shear-induced particle migration. *Phys. Fluids A* **4**, 30-40.

Revoy, J. M. & Higdon, J. J. L. 1992 Numerical simulations of polydisperse

sedimentation: equal sized spheres. *J. Fluid Mech.* **243**, 15-32.

Schaflinger, U., Acrivos, A. & Zhang, K. 1990 Viscous resuspension of a sediment within a laminar and stratified flow. *Int. J. Multiphase Flow* **16**, 567-578.

Shauly, A., Wachs, A. & Nir, A. 1997 Shear-induced resuspension of poly-dispersed suspension. *To be submitted.*

Chapter 3

A New Criterion for the Continuous Operation of Supersettlers in the Bottom Feeding Mode

abstract

By considering the hydrodynamic interaction between the suspension and the concentrated sediment in an inclined settler operation continuously in the bottom feeding mode. a new upper bound is derived for the maximum value of the volumetric feed rate which can be tolerated under a given set of conditions. This criterion is distinct from the familiar Ponder-Nakamura-Kuroda formula which results from applying simple kinematic arguments. Experiments were performed in a continuously operated high aspect ratio settler to check the validity of the theoretical analysis. It was found that the

experimental results for β_{min} were in good agreement with the corresponding theoretical predictions for $0.50 \leq \phi_d \leq 0.55$.

1. Introduction

The thickening of slurries and the separation of solid particles from liquid streams by means of gravity settling constitute an important step in many industrial processes such as those in water treatment plants, chemical waste treatment plants, mining industry etc. These process are often slow and requires large vessels especially when the particles are small and fluid is viscous. One way of enhancing the settling process is by employing continuously operated settlers with inclined walls (often called *supersettlers*). These settlers greatly enhance the surface area for capturing the sedimenting particles with the result that the suspension is separated in a time much shorter than that required by their vertical counterparts.

Consider a typical supersettler, sketched in figure 3.1, being operated continuously in the bottom feeding mode. We suppose that the feed consists of a well mixed monodisperse suspension of heavy spherical particles. As the suspension flows inside the settler under conditions where the particle Reynolds number is vanishingly small, the particles slip in the direction of gravity relative to the liquid and then form a concentrated sediment upon reaching the upper-facing surface of the settler. As a result, the interior of the settler contains three distinct fluid phases: 1) a particle free layer underneath the downward facing surface; 2) the bulk of the suspension where the particle volume fraction ϕ_s equals that in the feed; and 3) the sediment layer referred to above. It follows that, if the settler is long enough, all the particles will

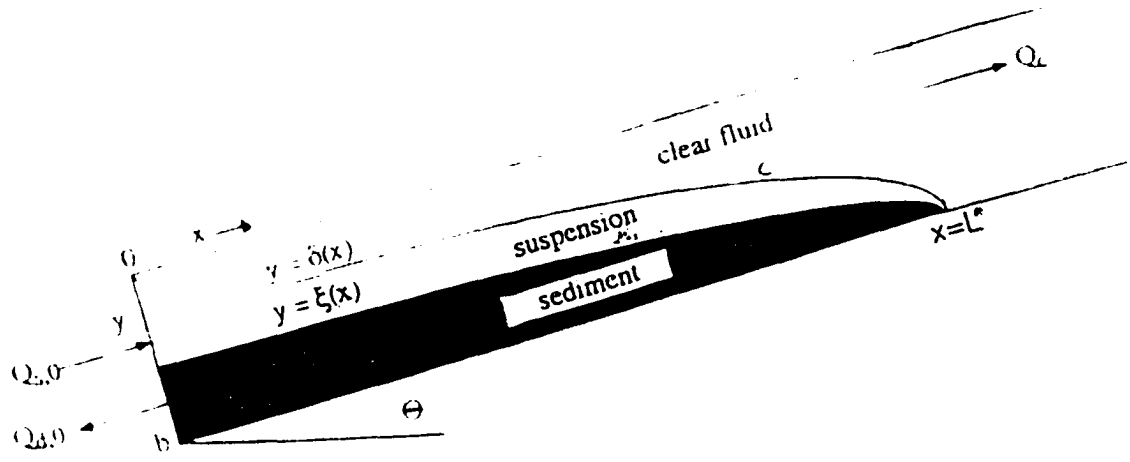

Figure 3.1: View of the inclined settler showing the definitions of the variables used in the analysis

sediment out of the suspension and that the overhead product will consist only of pure liquid. Clearly, such a continuous operation is possible only if the sediment can flow freely under gravity along the upward facing wall so that the particles can be collected at the bottom of the settler and be removed.

Let Q_{s0} and Q_{d0} denote, respectively, the volumetric flow rates, per unit depth, of the net feed and that of the sediment at the bottom of the settler and let us suppose further that the particle volume fraction within the

sediment equals the given value ϕ_d. Then, provided the overhead product is devoid of particles, we have, on account of an overall particle balance around the settler, that

$$Q_{s0}\phi_s - Q_{d0}\phi_d = 0. \tag{3.1}$$

In addition, let us suppose that the sediment along the upward facing surface extends over a distance L^* from the bottom of the settler, and let $u_t f(\phi_s)$ denote the settling speed of a representative particle within the suspension, where u_t refers to the Stokes settling speed of an isolated sphere and $f(\phi_s)$ is the familiar settling hindrance function which, following the usual practice, is taken to depend only on ϕ_s. A second overall particle balance around the sediment layer then yields

$$Q_{d0}\phi_d = Q_{d0}\phi_s + L^*\phi_s u_t f(\phi_s)\cos\theta \tag{3.2}$$

and hence, on account of equation (3.1),

$$Q_{s0} = \frac{L^* u_t f(\phi_s)\cos\theta}{(1 - \frac{\phi_s}{\phi_d})} \tag{3.3}$$

which relates Q_{s0} and L^*. In particular, in a settler of given length L, the volumetric feed rate Q_{s0} cannot exceed

$$Q_{s0}(max) = \frac{L u_t f(\phi_s)\cos\theta}{(1 - \frac{\phi_s}{\phi_d})} \tag{3.4}$$

if the overhead product is to remain free of particles. This is the well known Ponder- Nakamura-Kuroda (PNK) formula (see Acrivos & Herbolzheimer (1979)), modified to account for the presence of a sediment layer, which has played a key role in the design of supersettlers.

The expression given above for the maximum volumetric feed rate presupposes that the interface between the clear fluid and the suspension -c.f. curve C in figure 3.1 - remains stable and that any waves which may be generated do not break and thereby entrain particles into the clarified liquid. The stability of the flow configuration within supersettlers has therefore been studied extensively both theoretically as well as experimentally by Davis et al. (1983) and by Leung & Probstein (1983). On the other hand, as was mentioned earlier, another condition for the continuous operation of supersettlers, and therefore for the applicability of the PNK formula, refers to the requirement that the sediment layer be able to flow under gravity, so that the particles which have already settled can be removed. As we shall see presently, for a certain range of parameters, this can lead to values of the maximum permissible volumetric feed rate $Q_{s0}(max)$ which fall below those given by the PNK formula (equation (3.4)).

In two recent articles by Nir & Acrivos (1990) and by Kapoor & Acrivos (1995), the flow of a sediment layer that forms on an inclined plate in contact with a suspension of sedimenting particles above it, was investigated by means of a model in which the downward gravitational particle flux is opposed

by a shear-induced particle flux due to gradients in the particle concentration and in the shear stress. In general, as a consequence of this balance, the particle concentration within the sediment will remain everywhere below its maximum value $\phi_m \sim 0.58$, at which the suspension viscosity becomes infinite, and hence the sediment is able to flow under the action of gravity. It was also shown, however, that, if the angle of inclination θ falls below a critical value approximately equal to 10^o for a wide range of ϕ_s, a steady operation is no longer feasible and that the thickness of the sediment layer will grow indefinitely with time. This results from the fact that, at a critical angle, the particle concentration in the sediment adjacent to the upward facing surface equals the maximum value ϕ_m and, therefore, that portion of the sediment, on account of its infinitely large viscosity, is unable to flow and remains attached to the plate - see Kapoor & Acrivos (1995).

This analysis referred to above was, however, restricted to *low* aspect ratio settlers in which both the sediment and the clear fluid layers are everywhere very thin compared to the spacing, b, between the plates. But, from a practical point of view, one is primarily interested in the operation of *high* aspect ratio settlers, in which the thickness of the sediment and that of the clear fluid layer are comparable to b, because such settlers offer both increased efficiency as well as stability (- see Davis et al. (1983)). The flow of the suspension within a *high* aspect ratio vessel is accompanied, however, by a pressure drop along its length which opposes the downward flow of the

sediment, and hence, even if the conditions for the sediment flow set forth earlier by Kapoor & Acrivos (1995) are satisfied, i.e. even if the particle volume fraction adjacent to the upward facing surface remains below ϕ_m, the increased pressure drop resulting from an increase in Q_{s0} will eventually prevent the sediment from reaching the bottom of the settler and be collected. This then places a restriction on the maximum value of Q_{s0} which is quite distinct from that given by equation (3.4).

In this thesis, we present a theoretical and experimental study to examine the maximum value of the volumetric feed rate possible in an inclined settler operation continuously in the bottom feeding mode. Section 2 describes a theoretical analysis, leading to an expression for an upper bound on Q_{s0} that considers the hydrodynamic interaction between the suspension and the concentrated sediment in a continuous operation of high aspect ratio settlers. In §3, we describe our experiments and a comparison of our measurements with the theoretical predictions. The final section contains our conclusions.

2. Theoretical Analysis

Following Probstein et al. (1981) and Leung & Probstein (1983), we suppose that the settler is long enough relative to its width, so that the flow within each of the three phases, referred to earlier and depicted in figure 3.1, is everywhere quasi-parallel.[1] In addition, we model the suspension and the

[1]This quasi-parallel assumption does not apply of course near x=0 and $x = L^*/b$, i.e. within the entry and exit regions where inertia effects play an important role. For

sediment as effective Newtonian fluids having viscosities, relative to that of the clear liquid, equal to $\lambda(\phi_s)$ and $\lambda(\phi_d)$, respectively, where ϕ_s and ϕ_d are the corresponding particle volume fractions. Also, since it has been shown recently that, within a sediment flowing along the inclined plate, the particle concentration is, in general, fairly uniform, we shall take ϕ_d to be a constant and shall estimate its value by referring to the results of the more elaborate calculations presented by Kapoor & Acrivos (1995).

Under these circumstances then, the dimensionless Navier-Stokes equations within the clear fluid layer $0 < y < \delta(x)$ reduce to

$$\frac{\partial^2 u}{\partial y^2} - \frac{dP}{dx} + \Gamma \sin\theta = 0 \tag{3.5}$$

where u is the longitudinal component of the bulk velocity rendered dimensionless with u_t, y and x are, respectively, the transverse and longitudinal coordinates rendered dimensionless with b, the spacing between the plates, and P is the dynamic pressure divided by $u_t \mu_f / b$ where μ_f refers to the pure fluid viscosity. Finally

$$\Gamma = \frac{b^2 g \Delta\rho}{u_t \mu_f} \phi_s = \frac{9}{2} (\frac{b}{a})^2 \phi_s \tag{3.6}$$

where a is the radius of one of the spherical particles, g is the gravitational constant and $\Delta\rho$ is the difference between the density of the solid particles

moderate values of the bulk Reynolds number, however, the lengths of these regions are comparable to b, and hence their influence can be neglected in *high* aspect ratio vessels for which $L^*/b \gg 1$.

and that of the fluid. Similarly, within $\delta(x) < y < \xi(x)$ the region occupied by the suspension, we have

$$\lambda(\phi_s)\frac{\partial^2 u}{\partial y^2} - \frac{dP}{dx} = 0 \tag{3.7}$$

while, within the sediment, $\xi(x) < y < 1$,

$$\lambda(\phi_d)\frac{\partial^2 u}{\partial y^2} - \frac{dP}{dx} + \Gamma(1 - \frac{\phi_s}{\phi_d})\sin\theta = 0 \tag{3.8}$$

Equations (3.5.3.7-3.8), subject to the boundary conditions of no-slip at the two walls plus the requirement that the velocity and the shear stress be continuous across each of the two interfaces, can be readily integrated to yield the corresponding expressions for the velocities which are given in the Appendix. Using these velocity profiles, we obtain the following expressions for the volumetric flow rates per unit depth, rendered dimensionless with bu_t,

$$Q_c \equiv \int_0^{\delta(x)} u dy = F_3\frac{dP}{dx} + F_4\Gamma\sin\theta \tag{3.9}$$

$$Q_s \equiv \int_{\delta(x)}^{\xi(x)} u dy = F_5\frac{dP}{dx} + F_6\Gamma\sin\theta \tag{3.10}$$

$$Q_d \equiv -\int_{\xi(x)}^{1} u dy = -F_7\frac{dP}{dx} - F_8\Gamma\sin\theta \tag{3.11}$$

where the F's are functions of $\delta(x), \xi(x), \phi_s$ and ϕ_d as given in the appendix. We note that, if $\lambda(\phi_s)$ is set equal to unity, equations (3.9-3.11) become identical to those derived by Leung & Probstein (1983).

Next, to determine the remaining unknowns, $\delta(x), \xi(x)$ and dP/dx, we make use of the requirement that the particle flux be continuous across each of the two interfaces, $y = \delta(x)$ and $y = \xi(x)$, and that the net volumetric flow rate $Q_{net} \equiv Q_c + Q_s - Q_d$ be independent of x. These conditions lead to, respectively,

$$\frac{dQ_c}{dx} = f(\phi_s)\cos\theta, \tag{3.12}$$

$$\frac{dQ_s}{dx} = -\frac{\phi_d f(\phi_s)\cos\theta}{(\phi_d - \phi_s)} \tag{3.13}$$

and

$$\frac{dQ_d}{dx} = -\frac{\phi_s f(\phi_s)\cos\theta}{(\phi_d - \phi_s)}. \tag{3.14}$$

On integrating these along the length of the settler. we obtain that

$$Q_c = x f(\phi_s)\cos\theta, \tag{3.15}$$

$$Q_s = Q_{s0} - \frac{x\phi_d f(\phi_s)\cos\theta}{(\phi_d - \phi_s)} \tag{3.16}$$

and

$$Q_d = \frac{\phi_s}{\phi_d} Q_s, \tag{3.17}$$

where on account of equation (3.1), we have set $Q_{d0} = Q_{s0}\phi_s/\phi_d$. Note that equations (3.15-3.17) differs from equations (34-36) in Leung & Probstein (1983), who used an incorrect expression for the continuity of particle flux across the interface $y = \xi(x)$. Finally, on using the fact that both $Q_s(x)$ and $Q_d(x)$, as given by equations (3.16)& (3.17), must vanish at $x = L^*/b$,

we recover the expression for Q_{s0} given by equation (3.3), if the latter is rendered dimensionless by dividing both sides with bu_t. Thus, for a given dimensionless inlet feed rate Q_{s0}, we have that, as before

$$\frac{L^*}{b} = \frac{Q_{s0}(\phi_d - \phi_s)}{\phi_d f(\phi_s)\cos\theta}. \tag{3.18}$$

As was said earlier, for a settler of finite length L, a necessary condition for the present analysis to apply is that $L^* \leq L$, because, if the feed rate exceeds the maximum value given by equation (3.4), the excess suspension will leave the settler together with the clear fluid.

In addition, however, we require that equations (3.9-3.17) have a solution with $\delta = 0$ at x=0 and $\xi = 1$ at $x = L^*/b$. We therefore examine the set, which we obtain by substituting the corresponding flow rates from equations (3.15-3.17) into equations (3.9-3.11),

$$-F_3F + \beta F_4 = \frac{bx}{L^*} \tag{3.19}$$

$$-F_5F + \beta F_6 = \frac{\phi_d}{(\phi_d - \phi_s)}\{1 - \frac{bx}{L^*}\} \tag{3.20}$$

$$-F_7F + \beta F_8 = \frac{\phi_s}{(\phi_d - \phi_s)}\{\frac{bx}{L^*} - 1\} \tag{3.21}$$

where F and β are given by, respectively,

$$F \equiv -\frac{\phi_d}{Q_{s0}(\phi_d - \phi_s)}\frac{dP}{dx} = \frac{\beta(F_4 + F_6 + F_8) - 1}{F_3 + F_5 + F_7} \tag{3.22}$$

$$\beta \equiv \Gamma \frac{\phi_d \sin\theta}{Q_{s0}(\phi_d - \phi_s)}. \tag{3.23}$$

Note that the relation between F and the other F's given by equation (3.22) follows by adding equations (3.19-3.21), hence only two of the latter three equations are independent.

Now, given ϕ_s, ϕ_d and β, it is straightforward matter to determine δ and ξ, as functions of bx/L^*, by solving the set of non-linear algebraic equations (3.20), (3.21) and (3.22), or (3.19), (3.21) and (3.22), subject to the constraints: $\delta = 0$ at x=0 and $\xi = 1$ at bx/L^*. The solution can begin of course at either x=0 or at $x = L^*/b$. In addition, we require that, at x=0, the velocity u within the sediment be everywhere negative or zero which means, in particular, that u_{s-d}, the velocity along the suspension-sediment interface, cannot be positive at the entrance of the channel.

Now, on setting x=0 and $\delta = 0$, we find that equation (3.19) is satisfied automatically and that, for a wide range of β, the remaining set of equations yields two roots for $\xi(0)$, both lying between 0 and 1, as shown in figure 3.2 for a typical choice of ϕ_s and ϕ_d. But, since $(d\xi/dx)_{x=0} < 0$ for any computation starting from any point along the curve BD shown in figure 3.2, the constraint $\xi = 1$ at $bx/L^* = 1$ cannot be satisfied using the value of $\xi(0)$ at that point as an initial condition. Also, the velocity along the suspension-sediment interface, u_{s-d}, is positive along the curve CD where C denotes the location of the point where $u_{s-d} = 0$. It is found moreover that, as ϕ_s decreases, C approaches point B where $(d\xi/dx)_{x=0} = 0$, and eventually

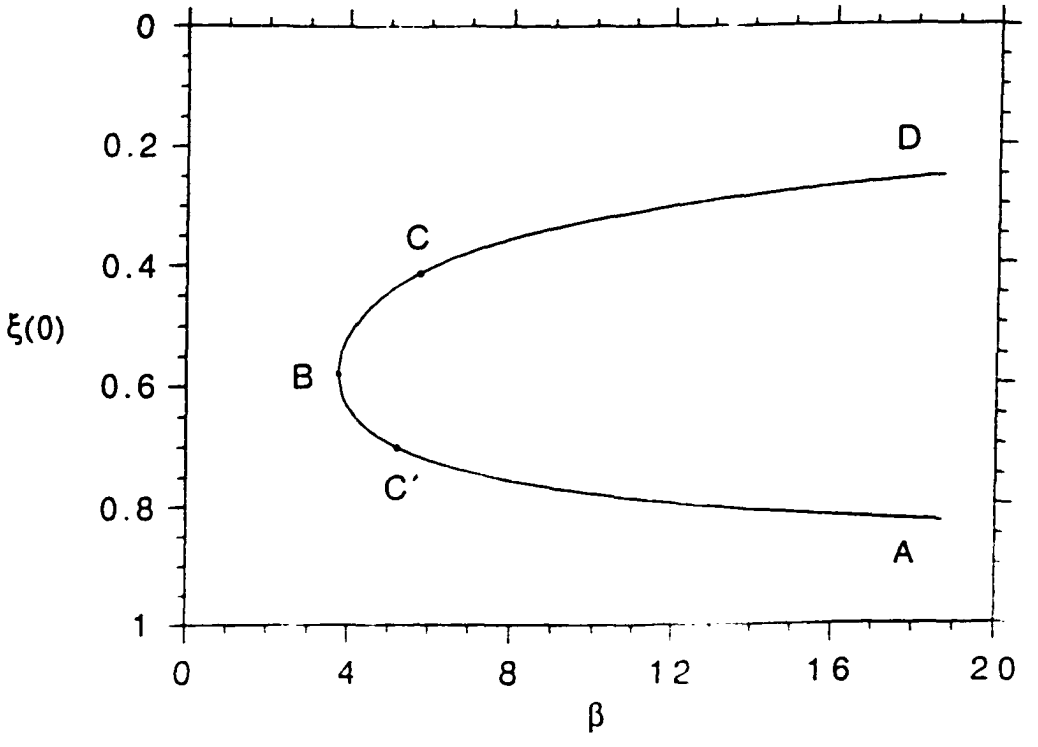

Figure 3.2: $\xi(0)$ as a function of β for $\phi_s = 0.01$ and $\phi_d = 0.52$.

crosses over to the lower branch BA (shown in figure 3.2 as C') when ϕ_s falls below 0.0017(for $\phi_d = 0.52$). Hence, as $\phi_s \rightarrow 0$, only the lower curve C'A is of any significance. We conclude therefore that the system of equations together with the constraints as given above has a unique solution. This was also pointed out by Leung & Probstein (1983). In addition, β cannot fall below a minimum value β_{min} given by the point B(or C' if $\phi_s < 0.0017$ for $\phi_d = 0.52$) in figure 3.2. This can also be demonstrated by starting the computations at $bx/L^* = 1$ and $\xi = 1$ and then decreasing x.

At high values of β, corresponding to low feed flow rates Q_{s0}, the thicknesses of both the clear fluid layer and that of the sediment are small relative

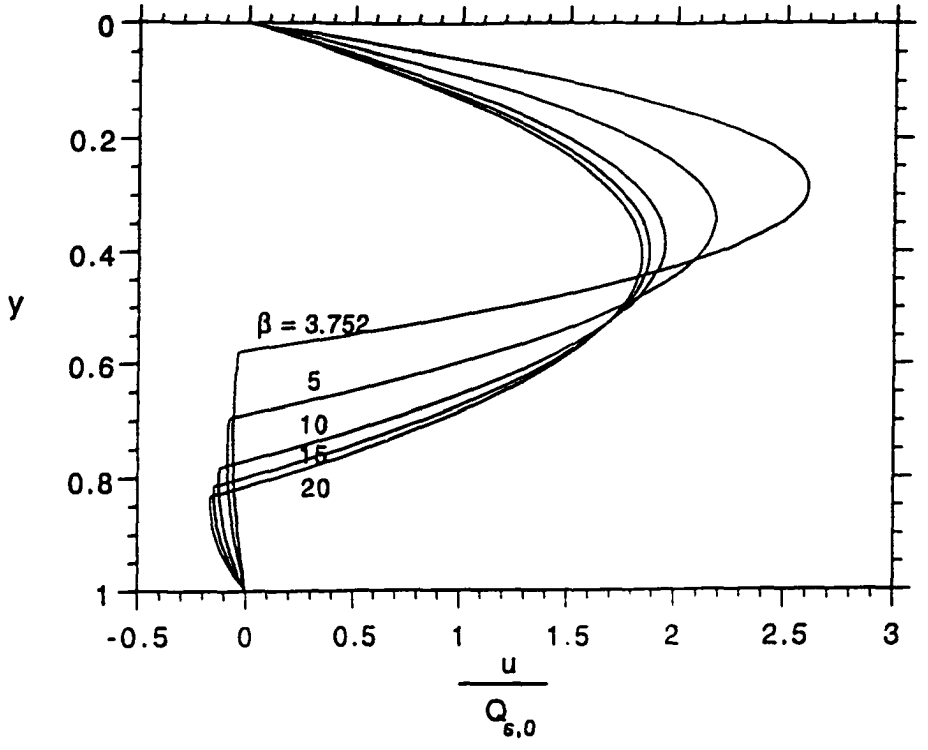

Figure 3.3: Dimensionless velocity profiles. $u_s(y)$ and $u_d(y)$, at x=0 for ϕ_s = 0.01 and $\phi_d = 0.52$.

to the spacing between the plates and, hence, the device operates as a *low aspect ratio* settler. But with decreasing β, i.e. with an increase in the feed flow rate Q_{s0} and therefore in the amount of material that enters the settler as feed, there is an increase in the thickness of the sediment layer at x=0, as well as a corresponding increase in the pressure drop along the channel which opposes the downward flow of the sediment. This tendency of the flow to choke is illustrated in figures 3.3 and 3.4 for a typical choice of ϕ_s and ϕ_d. Moreover since, as shown in figure 3.2, there exists no solution for $\beta < \beta_{min}$, this places a restriction on the maximum permissible value of Q_{s0}. The existence of β_{min}, whose value depends only on ϕ_s and ϕ_d, appears to have been overlooked in the earlier investigation by Leung & Probstein (1983).

As was mentioned earlier, β_{min} is given by point C' in figure 3.2 for $\phi_s < 0.0017$ (when ϕ_d=0.52). But, on noting that u_{s-d}=0 at C', we can construct the asymptotic solution of equation (3.20) and equation (3.22) at x=0, as $\phi_s \to 0$ and show after some algebra that

$$\beta_{min}(\phi_s \to 0) = 12\{1 + \sqrt{\frac{\phi_s \lambda(\phi_d)}{\phi_d}}\}^4 \sqrt{\frac{\phi_s}{\phi_d \lambda(\phi_d)}}. \tag{3.24}$$

Numerical results were obtained for β_{min}, given by the condition $(d\xi/dx)_{x=0} = 0$ (point B in figure 3.2) or $u_{s-d} = 0$ for $\phi_s \to 0$ (point C'). These are presented in figure 3.5 where we have plotted $\beta_{min}/\beta_{min}(\phi_s \to 0)$ vs ϕ_s with ϕ_d as a parameter, while, shown in figure 3.6 are the profiles for $\delta(x)$ and $\xi(x)$ for $\phi_s = 0.01$, $\phi_d = 0.52$ and $\beta = \beta_{min} = 3.75$. Clearly, β_{min} is a sensitive function of ϕ_d. For example, when ϕ_d is increased from 0.50 to 0.55, β_{min} increases from 3.38 to 5.68 (for $\phi_s = 0.01$).

Returning now to the conditions for determining the maximum volumetric feed rate for given values of ϕ_s and ϕ_d, we see from equations (3.18) and (3.23) that the dimensional flow rate Q_{s0} cannot exceed that given either by equation (3.4) or by

$$\frac{bu_t \Gamma \sin\theta}{\beta_{min}(\phi_s, \phi_d)(1 - \phi_s/\phi_d)} \tag{3.25}$$

whichever is smaller. This means that $Q_{s0}(\max)$ is given by the PNK formula, equation (3.4), for $\theta_{crit} \leq \theta < \pi/2$, while, for $0 < \theta \leq \theta_{crit}$, it equals equation (3.25), where

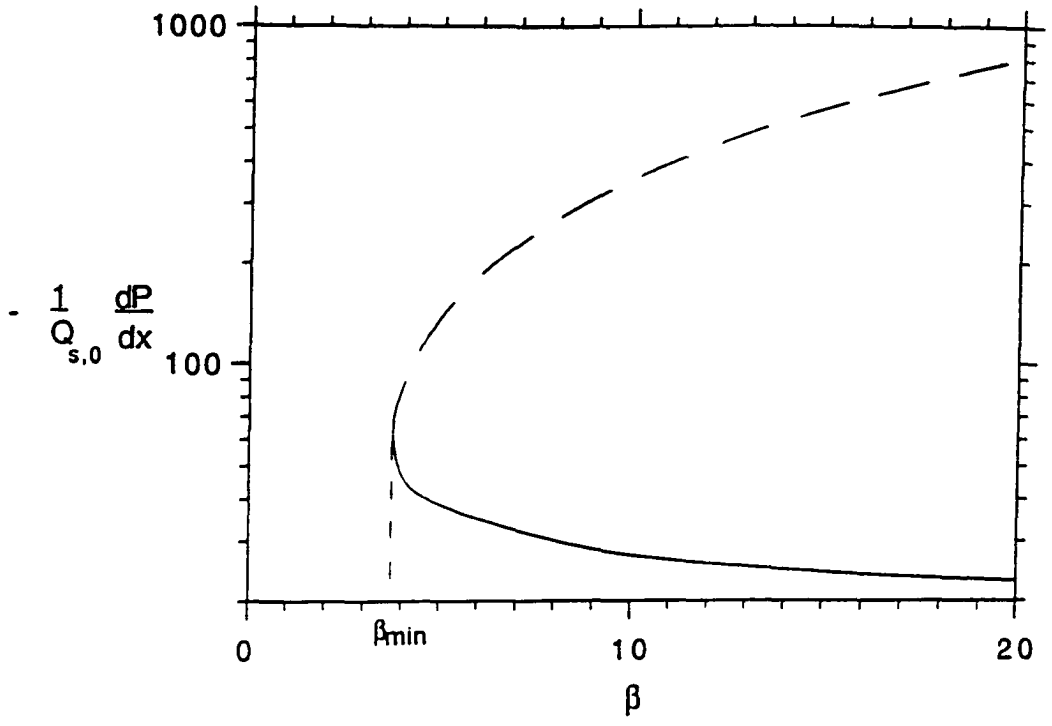

Figure 3.4: The dimensionless pressure gradient at at x=0 divided by the dimensionless feed rate, Q_{s0}, as a function of β for $\phi_s = 0.01$ and $\phi_d = 0.52$ for which $\beta_{min} = 3.75$.

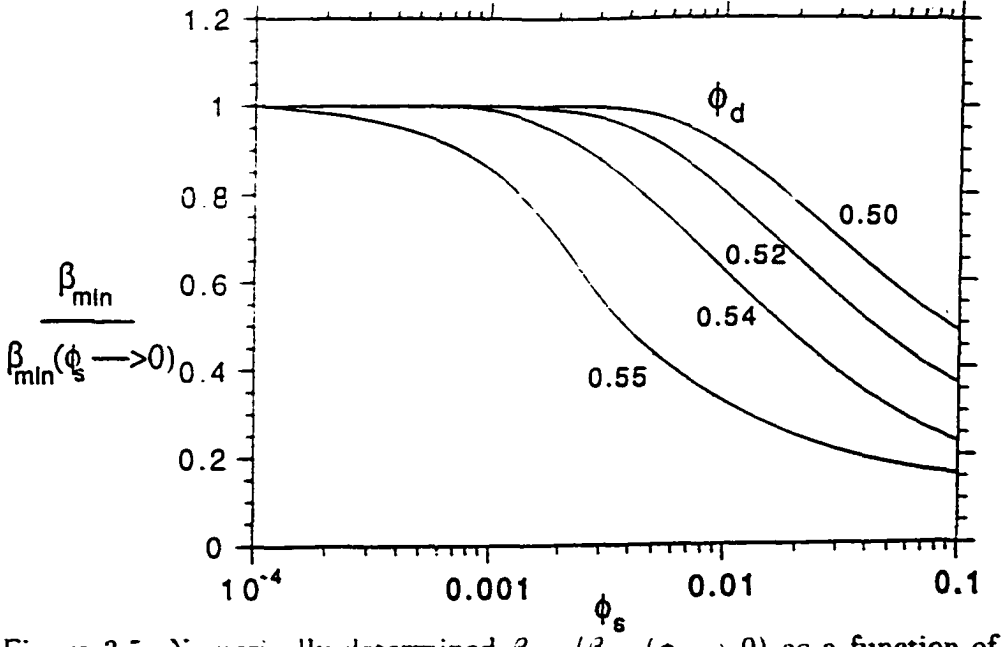

Figure 3.5: Numerically determined $\beta_{min}/\beta_{min}(\phi_s \to 0)$ as a function of ϕ_s with ϕ_d as a parameter. Here $\beta_{min}(\phi_s \to 0)$ is given by eq.(3.24).

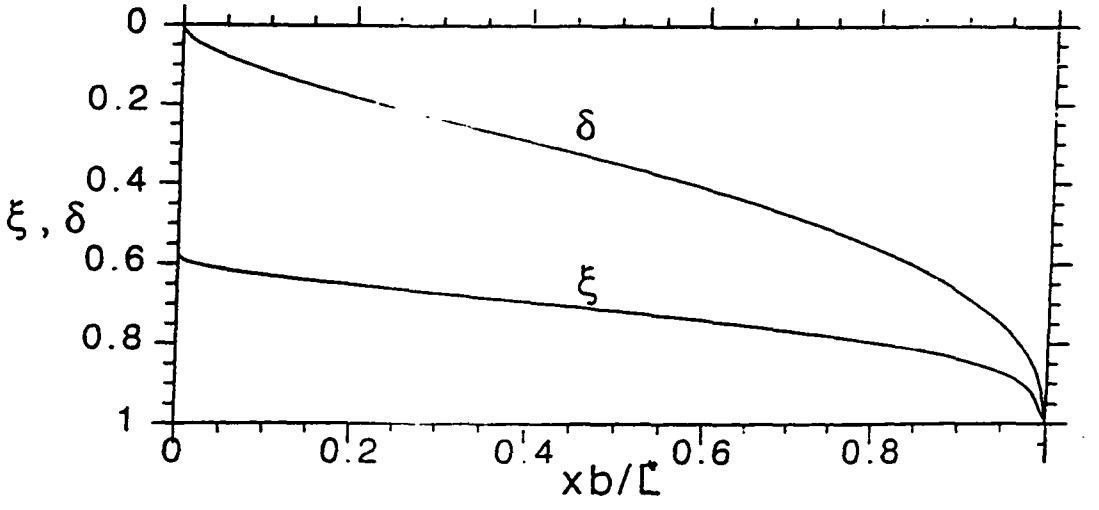

Figure 3.6: Profiles of $\delta(x)$ and $\xi(x)$ for $\phi_s = 0.01$, $\phi_d = 0.52$ and $\beta = \beta_{min} = 3.75$.

$$\theta_{crit} = \arctan\{\frac{\beta_{min}(\phi_s, \phi_d) f(\phi_s) L}{b\Gamma}\} \tag{3.26}$$

as obtained by equating equation (3.4) and equation (3.25). We can also see readily that, for a settler of given dimensions, the global maximum permissible value of Q_{s0} is reached when $\theta = \theta_{crit}$, in which case

$$Q_{s0}(max) = \frac{bu_t L f(\phi_s)\Gamma}{(1 - \phi_s/\phi_d)\sqrt{(b\Gamma)^2 + (\beta_{min}(\phi_s, \phi_d) f(\phi_s) L)^2}} \tag{3.27}$$

Note that ϕ_d is, strictly speaking, not an independent parameter since, in principle at least, one should be able to extend the analysis by Kapoor & Acrivos (1995) to high aspect ratio vessels and thereby determine the particle concentration profile within the sediment. In that case θ_{crit} would be found

to depend only on ϕ_s. The analysis leading to that result, however, has not been attempted thus far.

3. Experiments and comparison with the theory

3.1. Experimental set-up

The predictions based on the theory developed in the previous section were tested experimentally by measuring the maximum possible feed rate for the operation of a high aspect ratio inclined settler. The set-up, shown schematically in figure 3.7, consisted of a high aspect ratio settler of dimensions 75cm(L) x 2.5cm(W) x 2cm(b) which was connected to the flow system mounted on a pivoting stand so that it could be rotated to the desired angle of inclination. The settler had an inlet port for the suspension and outlet ports for the sediment and for the clear fluid. An adjustable flipper was attached at the entrance of the channel which functioned both as an entrance guide for the feed and as a baffle that segregated the feeding and sediment collecting sections. In this way, any entrainment of the sediment by the incoming suspension feed was minimized. In order to be able to operate the high aspect ratio settler, it was necessary to design the flipper properly.

Polystyrene spheres, obtained from Maxiblast Inc., were used in the experiments. These particles were a lot of class PB-2.5. The polydisperse material was sieved to obtain a uniform fraction in the size range $425 - 500\mu m$,

with a standard deviation of $37.5\mu m$. The density of polystyrene spheres was measured to be 1.045gm/cc. The suspending fluid consisted of a mixture of 40%(by volume) terpentine and 60% santisizer 278 fluid. The density and viscosity of the suspending fluid was measured to be 0.9881gm/cc and 0.143P(@$24^{o}C$) respectively. Polystyrene spheres were negatively buoyant and visible(refractive index mismatched) in the suspending fluid.

The details of the flow system are shown schematically in figure 3.7. The clear fluid and the sediment that were withdrawn from the settler were eventually remixed in a mixing chamber which was equipped with a mechanical stirrer and cooling coils to maintain a constant temperature. The temperature of the suspension in the mixing tank was monitored by means of a thermistor probe and was controlled manually by changing the set point of the temperature of the water in a circulator bath(Model RTE-221) which circulated through the cooling coils of the mixing tank. The suspension feed rate was measured using a flowmeter which was calibrated accurately with the suspending fluid used in the experiment. A progressive cavity pump, made by Moyno Inc., was used to provide uniform suspension flow rates. The pump was capable of handling flow rates up to 0.75 GPM without any suction of air bubbles. In addition, the concentrated sediment leaving the settler was pumped into the mixing tank by means of a peristaltic pump. Tygon tubing was used to connect the different units. This arrangement allowed us to operate the high aspect ratio settler continuously.

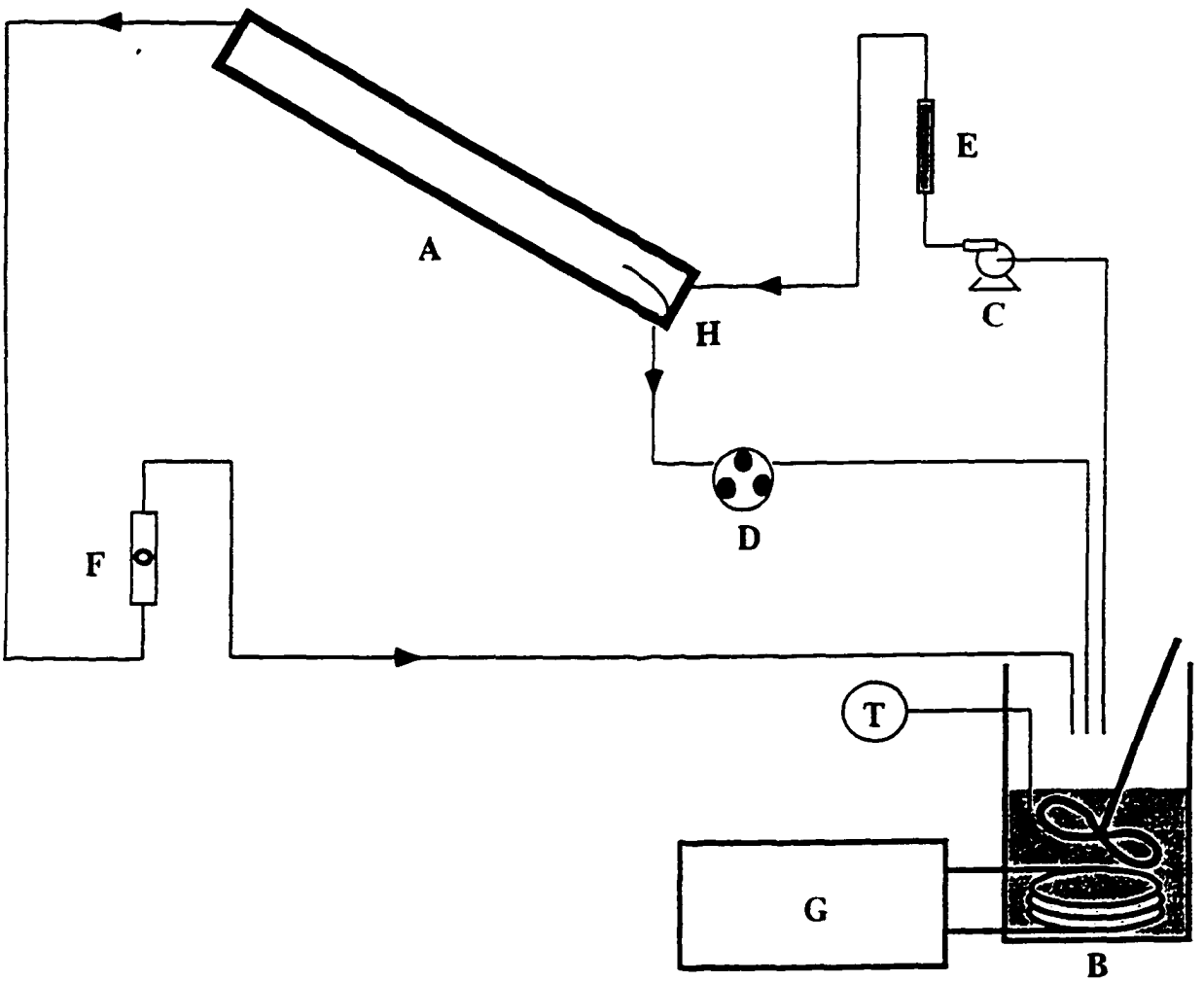

Figure 3.7: Schematic representation of the flow system. A: flow vessel, B: mixing tank, C: progressive cavity pump, D: peristaltic pump, E: flow meter, F: flow meter, G: temperature controlled bath, H: flipper, T: thermometer.

3.2. The start-up procedure

The following procedure was followed in starting the continuous operation of the settler. Initially, a suspension having the desired concentration and volume was loaded into the mixing tank and was maintained in suspension by the stirrer. The latter was set at an appropriate speed to avoid air bubble entrainment. The settler was then inclined at the desired angle. The temperature controlling unit and the tank outlet were opened to prime the progressive cavity pump. The sediment outlet at the bottom of the settler and the peristaltic pump were closed. The progressive cavity pump was then turned on and the suspension was made to flow through the settler at a low flow rate. Next, the peristaltic pump and the sediment outlet were slowly opened. By adjusting the speed of the peristaltic pump, a steady output of the sediment was maintained. After each successive increase in the suspension flowrate, the flipper was adjusted in order to eliminate the entrainment of the downward flowing sediment. Steady state was normally achieved in one to two hours. Attainment of the steady state was confirmed by the measurements of the flow rates of the feed and that of the overflow stream. Simultaneously, the sediment layer thickness and L^* were also observed. This start-up procedure enabled us to achieve a flow completely free of air bubbles, cavitation and any choking of the tubes.

3.3. Results and comparison with the theory

Visual observations of the flowing sediment layer clearly indicated a sharp change in contrast around the sediment-suspension interface. This feature of the sediment interface allowed us to observe the increase in the sediment layer thickness with suspension feed rate. Following the procedure described in §3.2, the suspension feed rate, Q_{s0}, was increased in small steps and the flow system was allowed to reach steady state. At each of these steps, the flow of the sediment and its thickness were closely watched. After reaching a critical Q_{s0}, we found the sediment thickness started increasing continuously with time within the channel so that a steady state could no longer be achieved. This allowed us to determine the maximum possible feed rate under the given conditions of the feed concentration and of the angle of inclination. These experiments were repeated for $\phi_s = 5\%, 7.5\%\&10\%$ and $\theta = 35^o. 40^o\&45^o$. The measured $Q_{s0}(\max)$ was then inserted into equation (3.23) and an experimentally observed value of β_{min} was thus obtained. Table 1 shows an excellent agreement with the theoretical predictions. This demonstrates the existence of a maximum allowable feed rate in the continuous operation of high aspect ratio settlers which is distinct from that found via the well-known PNK theory, equation (3.4).

ϕ_s	β_{min} (from theory)	θ	β_{min} (from experiments)
0.05	44.38	35^o	56.74
		37.5^o	54.12
0.075	94.7	35^o	107.7
		40^o	116.75
		45^o	103.16
0.10	171.53	35^o	159.66
		40^o	156.65
		45^o	151.14

Table 3.1: Comparison between the theoretical solution described in §2 and the experimentally observed value of β_{min} for $\phi_d = 0.52$.

4. Conclusions

A new upper bound for the maximum value of the volumetric feed rate in a continuously operated high aspect ratio inclined settler which can be tolerated under a given set of conditions was found theoretically as well as experimentally. The theoretical analysis was based on considering the hydrodynamic interaction between the suspension and the concentrated sediment in an inclined settler operating continuously in the bottom feeding mode. It was found that the experimental results for β_{min} were in good agreement with the corresponding theoretical predictions for $0.50 \leq \phi_d \leq 0.55$.

All the results described in this thesis pertain to the bottom feeding high aspect ratio settler, where the presence of a large pressure gradient, which opposes the downward flow of the sediment, introduces a constraint on the

maximum permissible feed flow rate for continuous operation. In contrast, when the settler is operated in the top feeding mode, a simple analysis, along the lines given earlier, shows that the pressure decreases as one proceeds down the channel, which means that the resulting pressure drop aids rather than hinders the sediment flow. Thus, provided that the angle of inclination exceeds the critical value found earlier by Kapoor & Acrivos (1995) for the flow along an inclined plate of a concentrated sediment in contact with a stagnant sedimenting suspension, the presence of this sediment does not place an additional constraint on the maximum allowable feed rate. In other words, in a settler of effectively infinite length, the expression for $Q_{s0}(\max)$ derived earlier by Davis et al.(1983), for the case $\lambda(\phi_s) = 1$,

$$Q_{s0}(max) = \frac{bu_t\Gamma \sin\theta}{192} \tag{3.28}$$

would be expected to apply with only minor modifications. The above expression is of course similar to equation (3.25) which applies for the bottom feeding mode. But since, as was shown earlier, β_{min} is $O(10)$, we conclude that, in settling vessels of effectively infinite length, the maximum volumetric feed rate for the bottom feeding mode can exceed that for the top feeding mode by an order of magnitude under otherwise identical conditions.

We conclude by noting that the results presented above are particularly significant in that they provide an improved theoretical basis for the design and optimal performance of supersettlers.

5. Appendix

The solution of equations (3.5), (3.7) and (3.8) is:

$$u_c = \left(\frac{dP}{dx} - \Gamma \sin\theta\right)\frac{y^2}{2} + c_1 y \tag{3.29}$$

$$u_s = \frac{1}{\lambda(\phi_s)}\left(\frac{dP}{dx}\frac{y^2}{2} + c_3 y + c_4\right) \tag{3.30}$$

$$u_d = \frac{1}{\lambda(\varphi_d)}\left[\left\{\frac{dP}{dx} + \left(\frac{\phi_d}{\varphi_s} - 1\right)\Gamma \sin\theta\right\}\frac{y^2}{2} + c_5 y + c_6\right] \tag{3.31}$$

$$c_1 = c_3 + \delta\Gamma \sin\theta \tag{3.32}$$

$$c_3 = F_1\frac{dP}{dx} + f_2\Gamma \sin\theta \tag{3.33}$$

$$c_4 = \lambda(\phi_s)\left\{\left(\frac{dP}{dx}\frac{\delta^2}{2} + c_3\delta\right)\left(1 - \frac{1}{\lambda(\phi_s)}\right) + \frac{\delta^2}{2}\Gamma \sin\theta\right\} \tag{3.34}$$

$$c_5 = c_3 - \xi\left(\frac{\phi_d}{\varphi_s} - 1\right)\Gamma \sin\theta \tag{3.35}$$

$$c_6 = -\frac{1}{2}\left\{\frac{dP}{dx} + \left(\frac{\phi_d}{\varphi_s} - 1\right)\Gamma \sin\theta\right\} - c_3 + \xi\left(\frac{\varphi_d}{\varphi_s} - 1\right)\Gamma \sin\theta \tag{3.36}$$

$$A = -\frac{1}{2}\left[\delta^2\left(1 - \frac{1}{\lambda(\varphi_s)}\right) + \xi^2\left(\frac{1}{\lambda(\varphi_s)} - \frac{1}{\lambda(\phi_d)}\right) + \frac{1}{\lambda(\phi_d)}\right] \tag{3.37}$$

$$B = -\frac{1}{2}\left[\frac{(\varphi_d/\varphi_s - 1)(\xi - 1)^2}{\lambda(\varphi_d)} + \delta^2\right] \tag{3.38}$$

$$D = \delta\left(1 - \frac{1}{\lambda(\varphi_s)}\right) + \xi\left(\frac{1}{\lambda(\varphi_s)} - \frac{1}{\lambda(\varphi_d)}\right) + \frac{1}{\lambda(\phi_d)} \tag{3.39}$$

$$F_1 = \frac{A}{D} \tag{3.40}$$

$$F_2 = \frac{B}{D} \tag{3.41}$$

$$F_3 = \frac{\delta^3}{6} + F_1\frac{\delta^2}{2} \tag{3.42}$$

$$F_4 = \frac{\delta^2}{2}(F_2 + \delta) - \frac{\delta^3}{6} \tag{3.43}$$

$$F_5 = \frac{(\xi^3 - \delta^3)}{6\lambda(\phi_s)} + \frac{F_1(\xi^2 - \delta^2)}{2\lambda(\phi_s)} + \left(1 - \frac{1}{\lambda(\phi_s)}\right)\left(\frac{\delta^2}{2} + \delta F_1\right)(\xi - \delta) \tag{3.44}$$

$$F_6 = \frac{(\xi^2 - \delta^2)}{2\lambda(\phi_s)}F_2 + \left[\delta\left(1 - \frac{1}{\lambda(\phi_s)}\right)F_2 + \frac{\delta^2}{2}\right](\xi - \delta) \tag{3.45}$$

$$F_7 = \frac{1}{\lambda(\phi_d)}\left[\frac{(1-\xi^3)}{6} + \frac{(1-\xi^2)F_1}{2} - (F_1 - \frac{1}{2})(1-\xi)\right] \tag{3.46}$$

$$\begin{aligned} F_8 \;=\; & \frac{1}{\lambda(\phi_d)}\left[\frac{(1-\xi^3)(\phi_d/\phi_s - 1)}{6} + \frac{(1-\xi^2)\{F_2 - \xi(\phi_d/\phi_s - 1)\}}{2}\right] \\ & + \frac{1}{\lambda(\phi_d)}\left[\{(\xi - \frac{1}{2})(\phi_d/\phi_s - 1) - F_2\}(1-\xi)\right] \end{aligned} \tag{3.47}$$

6. References

Acrivos, A. & Herbolzheimer, E. 1979 Enhanced sedimentation in settling tanks with inclined walls. *J. Fluid Mech.* **92**, 435-457.

Davis, R. H., Herbolzheimer, E. & Acrivos, A. 1983 Wave formation and growth during sedimentation in narrow tilted channels. *Phys. Fluids* **26**, 2055-2064.

Kapoor, B. & Acrivos, A. 1995 Sedimentation and sediment flow in settling tanks with inclined walls. *J. Fluid Mech.* **290**, 39-66.

Leung, W. F. & Probstein, R. F. 1983 Lamella and tube settlers 1. Model and operation. 2. Flow stability. *Ind. Engng Chem. Proc. Des, Rev.* **22**, 58-67.

Nir, A. & Acrivos, A. 1990 Sedimentation and sediment flow on inclined surfaces. *J. Fluid Mech.* **212**, 139-153.

Probstein, R. F., Yung, R. & Hicks, R. 1981 In Physical Separations (ed. M. P. Freeman & J. A. Fitzpatrick, New York : Engineering Foundation), 53-92.

Chapter 4

Measurements of Particle Velocity Fluctuations in Concentrated Suspensions Undergoing Shear

abstract

Using laser Doppler anemometry(LDA) particle velocity fluctuations in concentrated suspensions (20% - 40% solids volume fraction) of non-colloidal spheres (325 μm average diameter) were measured in the velocity gradient, vorticity and flow directions in a narrow gap Couette device for values of the applied shear rate γ ranging from 3 to $16s^{-1}$. The purpose of these measurements was to provide information about values of the so-called *suspension temperature* T which equals the sum of the translational velocity fluctuations for a particle relative to its mean translational velocity. All the measurements

were corrected for the influence of the LDA noise. Unfortunately, the order of magnitude of the LDA noise and of the particle velocity fluctuations was found to be the same and, in addition, the latter included a contribution of the particle rotation which does not enter into the expression of T and which could not be removed from the measured data. Hence, any quantitative conclusions regarding T could not be made even though the measured experimental results were comparable to those obtained by Shapley *et al.* (1997). Finally, a suggestion is made on how the problems of the particle rotation and the LDA noise could be overcome.

1. Introduction

Recent experiments(e.g. Leighton & Acrivos, 1987, Koh, *et al.* , 1991, Sinton & Chow, 1991; Abbott, *et al.* , 1991; Phillips, *et al.* , 1992; Chow *et al.* , 1994; Kapoor & Acrivos, 1995) on the flow of concentrated suspensions have focused on measuring the mean velocity and particle concentration profiles in simple geometries. These experiments support the claim that particles in suspensions migrate from regions of high shear rate to low as well as from high particle concentrations to low. Also, based on these experiments, considerable progress has been made in developing mathematical models for this migration process in slow flows of concentrated suspensions. These models lead to a diffusion equation for the particle concentration to be solved in conjunction with the continuity and momentum equations for the entire suspension.

From a fundamental point of view, the studies mentioned above have proposed various mechanisms for particle migration based on the notion that an average particle moves randomly as it follows the streamlines of the mean flow. This random motion, which leads to a diffusive behavior, arises due to the chaotic nature of the particle evolution equation in concentrated suspensions. Leighton and Acrivos (1987) attributed this diffusive behavior to the existence of a small scale surface roughness on the particles, while Abbott *et al.* (1991) attributed it to forces not accounted for by the Stokes equations. Hence, there exist some disparities in describing all interactions and the re-

sultant migration phenomenon. This provides a need and a motivation for a further investigation of this subject, both experimentally and theoretically.

Recently, Nott & Brady(1994) proposed a *suspension balance* model, similar to that presented by Jenkins & McTique(1990) for the flow of granular materials, which involves the mean square of the velocity fluctuations plus a balance law and boundary conditions for its determination. Nott & Brady (1994) then constructed and solved the macroscopic mass, momentum and energy balances and showed that their model is consistent with the results of Stokesian dynamics simulations in which the particle velocity fluctuations are determined numerically. These authors also computed the shear-induced particle diffusion in a homogeneous shear flow as well as the migration of particles in inhomogeneous flows arising from the chaotic motion of the particles. A key term in their model is the *suspension temperature* which is used to quantify the random motion of the particles about their mean velocity, and is defined as (Nott & Brady. 1993)

$$T = \langle u_r'^2 \rangle_p + \langle u_z'^2 \rangle_p + \langle u_\theta'^2 \rangle_p, \tag{4.1}$$

where u_r', u_z'&u_θ' are the fluctuations of the translational velocity of a particle about its mean translational velocity in the velocity gradient, vorticity and the flow directions, respectively and the angle brackets denote an ensemble average over all the particles. Since the *suspension temperature* is a measure of the random kinetic energy of the flow, it replaces the thermody-

namic temperature in the dense-gas kinetic theory analysis. In addition, the fluctuating motion of the particles is closely connected to the shear-induced particle tracer diffusivity, D, because the latter is related to the mean square particle displacement and the particle velocity fluctuation autocorrelation function by means of

$$D = \lim_{t\to\infty} \frac{1}{2}\frac{d}{dt}\langle (x - \langle x\rangle_p)^2\rangle_p = \int_0^\infty \langle u'(0)\cdot u'(t)\rangle_p dt. \qquad (4.2)$$

Although the *suspension temperature* is a key property in such theoretical studies, only a few attempts have been made to experimentally measure its magnitude. Ahn, *et al.* (1991) and Hsiau & Hunt(1993) measured only the streamwise fluctuation velocity component in granular media using fiber-optic probes, while Drake(1991) measured both fluctuation velocity components in a two-dimensional granular flow down an inclined chute using a high-speed photographic technique. Recently, Natarajan *et al.* (1995) used imaging methods to measure two components of the average and fluctuating velocities in a two-dimensional flow of a granular material. Also, Nicolai *et al.* (1995 & 1996) have measured the particle velocity fluctuations and self-diffusivities of sedimenting suspensions by an imaging technique. Recently, Shapley *et al.* (1997) have presented their preliminary work on the LDA measurements of particle velocity fluctuations in concentrated suspensions at the annual meeting of Society of Rheology. Since these authors are still in the process of completing their work, we shall discuss only their

preliminary results available to us so far.

In this chapter, we present an experimental study for measuring such particle velocity fluctuations in a concentrated suspension being sheared in a Couette device in which the particle velocity and velocity fluctuations are determined using the technique of laser Doppler anemometry (LDA). Our objective is to obtain a direct experimental measurement of the *suspension temperature* that can be used to test the Nott-Brady migration theory and constitutive equations based on their *suspension balance* model. In section §2, we briefly describe various macroscopic models for suspension flows as they pertain to Couette flows. Details of the experimental facility are described in §3 together with the instrumentation used for the particle fluctuation measurements. The final section contains results and discussion.

2. Macroscopic models for suspension flow

2.1. Diffusive flux model

Leighton & Acrivos (1987 a&b) proposed a diffusive model to explain their observations of the apparent long-time decrease and short-time increase in the effective viscosity of a suspension as measured in a Couette viscometer. This model was used later by Phillips *et al.* (1992) to predict the concentration inhomogeneity in the pressure-driven flow in a tube and in a wide-gap Couette flow. In their model, the net flux of particles consists of two contributions: a diffusive flux driven by a gradient in the shear rate and a diffusive flux due

to a gradient in the concentration. In the notation of Phillips *et al.* (1992), the diffusion equation for the particles is

$$\frac{\partial \phi}{\partial t} = \frac{a^2}{r}\frac{\partial}{\partial r}\{r[K_c\phi\frac{\partial}{\partial r}(\gamma\phi) + K_\eta(\gamma\phi^2)\frac{1}{\eta}\frac{\partial \eta}{\partial \phi}\frac{\partial \phi}{\partial r}]\} \tag{4.3}$$

where a is the particle radius, K_c and K_η are proportionality constants, and η is the relative effective viscosity of the suspension. In a Couette flow $\gamma = \gamma_{r\theta}$ is the local shear rate which is determined by momentum conservation. For the case of a Couette flow, the net flux in the radial direction vanishes at steady state and hence equation (4.3) reduces to

$$\frac{\gamma\phi}{\gamma_w\phi_w} = (\frac{\eta_w}{\eta})^{\frac{K_\eta}{K_c}} \tag{4.4}$$

where the subscript w denotes properties at the inner cylinder wall.

From experimental data on Couette flows, Phillips *et al.* found that $K_c/K_\eta \approx$ 0.66. and therefore, using Kreiger's formula for the effective viscosity,

$$\eta = (1 - \phi/\phi_m)^{-1.82} \tag{4.5}$$

where η and ϕ_m are the viscosity of the suspending fluid and the maximum concentration respectively, they obtained that

$$\phi = \phi_m\frac{r^2}{(r^2 + \alpha R_i^2)} \tag{4.6}$$

The constant $\alpha = (\phi_m - \phi_w)/\phi_w$ is determined by applying the condition that the average particle concentration $\bar{\phi}$ is known, hence

$$\bar{\phi} = \frac{2}{R_o^2 - R_i^2}\int_{R_i}^{R_o} \phi r dr = \phi_m[1 - \frac{R_i^2}{R_o^2 - R_i^2} ln \frac{R_o^2 + \alpha R_i^2}{R_i^2(1+\alpha)}], \qquad (4.7)$$

where R_i is the outer radius of the inner cylinder and R_0 is the inner radius of the outer cylinder. This model does indeed predict that particles migrate from high shear regions to low, leading to a velocity profile which is in good agreement with experiments in a Couette geometry. On the other hand, since in a tube or a channel flow the term containing the shear rate in equation (4.3) vanishes along the centerline, the two terms in equation (4.3) will balance only if $\phi = \phi_m$ at that point. In turn, this leads to an infinite concentration gradient at the centerline which of course implies that the continuum description used in the analysis fails over distances $O(a)$ from the centerline, where again a refers to the particle radius. Hence, even though they accurately model the observed particle velocity profile which is blunted along the centerline in a tube or channel flow, the constitutive equations proposed by Leighton & Acrivos and by Phillips *et al.* need to be modified so as to yield realistic particle concentration profiles near zero shear locations.

2.2. Suspension balance model

As mentioned in §1, Nott & Brady (1994) proposed a suspension balance model to explain the migration of particles flowing under action of shear.

In this model mass, momentum and energy balances for particulate(and the entire suspension) are solved simultaneously for the concentration, the bulk velocity and the suspension temperature. The balance equations for the suspension are obtained by averaging the conservation of mass, energy and Cauchy's equation of motion. For a given geometry, these equations need to be solved in conjunction with appropriate boundary conditions. In these equations, a viscous stress term, the *particle (or suspension) pressure*, is given by

$$\Pi = \frac{1}{2}(p(\phi)\sqrt{T} + \bar{p}(\phi)\gamma), \tag{4.8}$$

where $p(\phi)\&\bar{p}(\phi)$ are nondimensional and monotonically increasing functions of the volume fraction ϕ, which can be measured from independent experiments or simulations. Nott & Brady argued that particle migrations and concentration variations occur in order to keep the suspension pressure constant in directions perpendicular to the mean motion.

The model by Nott & Brady reduces to the diffusive flux model discussed earlier for a unidirectional and fully developed shear flows such as in a Couette device. These authors have shown that, if only the second term on the right-hand side of equation (4.8) is retained, the particle conservation equation simplifies in this case to

$$\frac{\partial \phi}{\partial t} = \frac{2a^2}{9r}\frac{\partial}{\partial r}\{r[f(\phi)\bar{p}'(\phi)\gamma\frac{\partial \phi}{\partial r} + f(\phi)\bar{p}(\phi)\frac{\partial \gamma}{\partial r}]\} \tag{4.9}$$

where $f(\phi)$ is the known hindered settling function. The above equation is of the same form as that proposed by Phillips, *et al.* , equation (4.3). However, it is important to note that equation (4.3) contains only one proportionality function $\bar{p}(\phi)$ whereas the models proposed by Leighton & Acrivos and by Phillips, *et al.* contain two independent functions of ϕ in the former or two independent model parameters $K_c \& K_\eta$ in the latter. In addition, the Nott & Brady model takes into account the diffusive flux of the fluctuation energy - thus, the temperature can be finite even when the local shear rate vanishes. For a Couette flow, the fluctuation energy balance simplifies to

$$\eta(\phi) - \alpha(\phi)T + \frac{\epsilon^2}{r}\frac{d}{dr}\left\{r\kappa(\phi)\frac{dT}{dr}\right\} = 0, \tag{4.10}$$

where $\epsilon = a/(R_o - R_i)$, T & r are rendered dimensionless with $\gamma^2 a^2$ & $(R_o - R_i)$ respectively, and $\alpha(\phi) \& \kappa(\phi)$ are the dimensionless phenomenological coefficients which need to be determined by independent measurements. Hence the *temperature* at any point in the suspension depends on the local shear rate, the particle concentration and on the particle aspect ratio ϵ. Unlike the model by Leighton & Acrivos or by Phillips *et al.* , the model by Nott & Brady has not been tested as yet against experimental measurements of the particle velocity fluctuations, the *temperature* and the particle concentrations.

The model by Nott & Brady can also be used to derive a diffusion equation for *tracer* particles in a uniform shear flow under conditions where the particle

concentration is also uniform. In fact, these authors argued that the driving force for *tracer* motion relative to the mean is the gradient in the *partial pressure* of the tracer particles and thereby obtained for the particle tracer diffusivity:

$$D = \frac{2}{9}\gamma a^2 f(\phi)\bar{p}(\phi) = \frac{2}{9}af(\phi)p(\phi)\sqrt{T}, \tag{4.11}$$

where T is only a function of ϕ in this case. Clearly experiments are needed to measure D, T, f, p and $\bar{p}$ in order to test the predictions of this suspension balance model.

3. Experimental apparatus and instrumentation

3.1. Couette device

We measured particle velocity fluctuations in a narrow gap cylindrical Couette device which establishes a one dimensional suspension flow. Other geometries(eg. a rectangular channel or a closed loop pipe flow) are subject to *pump fluctuations*, *bubble generation* etc. which complicate the analysis of the experimental data. To get accurate and reliable fluctuation measurements, a specially constructed Couette device, shown schematically in figure 4.1, was designed. The two cylinders were made of high quality plexiglass which had a refractive index of 1.490@24°C. The outer radius of the inner cylinder (R_i) was 7.5425 cm and the inner radius of the outer cylinder(R_0)

was 8.2245cm, giving a gap size equal to 0.682cm with an accuracy of 25μm. The inner cylinder was mounted on a shaft which in turn was mounted on a computer controlled feedback motor (ID Corp., California). This motor provided rotational speeds to an accuracy of 0.02%. Also, the shaft was aligned accurately with two bearings separated by o-rings. We sealed the bottom of the gap with mercury. This eliminated three-dimensional secondary flows by creating a stress-free boundary, and also suppressed any thermal non- uniformities in the suspension above it. A great advantage of this design is that it enabled us to perform LDA measurements in the forward scatter mode.

We then mounted, on the outer cylinder, a plane window(shown as (a) in figure 4.1) filled with a refractive index matched fluid in order to remove any errors arising from the refraction of the laser beam at the cylindrical surface(Boadway & Karahan, 1981). Using this plane window, the particle fluctuating velocities were measured in the θ and z directions. But since the LDA technique measures the particle velocity component in the direction of its fringe pattern movement, it is impossible to generate the required fringe pattern in the radial direction using LDA beams passing through the above window. Hence we attached one more window(shown as (b) in figure 4.1), filled with an index matched fluid. The radial mean velocity and velocity fluctuations were then obtained by passing LDA beams through position A shown in figure 4.1. Therefore, this specially constructed Couette device appears to be better suited for making laser Doppler measurements than other

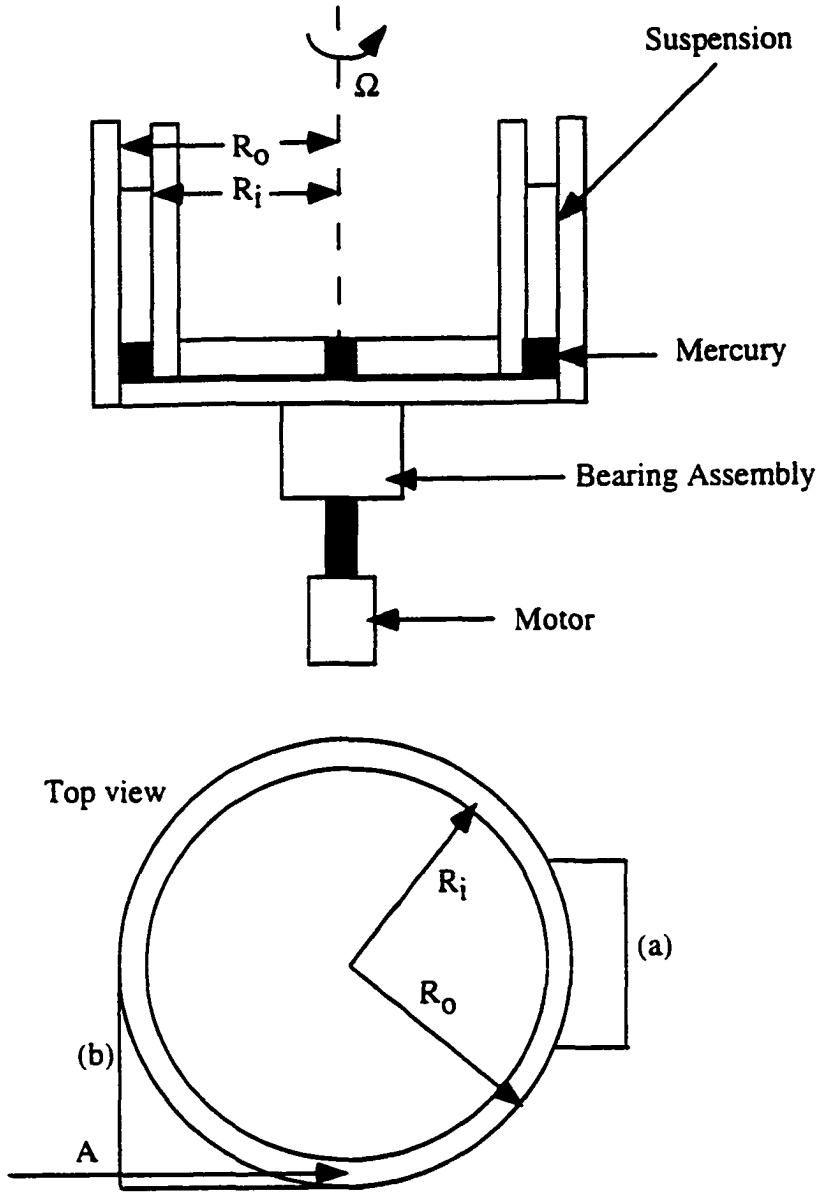

Figure 4.1: Schematic of the Couette device and the experimental setup.

available designs which can only measure two components of the velocity in the back-scatter mode.

3.2. Suspensions

In this work we used fairly monodisperse PMMA particles (standard deviation $\sim$ 25 microns) with mean diameter $325\mu m$, and density(ρ_p) 1.172 gm/cc. The particles, which were obtained from Zenica Resins as a single lot (grade Neocryl 738), were sieved several times with an alcohol-water mixture to obtain the desired range of particle sizes. We found that these particles were free of air bubbles and were spherical when placed under a microscope. In these size ranges, approximately $25-35$ particles can pack closely across the gap of the Couette device. Following the recipe of Krishnan *et al.* (1996), a suspension of these particles was made using a mixture of 77.38% Triton X-100, 9.23% water and 13.39% anhydrous zinc chloride (weight percentages) which matched the refractive index and density of the acrylic spheres. The pure suspending fluid had a viscosity of 3.4 Pa.s at the operating temperature of 23° C. The suspension was sheared for several hours to achieve a uniform concentration and to drive out any air bubbles. The experiments were carried out at applied shear rates in range of 3 - 16/s for particle volume fractions of 20%, 30% and 40%.

3.3. Instrumentation

For the particle velocity fluctuation measurements, we used a Dantec laser-Doppler optical system which, together with its major parts and alignment with respect to the Couette device, is shown in the photograph(figure 4.2). The system has a 300mW argon-ion air cooled laser and single Bragg cell transmission fiber optics. The Bragg cell produces a shift frequency of 40 MHz. The fiber-flow system contains a 85 mm 2D- probe with 55X beam expander. We arranged the optical alignment to yield a measuring volume, based on the e^2 light intensity cut-off point, of $13\mu m$ in diameter and $49\mu m$ in length when a 514.5 nm(green) beam of 2.2mm unfocused diameter was used. Light scattered in the forward direction was collected by a 55X receiving optics connected to a photomultiplier (PM) tube. A 514.5 nm filter was attached between the pinhole and the photomultiplier. The output of the PM tube was connected to an online processor called Enhanced Burst Spectrum Analyzer(model 57N20) developed by Dantec. This BSA employs an advanced burst detection scheme(Casperson, 1992; Lading, 1987) to accurately find and validate the burst. The band pass filter is designed for measuring frequencies as low as 122 Hz. and is capable of processing signals with a signal to noise ratio as low as -6dB. A personal computer (Micron pentium 133 MHz) was connected to the BSA via IEEE488 to obtain the data. Also, a digital oscilloscope(Tektronix, 2232, 100MHz) with a digital sampling rate of 100 megasamples/sec was connected to the BSA to monitor

Figure 4.2: A picture showing the LDA system aligned with respect to the Couette device.

the signals. The correlation analysis was performed through a computer code developed by us. Details of this code are presented in §5.

The transmitting probe was always placed normal to each of the three windows. Also, a three-dimensional traversing system was used with positioning repeatability of $\pm 10\mu m$. Because of the bending of the laser beam when it passed from the air to the fluid medium, the distance traveled by the probe on a traverse in the radial direction, used to scan the points on the inner and the outer cylinders, was not the same as the gap size. Hence we performed a calibration of the traverse for each window.

4. Results

4.1. Mean flow

For a steady laminar flow of a fluid with uniform composition, the only non-vanishing component of the mean velocity field is the azimuthal one given by

$$u_\theta(r) = [\frac{\Omega R_i^2}{R_o^2 - R_i^2}](\frac{R_o^2}{r} - r) \tag{4.12}$$

Figure 4.3 presents the measured mean velocity, $\langle u_\theta \rangle$, as a function of the radial location, r^*, in the Couette gap. The mean velocities were normalized with respect to the speed of the inner cylinder and r^* was obtained by the transformation:

$$r^* = \frac{1}{R_o - R_i}(r - R_i). \tag{4.13}$$

The mean was calculated over 50000 samples measured over a period of time at an average shear rate of $16s^{-1}$ for a particle concentration of 40%. [1] This data was obtained at the rate of 3-4 kHz with a record interval of $80\mu s$. We noted that some test runs with 100000 samples produced identical mean velocities. As shown in figure 4.3, the measured profile is in agreement with that computed theoretically from equation (4.12). The good agreement of the measured data with the theoretical profile was taken as confirming the accurate alignment of the experimental apparatus. Also, the measured mean

[1] Even though the velocity profile in figure 4.3 appears to be linear, a simple calculation using exact analytical expression for the given geometry reveals that the shear rate varies by about 20% across the gap. However, the effect of the apparent wall slip velocity for $\phi \leq 0.4$ is negligible (c.f. Jana *et al.* .1995).

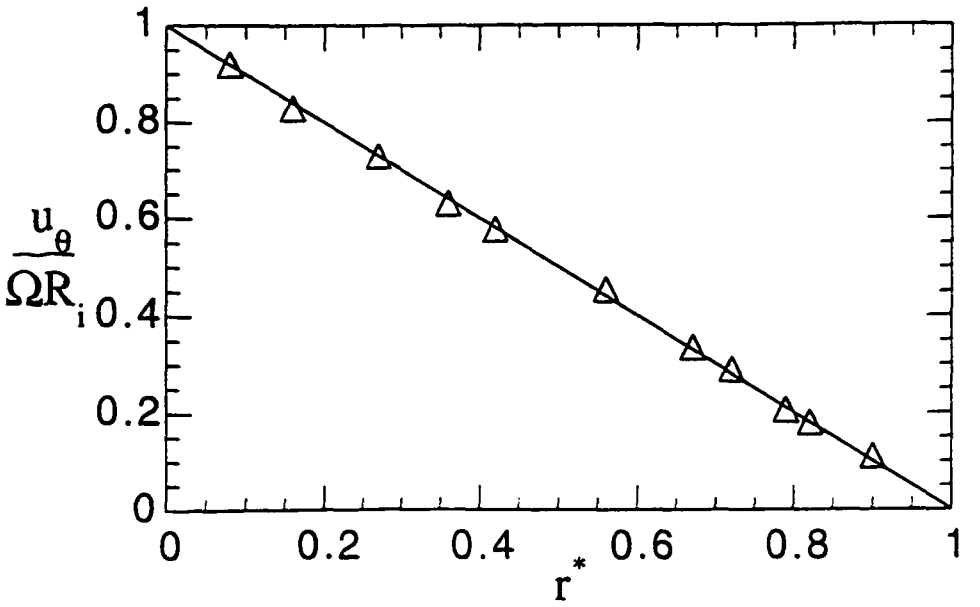

Figure 4.3: The mean velocity profile in the gap for $\gamma = 16s^{-1}$ and $\phi = 0.40$: – .using equation (4.12); △–experiments.

velocities in the r and z directions, $\langle u_r \rangle$ & $\langle u_z \rangle$, were found to be negligible at various radial locations.

4.2. LDA Noise

To obtain accurate particle velocity fluctuations, it is important to subtract the velocity fluctuations caused by the finite measuring volume(Durst *et al.* ,1995), the fringe pattern distortion (Ruck, 1991) and by the electronic & laser noise from the signal processing equipment, the air cooled laser and/or the frequency shift drivers used with LDA equipment. Since it is impossible to calculate separately the contribution to the velocity fluctuations

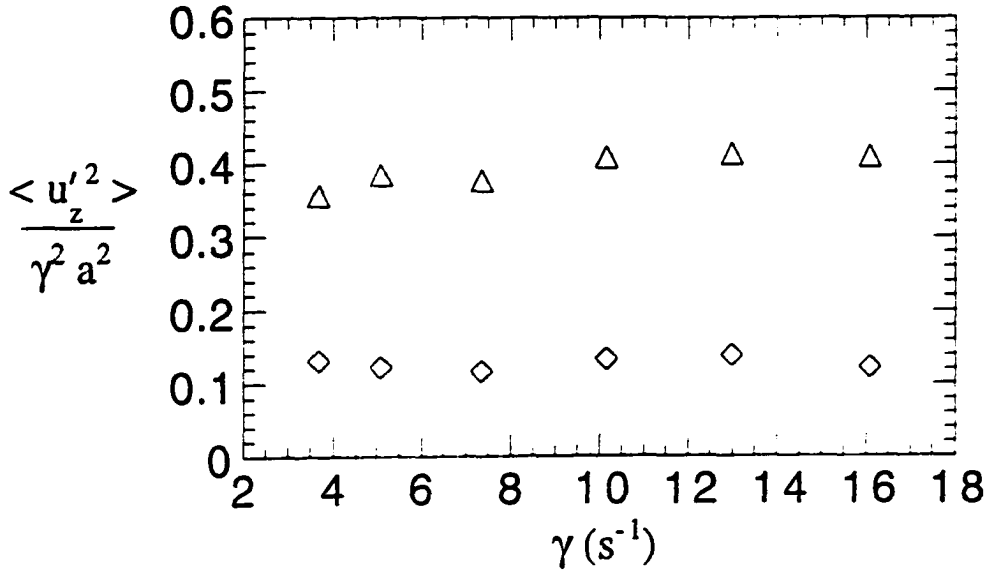

Figure 4.4: Plot of $\langle u_z'^2 \rangle$. the experimentally determined mean square fluctuating velocity in the vorticity direction vs. γ: $\diamond$ for $\phi = 0.02$. $\triangle$ for $\phi = 0.40$.

from these sources, we estimated the sum of all the contributions referred to above by measuring the velocity fluctuations in a dilute (2% particle concentration) suspension undergoing shear. Under these conditions, a non-zero fluctuating velocity was detected even when particle fluctuations due to hydrodynamic interactions were negligible. This non-zero fluctuating velocity was taken to represent the error from the LDA noise and was subtracted out from the particle velocity fluctuation velocity measurements. Unfortunately, as shown in figure 4.4, we found that the order of magnitude of the LDA noise was the same as that of the particle velocity fluctuations. Hence, our measurements of T are subject to a considerable degree of uncertainty.

We measured the fluctuating velocity for particles of size $325\mu m$ which

was greater than the size of the measuring volume. As detailed in §3.2, the refractive index of the particles and that of the suspending fluid were matched closely and the particles were chosen to be high quality spheres with no air bubbles inside them. Hence, it appears safe to assume that the Doppler signal was received from the scattered light due to slight imperfections on the surface of the particles. These surface scattering points have translational as well as rotational velocity components. But since only the translational velocity components contribute to the *suspension temperature*, given by equation (4.1), it is essential that the contribution of the particle rotation to the particle velocity measurements be eliminated. But since the angular velocity of the particles in a concentrated suspension is not known, it is impossible to estimate or eliminate this rotational contribution to $\langle u'^2 \rangle$. Hence, the measured suspension temperature is given as

$$T^{meas} = T^{tr}(eq.(4.1)) + T^{rot}, \tag{4.14}$$

where the superscript *tr* & *rot* denotes the translational and the rotational components respectively. In arriving at equation (4.14) we have used the fact that since the location of the scattering centers on the surface of a given particle is random, the translational and rotational components of the measured velocity fluctuations are uncorrelated. The following section presents the measured particle velocity fluctuations which includes the rotational contribution.

4.3. Velocity fluctuations measurements

The particle fluctuation experiments were conducted at solids concentrations ranging from 20 to 40% and for values of γ ranging from 3 to 16/s. All the measurements were performed at $r^* = \frac{1}{2}$ i.e. the middle of the Couette gap. In figures 4.5-4.7 we present plots of mean square velocity fluctuations in three directions for the case of $\phi = 0.2, 0.3\&0.4$, where the dimensionless mean square fluctuation velocity is shown as function of γ. Here, the mean square fluctuating velocity is scaled with $\gamma^2 a^2$. The error bars drawn for our data represent the uncertainty in five independent sets of measurements. Clearly, the fluctuating velocity component in the flow direction is negligible compared to its magnitude in the velocity gradient and vorticity directions. This shows that velocity fluctuations are anisotropic and that they depend upon the flow configuration. The fluctuating velocity increases with increasing concentration, as was reported in the study by Nott & Brady (1994). The same trend was also observed in the experiments by Shapley *et al.* (1997). Our results for the suspension temperature are plotted in figure 4.8 together with the preliminary results of the experimental study by Shapley *et al.* (1997). Although Shapley *et al.* used the same technique to measure the particle velocity fluctuations, their estimated values for suspension temperature are somewhat larger than those found in this study. At present, we cannot pinpoint the cause of this discrepancy and more experiments are clearly needed.

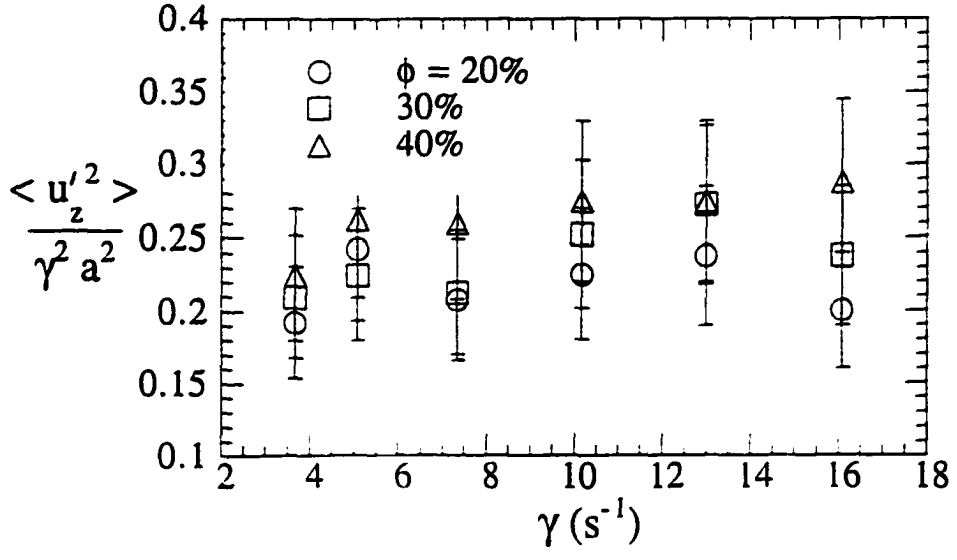

Figure 4.5: Plot of $\langle u_z'^2 \rangle$, the experimentally determined mean square fluctuating velocity in the vorticity direction vs. γ for $\phi = 0.2$, 0.3 and 0.4.

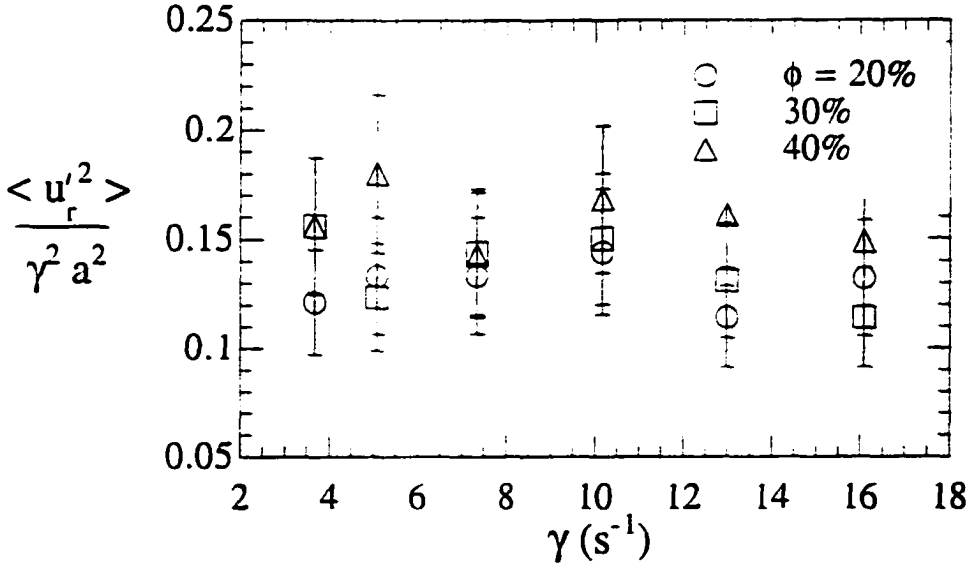

Figure 4.6: Plot of $\langle u_r'^2 \rangle$, the experimentally determined mean square fluctuating velocity in the velocity gradient direction vs. γ for $\phi = 0.2$, 0.3 and 0.4.

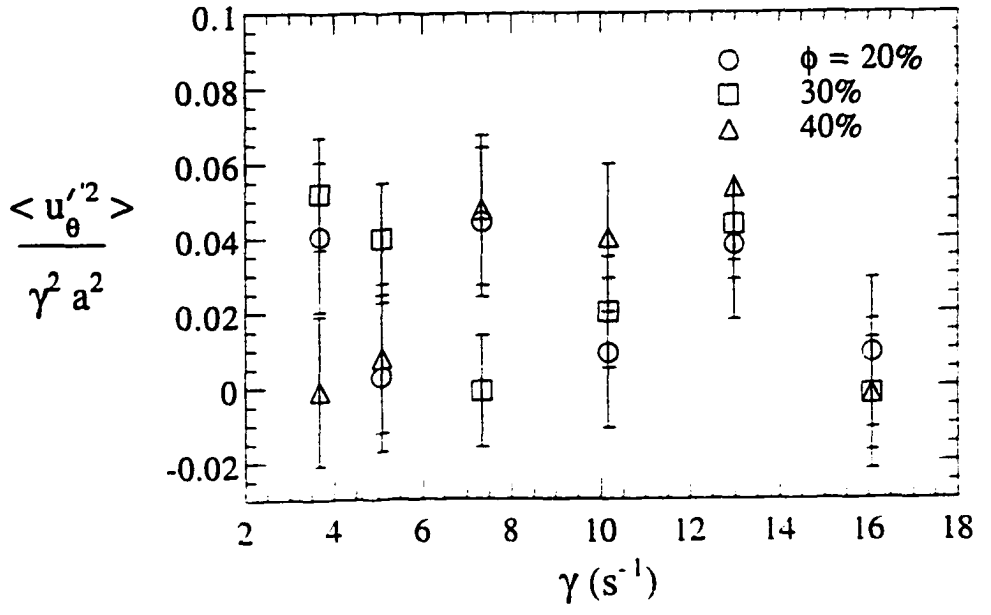

Figure 4.7: Plot of $\langle u_\theta'^2 \rangle$, the experimentally determined mean square fluctuating velocity in the flow direction vs. γ for $\phi = 0.2$, 0.3 and 0.4.

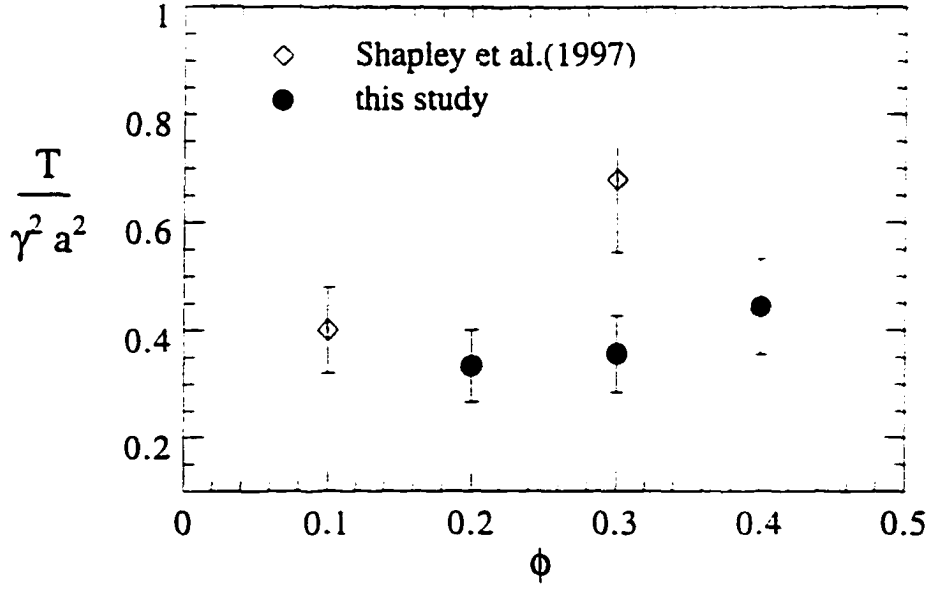

Figure 4.8: Plot of the dimensionless suspension temperature T vs. ϕ for $\gamma = 0.8s^{-1}$ and comparison of the present results with the experiments of Shapley *et al.* (1997).◇–from Shapley *et al.* (1997), ●–from this study.

4.4. A possible remedy

The experimental work described above has established that it is not possible to completely eliminate the influence of the particle rotation and of the LDA noise from the measured velocity fluctuations data using our current understanding of the LDA technique. Here, we propose a possible method that can be used to remedy this situation.

We note that the Doppler frequency (and thus the velocity) determined by an LDA signal processor is the weighted average of frequencies of all scattering points that contribute to the signal. Now the instantaneous velocity vector of the i^{th} scattering point on a j^{th} particle inside the measuring volume at time t_k is given by

$$\mathbf{u}_{ij}(t_k) = \mathbf{u}_{ij}^{tr}(t_k) + a\{\omega_j(t_k) \times \mathbf{n}_{ij}(t_k)\} \tag{4.15}$$

where ω_j is the instantaneous angular velocity vector of the j^{th} particle, $\mathbf{n}_{ij}$ is the vector normal to the surface of the j^{th} particle at the i^{th} scattering point and the superscript tr denotes the translational velocity. Thus, the measured velocity vector at any instant t_k, when there are $N_j(t_k)$ scattering points on particle j and M particles inside the measuring volume, is given by

$$\mathbf{u}(t_k) = \frac{\sum_{j=1}^{M} \sum_{i=1}^{N_j(t_k)} \mathbf{u}_{ij}(t_k) W_{ij}(\mathbf{x})}{\sum_{j=1}^{M} \sum_{i=1}^{N_j} W_{ij}(\mathbf{x})} \tag{4.16}$$

where $W_{ij}(\mathbf{x})$ is the weight function of the i^{th} scattering point with position vector $\mathbf{x}$. Since the signal amplitude for a given scattering point at a given

time is proportional to the intensity of the beam incident on it, a suitable weight function is given by the illuminating intensity as a function of position in the scattering volume(see- Durst et al., 1981; Kreid, 1974). Note that the direction of the normal vector is random and uncorrelated with either $\mathbf{u}(t_k)$ or $\omega(t_k)$. Thus, when a large number of samples (N^{sample}) are taken over a period of time, the rotational velocity vector will contribute only to the mean square velocity fluctuations.

Next, we recall that the auto-correlation function is defined as

$$\mathbf{R}(\tau) = \frac{1}{N^{sample}} \sum_{k=1}^{N^{sample}} \{[\mathbf{u}(t_k) - \langle \mathbf{u} \rangle] \cdot [\mathbf{u}(t_k + \tau) - \langle \mathbf{u} \rangle]\}, \tag{4.17}$$

where $\langle \mathbf{u} \rangle$ is the mean of the measured velocity, given by equation (4.16), over a large number of samples. In addition, as mentioned earlier, the direction of the normal vector, $\mathbf{n}_{ij}$ in equation (4.15), is random and it is completely uncorrelated with either $\mathbf{u}^{tr}(t_k)$ or $\omega(t_k)$ for any $\tau \neq 0$. Hence, for $\tau \rightarrow 0^+$, only the translational velocity of the particles contributes to the auto-correlation function $\mathbf{R}(\tau)$. Therefore, the expression for the *suspension temperature* given by equation (4.1) is modified to

$$T = \lim_{\tau \to 0^+} \mathbf{R}_{u_\theta}(\tau) + \lim_{\tau \to 0^+} \mathbf{R}_{u_r}(\tau) + \lim_{\tau \to 0^+} \mathbf{R}_{u_z}(\tau) \tag{4.18}$$

where the contribution of the random noise and of the particle rotation is eliminated. In addition, the long time diffusivity given by equation (4.2) can be calculated by integrating the auto-correlation function measured in the experiments.

We tested the proposed scheme by measuring the local particle velocities sampled over a large interval of time and then by computing particle velocity fluctuation auto-correlation function. To ensure a high statistical reliability of the fluctuation measurements, the time interval between the samples, $\Delta t = t_{k+1} - t_k$, was chosen close to the integral time scale of the flow:

$$\Delta t \approx \frac{R_o - R_i}{\langle u_\theta \rangle}. \tag{4.19}$$

Using this sampling time interval, the azimuthal instantaneous velocity, $u_\theta(t_k)$, was first measured at a shear rate of 16/s for a particle concentration of 40%. The instantaneous flow velocity was then measured at random arrival times, t_k and the sampling size was set to $N = 10^5$ to ensure a correct statistical ensemble of the data. Since the particle velocity data were not obtained at regular time intervals, the auto-correlation function, given by equation (4.17), was computed from the modified equation given by

$$\mathbf{R}(\tau) = \frac{1}{N^{sample}} \sum_{k=1}^{N^{sample}} \{[\mathbf{u}(t_k) - \langle \mathbf{u} \rangle] \cdot [\mathbf{u}(t_k + \bar{\tau}) - \langle \mathbf{u} \rangle]\}, \tag{4.20}$$

where $\tau - \Delta\tau \leq \bar{\tau} < \tau + \Delta\tau$ with $\Delta\tau$ chosen to be equal to $0.1/\dot{\gamma}$. The modification given above was chosen so as to avoid interpolating the measured data and to have an ensemble average of at least 2000 samples for each τ. The computations were performed using a FORTRAN program. Shown in figure 4.9 is the plot of the auto-correlation function, $R_{u_\theta}(\tau)$, as a function of the time lag, τ, at $\tau^* = 0.5$, from which it is seen that the measured velocity

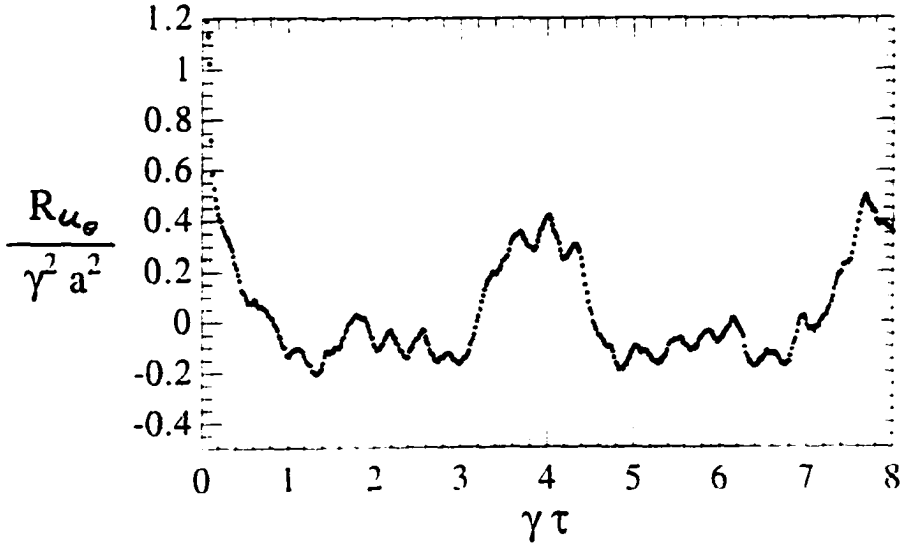

Figure 4.9: Plot of the dimensionless auto-correlation function vs. time lag τ at $r^* = 0.5$ and $\sigma = 0.40$.

fluctuation has a dominant periodic component. Hence, it was not possible to extract the auto-correlation part from the measured data accurately. Our experiments seemed to indicate that small variations in the radii of the inner and of the outer cylinders was the source of the periodic motion. The existence of non-uniformities in the radius of the inner cylinder was confirmed by measuring the velocity at the surface of the inner cylinder as well as the time period of its periodic component at various speeds of the inner cylinder. Due to time constraints, we decided against fabricating an accurate Couette device free of such non-uniformities. This task is being left for the future.

5. References

Abbott, J. R., Tetlow, N., Graham, A. L., Altobelli, S. A., Fukushima, E., Mondy, L. A. & Stephens, T. S. 1991 Experimental observations of particle migration in concentrated suspensions: Couette flow. *J. Rheol.* **35**, 773-779.

Ahn, H., Brennen, C. E. & Sabersky, R. H. 1991 Measurements of velocity, velocity fluctuations, density and stresses in chute flows of granular materials. *Trans. ASME E: J. Appl. Mech.* **58**, 792-803.

Boadway, J. D. & Karahan, E 1981 Correction of laser Doppler anemometer reading for refraction at cylindrical interfaces. *DISA Information*, **26**, 4-6.

Casperson, C. 1992 The enhanced burst spectrum analyzer. *Dantec Information* **11**, 17-20.

Chow, A. W., Sinton, S. W., Iwamiya, J. H. & Stephens, T. S. 1994 Shear-induced migration in Couette and parallel-plate viscometers: NMR imaging and stress measurements. *Phys. Fluids A* **6**, 2561-2576.

Drake, T. G. 1991 Granular flow: physical experiments and their implications for microstructural theories. *J. Fluid Mech.* **225**, 121-152.

Durst, F., Jovanovic, J. & Sender, J. 1995 LDA measurements in a near-wall region of a turbulent pipe flow. *J. Fluid Mech.* **295**, 305-335.

Durst, F., Melling, A. & Whitelaw, J. H. 1981 *Principles and practice of Laser-Doppler anemometry.* Academic Press, London.

Hsiau, S. S.& Hunt, M. L. 1993 Shear-induced particle diffusion and longitudinal velocity fluctuations in a granular-flow mixing layer. *J. Fluid Mech.*

251, 299-313.

Jana, S. C., Kapoor, B. & Acrivos, A. 1995 Apparent wall slip velocity coefficients in concentrated suspensions of noncolloidal particles. *J. Rheol.* **39(6)**, 1123-1132.

Jenkins, J. T. & McTigue, D. F. 1990 Transport processes in concentrated suspensions: the role of particle fluctuations. In *Two phase flows and waves*, (ed. D. D. Joseph & D. G. Schaeffer). Springer.

Kapoor, B. & Acrivos, A. 1995 Sedimentation and sediment flow in settling tanks with inclined walls. *J. Fluid Mech.* **290**, 39-66.

Koh, C. J., Hookham, P. & Leal, L. G. 1994 An experimental investigation of concentrated suspension flows in a rectangular channel. *J. Fluid Mech.* **266**, 1-32.

Kreid, D. K. 1974 Laser-Doppler velocimeter measurements in nonuniform flow: error estimates. *Applied Optics*, **13**(8), 1872-1881.

Lading, L. 1987 Spectrum analysis of LDA signals. *Dantec Information* **05**, 2-8.

Leighton, D. & Acrivos, A. 1987 Measurement of shear-induced self diffusion in concentrated suspensions of spheres. *J. Fluid Mech.* **177**, 109-131.

Natarajan, V. V., R., Hunt, M. L. & Taylor, E. D. 1995 Local measurements of velocity fluctuations and diffusion coefficients for a granular material flow. *J. Fluid Mech.* **304**, 1-25.

Nicolai, H., Herzhaft, B., Hinch, E. J., Oger, L. & Guazzelli, E. 1995 Particle

velocity fluctuations and hydrodynamic self diffusion of sedimenting non-Brownian spheres. *Phys. Fluids* **7**, 12-22.

Nicolai, H., Peysson, Y. & Guazzelli, E. 1996 Velocity fluctuations of a sphere falling through a sedimenting suspension. *Phys. Fluids* **8**, 1-8.

Nott, P. R. & Brady, J. F. 1994 Pressure-driven flow of suspensions: simulation and theory. *J. Fluid Mech.* **275**, 157-199.

Phillips, R. J., Armstrong, R. C., Brown, R. A, Graham, A. L. & Abbott, J. R. 1992 A constitutive equation for concentrated suspensions that accounts for shear-induced particle migration. *Phys. Fluids A* **4**, 30-40.

Ruck, B. 1991 LDA fringe pattern distortion by tracer particles inside the illuminating laser beams. *Laser Anemometry ASME* **2**, 629-636.

Shapley, N., Armstrong, R. C. & Brown, R. A. 1997 LDV measurements of particle velocity fluctuations in a concentrated suspension. *Society of Rheology Annual Meeting, Columbus, OH.*

Sinton, S. W. & Chow, A. W. 1991 NMR flow imaging of fluids and solid suspensions in Poiseuille flow. *J. Rheol.* **35**, 735-772.

IMAGE EVALUATION TEST TARGET (QA-3)

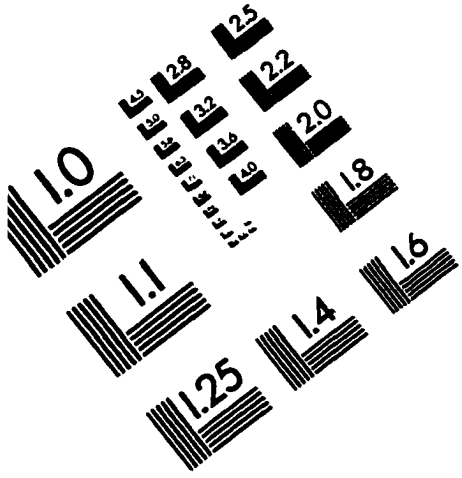

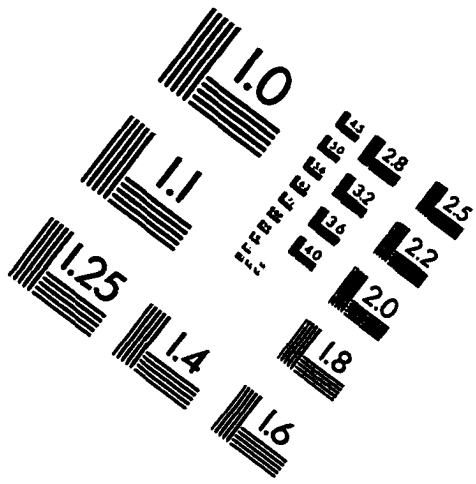

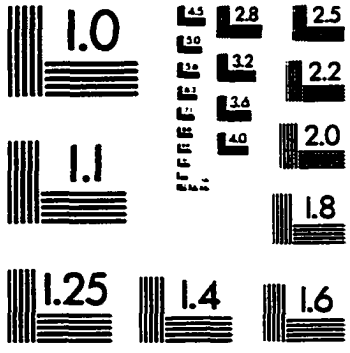

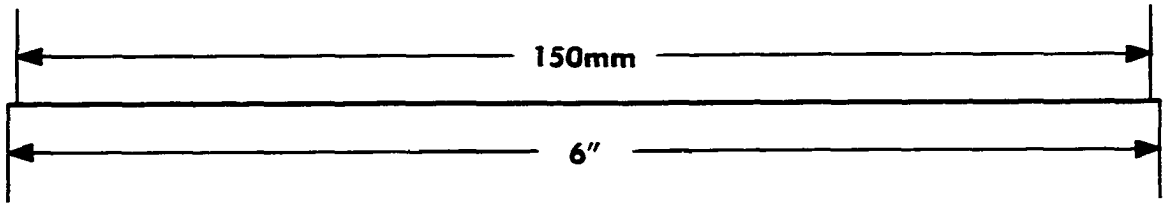

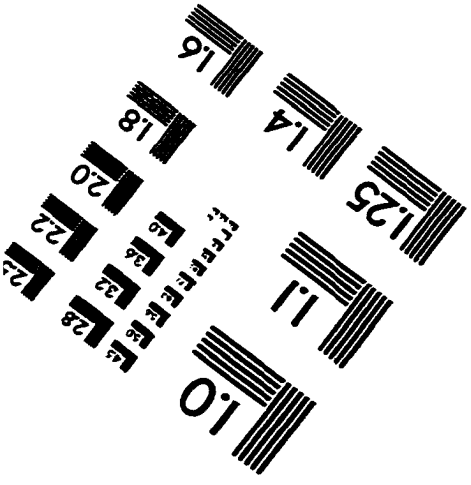

APPLIED IMAGE, Inc
1653 East Main Street
Rochester, NY 14609 USA
Phone: 716/482-0300
Fax: 716/288-5989